Microphone based on Polyvinylidene Fluoride (PVDF) micro-pillars and patterned electrodes

DISSERTATION

Presented in Partial Fulfillment of the Requirements for the Degree Doctor of Philosophy
in the Graduate School of The Ohio State University

By

Jian Xu, B.E., M.E.

Graduate Program in Mechanical Engineering

The Ohio State University

2010

Dissertation Committee:

Marcelo Dapino, Advisor

Derek Hansford

Ahmet Selamet

Gregory Washington

ABSTRACT

Piezoelectric materials have the ability to transfer energy between the electric and mechanical domains. Polyvinylidene fluoride (PVDF) exhibits higher piezoelectricity than other polymer materials such as nylon and polyvinyl chloride. PVDF is a superior material for sensors because its stress constant, the ability to convert stress into electrical energy, is more than 20 times higher than that of lead zirconate titanate. Nonetheless, there is significant interest in improving the effective stress constant of PVDF devices beyond the intrinsic sensitivity of the material. Significant research has focused on improvements in material properties, such as increasing β phase ratio or artificially introducing defects, and processing, such as optimizing stretch ratio and poling temperature or applying a high electric field. This research is focused on improving the stress constant, or sensor sensitivity, by means of design.

The acoustic sensor presented in this dissertation exploits the key advantages of PVDF as a sensor material by means of two key design elements aimed at increasing the charge and decreasing the effective device capacitance. The first design element is a stress amplification mechanism through the area ratio between the overall surface exposed to acoustic waves and the area of an array of PVDF micro-pillars. Because PVDF responds to stress, this mechanism increases the amount of charge for a given pressure level. The second design element is top and bottom electrodes selectively patterned to form an overlapping active area determined by the micro-pillars. Excluding the capacitance of the other inactive area, the design with patterned electrodes reduces the capacitance of the sensor and hence increases the voltage generated by the sensor.

The small size, high stiffness, and reduced mass of MEMS sensors are of great interest because such devices can significantly improve both the temporal and spatial measurement bandwidth. The sensor realization requires micro-fabrication process and this technology is available at the Biomedical Engineering Center of The Ohio State University. Previously patterned polydimethylsiloxane (PDMS) stamps molded from photolithographically fabricated masters are used in the production of individual and interconnected PVDF micro-pillar arrays. Taking advantage of the thickness or "33" mode, the developed PVDF micro-pillar sensor has a frequency bandwidth of at least 20 Hz-100 kHz and maximum response of up to a few MHz (depending on specific sensor dimensions).

A PVDF micro-pillar sensor with patterned electrodes and gap ratio of 5.82 was developed and various acoustic tests were performed on this sensor. The sensitivity calibration test shows that the developed sensor has a sensitivity of 189.3 μV/Pa, which is 60.39× greater than that of commercial solid PVDF with the same footprint and thickness. The measured stress constant of the sensor is -19.93 V/m/Pa, which is 60.39× larger than that of commercial solid PVDF (g_{33} =-0.33 V/m/Pa). The measured stress constant amplification ratio is in good agreement with the predicted amplification ratio of 59.19, thus confirming the performance advantages of the micro-pillar sensor.

To my wife and parents.

Without the continous love, support, and encouragement from my families this work would never be completed.

ACKNOWLEDGMENTS

I would like to take this opportunity to express my sincere gratitude to my adviser, Prof. Marcelo Dapino, for his guidance, assistance, and support during my Ph.D. study. Dr. Dapino's expertise on smart materials and his passion on the challenging projects always kept me moving forward. I have fully enjoyed exchanging my thoughts with him during my stay at The Ohio State University. This research would never be possible without his suggestions, enthusiasm, and trust.

I would also like to thank my dissertation committee, Prof. Derek Hansford, Prof. Ahmet Selamet, and Prof. Gregory Washington for reviewing my proposal, addressing important issues, and providing valuable suggestions. The knowledge acquired from their courses was very useful in my research. I am also grateful to Daniel Gallego-Perez in Dr. Hansford's group for his collaboration, discussions, and hard work in this research. Without the inspiration and help from Dr. Hansford's group, this project would never have happened in the first place. We acknowledge Ryan Stromberg and Rick Nay of Hysitron Inc. for assistance with the indentation tests and OSU Nanotech West Lab technical staff for technical assistance.

I am grateful to the member organizations of the Smart Vehicle Concepts Center and the National Science Foundation Industry/University Cooperative Research Centers program for supporting this work. I am also thankful to Prof. Rajendra Singh for useful discussions. Thanks also to the Graduate School and Department of Mechanical Engineering for funding my first year of research through a University Fellowship.

I would like to thank Dr. Sandeep Vijayakar and Dr. Farong Zhu (Advanced Numerical Solutions, LLC, OH) for initiating this project.

Finally, I received substantial support from fellow students of the Smart Materials and Structures Lab and the Mechanical Department staff for their assistance, cooperation, and help.

VITA

January 29, 1975	Born - Wu Jin, Jiangsu China
1998	B.E. Mechanical Engineering, Tsinghua University
2003	M.E. Mechanical Engineering, Tsinghua University
2005-2006	Graduate Fellow, The Ohio State University
2006-present	Graduate Research Associate, The Ohio State University

PUBLICATIONS

J. Xu, M.J. Dapino, D. Gallego-Perez, and D. Hansford, "Microphone based on Polyvinylidene Fluoride (PVDF) micro-pillars and patterned electrodes," *Sensors and Actuators A: Physical*, Vol. 153, pp. 24-32, 2009.

J. Xu, M.J. Dapino, D. Gallego-Perez, and D. Hansford, "Acoustic sensor with PVDF micro-pillars and patterned electrodes," *in Proceedings of the ASME Conference on Smart Materials*, October 2008.

J. Xu, M.J. Dapino, D. Gallego-Perez, and D. Hansford, "Design and micro-fabrication of A PVDF acoustic sensor," *in Proceedings of SPIE*, Vol. 6929, April 2008.

FIELDS OF STUDY

Major Field: Mechanical Engineering

Studies in:

Smart Materials and Structures
Noise Vibration and Harshness Control
Numerical Optimization

TABLE OF CONTENTS

Page

Chapters:

LIST OF FIGURES

LIST OF TABLES

CHAPTER 1

INTRODUCTION AND BACKGROUND

1.1 Introduction and Motivation

Ferroelectric materials constitute a class of smart materials that produce coupling between the mechanical and electrical domains. Piezoelectrics are the most well know examples of ferroelectric class. The piezoelectric materials exhibit the direct piezoelectric effect, the generation of an electric potential when stress is applied, as well as the reverse piezoelectric effect, the generation of stress and/or strain when an electric field is applied. Polyvinylidene fluoride (PVDF) exhibits higher piezoelectricity than other polymer materials such as nylon and polyvinyl chloride. PVDF is a superior material for sensors because the stress constant, the ability to convert stress energy to electric energy, of PVDF is more than 20 times higher than lead zirconate titanate (PZT), which has a higher strain constant, the ability to convert electric energy to stress energy, and thus is a good material for various actuators. In addition to the high sensitivity of PVDF, a major advantage of PVDF over other smart materials, such as magnetostrictives, ferromagnetic, and shape memory alloys, is its high frequency bandwidth, which could be up to a few MHz. In general, magnetostrictive materials can be operated up to about 10 kHz. However, the applications based on magnetostrictives require the use of solenoids used to generate magnetic field. The feasible operating frequency of solenoid is typically less than 2-3 kHz. Further, if thermoelectric coupling is introduced into the systems, the operating frequency could be lowered to a few hertz.

Existing commercial microphones are capable of either high sensitivity or broad frequency bandwidth. Typical specifications for the former category include a sensitivity of about 50 mV/Pa and a frequency range of 10 kHz, whereas transducers in the latter category exhibit a sensitivity of about 1 mV/Pa and a frequency range of 70 kHz. It is emphasized that the above sensitivities include the gain provided by the built-in amplifier placed inside of the microphone case. These microphones tend to be large, with typical geometries having a diameter of 12 mm. While these devices work well in many applications, there is a need for acoustic sensors capable of exhibiting high sensitivity and broad frequency bandwidth, while simultaneously having a much smaller size than the existing designs.

Such microphones would enable new techniques for the measurement of noise-source characteristics, for example by means of extremely dense microphone arrays capable of measuring with great accuracy both pressure amplitude and direction. Such techniques will be crucial for guiding and validating the development of accurate noise prediction tools and effective suppression techniques [3, 32].

Ever since the microphone was invented in the late nineteenth century, it is widely used on audio applications that typically require a maximum sound pressure level (SPL) of 110-130 dB (re 20 μPa) and bandwidths of 10-20 kHz. However, aeroacoustic applications, which are facing ever-tightening regulatory constraints due to increasing community airport noise standards, require a maximum SPL in excess of 160 dB and bandwidths of on the order of 100 kHz.

One realization of microphones is electronic stethoscopes, which are commonly used for clinical auscultation and real-time monitoring of the human respiratory system. A significant volume of research has been devoted to the analysis of lung sounds based on empirical information of normal and abnormal lung sounds [9, 55]. Electronic stethoscope arrays for measurement of breathing sounds are of great interest due to their non-invasive nature, yet the utilization of these arrays for real-time monitoring of lung sounds is confined to large sound fields in adults. The existing electronic stethoscopes are too bulky, typically 25 mm in diameter, for utilization in infants and small children.

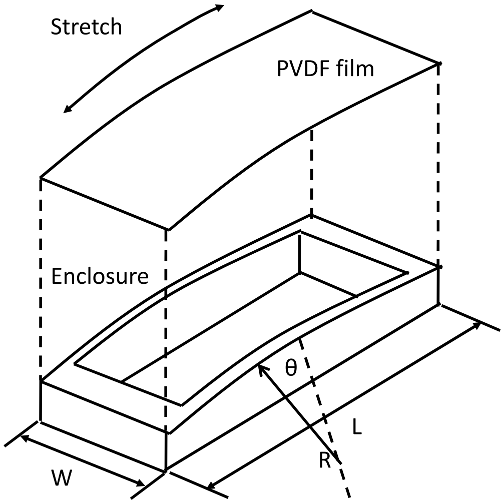

Figure 1.1: The principle of curved microphone structure [49].

Accordingly, several drawbacks of the existing microphones include:

- Limited in either bandwidth or sensitivity, which is not suitable for advanced diagnosis
- Limited dynamic range
- An array of multiple stethoscopes comprising bulky and cumbersome components

Two possible approaches, cylindrical curvature microphone based on commercial PVDF film and acoustic sensor with micro-pillars and patterned electrodes, are proposed and discussed in this dissertation. Developing a microphone based on commercially available PVDF is a good start point for this research because it can avoid some complicated issues of fabricating an active PVDF film such as polarization and electrodes metallization. However, the main focus of this research is to develop an ultrasonic acoustic sensor based on PVDF micro-pillars and patterned electrodes, which is the main contribution of the author. One potential application of the proposed micro-acoustic sensor would be vehicle positioning. Like animal echolocation, the vehicle would emit ultrasonic waves and an array of microsensors placed on the vehicle skin would measure in real time the echo of the emission (both magnitude and direction). The time difference between the emitted and reflected waves would provide localization of objects around the vehicle and would create safer driving conditions. Spatial location requires pointpoint accuracy, hence involving sensor dimensions much smaller than possible to fabricate with conventional designs.

Figure 1.1 shows the principle of curved microphone structure, which is also widely used in a commercial speaker [49]. In this design, the film is curved in one direction

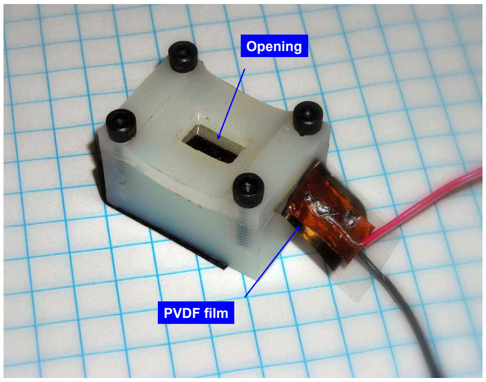

Figure 1.2: Cylindrical curvature microphone based on commercial PVDF film.

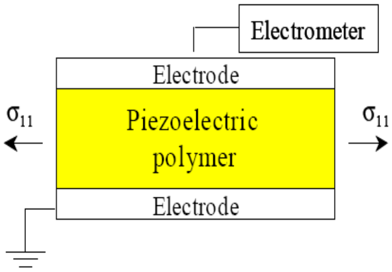

Figure 1.3: Mode 3-1.

and clamped rigidly onto each end of the enclosure, as shown in Figure 1.2. The acoustic pressure applied normal to the cylindrical surface of the PVDF film generates the internal large stress in the plane, which is converted into a charge on the electrodes. The charge produces an open circuit voltage since PVDF is a dielectric material [71]. The amplification effect is similar to the force amplification in a rope held at two ends (i.e., a rope can generate very larger tensile forces when subjected to a perpendicular center force). Typically, a commercial PVDF film is polarized in the x_3 direction. This kind of microphone works in 3-1 mode, as shown in Figure 1.3, because the induced stress is in the x_1 direction (i.e., the length direction).

The small size, high stiffness, and reduced mass of microelectromechanical systems (MEMS) sensors are of great interest because such devices can significantly improve both the temporal and spatial measurement bandwidth. MEMS technology

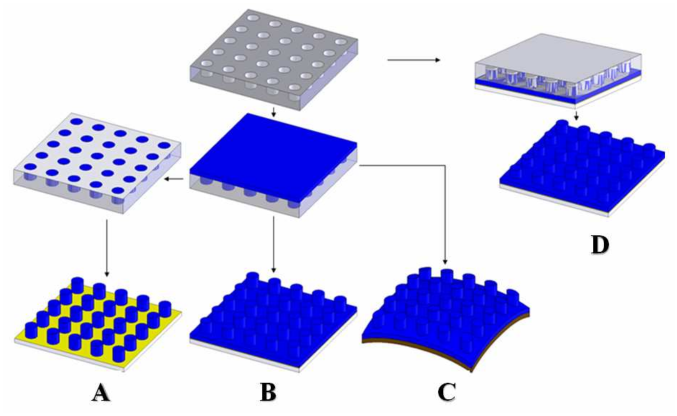

Figure 1.4: Schematic diagram of fabrication of PVDF microstructures: (A) Stamped discrete, (B) Stamped continuous on a rigid substrate, (C) Stamped continuous on a flexible substrate, (D) Embossed. (Figure courtesy D. Hansford)

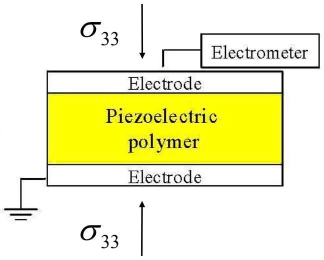

Figure 1.5: Mode 3-3.

has traditionally been focused on silicon based fabrication techniques. With the development of sacrificial layer micromolding (SLaM) and patterned substrate micromolding (PSM), the microfabrication of polymer microstructures is becoming increasingly promising [44, 19]. The sensor realization requires micro-fabrication process and this technology is available from Dr. Hansford's group at the Biomedical Engineering Center (BEC) of OSU. Previously patterned polydimethylsiloxane (PDMS) stamps molded from photolithographically fabricated masters are used in the production of individual and interconnected PVDF micropillar arrays as shown in Figure 1.4. Note that such sensor works under 3-3 mode, compared to 3-1 mode of the first approach. The improved sensitivity takes advantage of a large piezo stress constant g_{33} rather than g_{31}. The static sensitivity of PVDF film is defined as the ratio of the output voltage over the pressure acting on the PVDF material (i.e., $K = V_o/P$). For a given external pressure, the only feasible way to improve the sensitivity of PVDF film is to increase the voltage output of the film. The voltage produced by a capacitive sensor is given by the ratio between charge and capacitance (i.e., $V_o = Q/C$, where Q is the induced charge and C is the capacitance). So basically there are two ways to improve the voltage output of the PVDF film: one is to increase the charge generated by the PVDF film and the other is to reduce the capacitance of the device. Our developed micro-pillar sensor achieves the both ways and hence significantly improve the sensitivity of the sensor.

1.2 Overview of Smart Materials

Smart materials have the ability to convert one form of energy into another, and are widely used in sensing and actuation applications such as microphones, accelerometers, sonar transducers, structure morphing, energy harvesting, motion/force sensing, vibration control, etc. Smart materials have one or more properties that can change in response to external stimuli such as heat, electric or magnetic field, stress, light and pH. Smart materials can be commonly categorized into several classes based on the type of driving input and its corresponding response: piezoelectric, electrostrictive, electroactive, magnetostrictive, electrorheological and magnetorheological, shape memory, ferromagnetic shape memory, pH sensitive, temperature-responsive and chromogenic. In general, all of these smart materials are essentially transducers and thus the applications based on smart materials can be classified into two fundamental behaviors: sensing and actuation.

1.2.1 Magnetostrictives

Magnetostrictive materials produce energy transduction between the magnetic and mechanical domains. They not only deform in response to magnetic field, but also magnetize in response to stress. Giant magnetostrictive materials, especially rare earth-iron discovered by A.E. Clark, can generate magnetostrains which are two orders of magnitude larger than Nickel. Giant magnetostrictive materials like Terfenol-D and Galfenol exhibit strong spin-orbit coupling. Therefore, when an applied magnetic field rotates the spins, the orbital moments rotate so that considerable distortion of the crystal lattice occurs, which leads to large macroscopic strains [12]. In order to orient the magnetic moments perpendicular to its longitudinal axis, a bias compress load is usually applied to the magnetostrictive material. The magnetic moments tend to align along the direction of the external longitude magnetic field and this leads to orientation of the domains in longitude direction, which produce the strain generation. Butterfly curves are commonly obtained because two strain cycles are induced per magnetization and field cycle. Terfenol-D presents the best compromise between a large magnetostrain and a low magnetic field at room temperature. Terfenol-D achieves maximum strains of about 0.12% and has a frequency bandwidth up to 10 kHz including a ΔE effect [13, 29, 40]. The strong magnetoelastic coupling in magnetostrictive materials leads to large variation in elastic modulus is referred as the ΔE effect. Some of the drawbacks of Terfenol-D are that it is relatively expensive to produce and is very brittle. While Galfenol (Fe-Ga) is gaining in popularity because it is a new and robust magnetostrictive material that brings the possibility for a new class of transducers with 3-D multi-functionality and the capability to withstand harsh environments. Galfenol can produce 0.03% strain [41] and is machinable with common techniques [10]. The unique combination of mechanical robustness and high magnetostriction of Galfenol makes it ideal for applications as sensors and actuators that can take tension, bending, torsion, and shock loads in harsh environments.

1.2.2 Shape Memory Alloys

Shape memory alloys (SMAs) provide transduction between thermal and mechanical energy. A SMA is an alloy that remembers its original, cold, forged shape, and which returns to that shape after being deformed by applying heat. The most common SMA is NiTiNol, which has been investigated since 1962 [7]. In general, at high temperatures, SMA exhibits a body centered cubic austenite phase. At low temperatures, it exhibits martensite phase, which has a monoclinic crystal structure. When a SMA is cooled from its high temperature austenite phase, a twinned martensite structure is produced. This twinned structure comprises alternating rows of atoms tilted in opposite directions. The twins reoriented so that they all lie in the same direction after the material is subjected to a stress, which is known as detwinning. When the material is heated, the deformed martensite regains its cubic austenite form, and thus the original shape is recovered. So, this behavior is called as "shape memory effect" [64]. Two common effects are one-way and two-way shape memory (the material remembers two different shapes: one at low temperatures, and one at the high temperature shape). SMAs have numerous applications in many areas including areospace, medicine, orthodontics, safety devices, robotics, etc [17, 24, 47].

1.2.3 Ferromagnetic Shape Memory Alloys

Ferromagnetic shape memory alloys (FSMAs) were first identified by Ullakko at MIT in 1996 [74]. FSMAs in the Ni-Mn-Ga system are a recent class of smart materials that are of great interest because of their ability to produce large strains of up to 10% in the presence of magnetic fields. This strain magnitude is around 100 times larger than those of other smart materials such as piezoelectrics and magnetostrictives. One unique advantage of FSMAs over SMAs is that they exhibit faster response than the thermally activated SMAS because FSMAs are activated by magnetic field [18]. Therefore, the combination of large strains and fast response opens up opportunities for various possible applications such as sonar transducers, structural morphing, energy harvesting, motion/force sensing and active vibration control. Characterization and modeling of the FSMA Ni-Mn-Ga for sensing and actuation, which include continuum thermodynamics based energy model, non-linear and hysteretic constitutive relationships, dynamic sensing, tunable stiffness, frequency dependent strain-filed hysteresis, etc., have been fully explored by Sarawate at OSU [64].

1.2.4 Magneto and Electro-rheological Fluids

Magneto/electro-rheological fluids are oil or water based liquids that change their viscosity, yield stress, and other rheological properties when subjected to an external magnetic/electric field. In general, there are two types of particles (micrometer and nanometer size), which are suspended in the base fluid and align themselves along the lines of magnetic/electric flux when a magnetic/electric field is applied. For applications, it is crucial to ensure that the lines of flux are perpendicular to the direction of the motion to be restricted. These fluids have found applications [38, 57, 1, 56]in smart dampers, high frequency valves, force feedback devices, optics, and automotive clutches.

1.2.5 Ferroelectrics

Ferroelectric materials contain a class of smart materials that produce electromechanical coupling. Electrostrictive materials such as lead magnesium niobate (PMN), relaxor ferroelectric PMN-PT and relaxor KNaNbO-SrTiO ceramic exhibit a quadratic behavior (i.e., the induced stress/strain is a quadratic function of the applied electric field). These electrostrictive ceramics generally show lower hysteresis (less than 1%), have greater stiffness , lower strains (of about 0.1%) and good reproducibility [59]. They have found applications in electroacoustic transducers [52], active noise control [30], active vibration control [21], and electrostrictive deformable mirrors [31]. Piezoelectric materials are the most commonly known examples of ferroelectric class. The piezoelectric materials usually exhibit a linear behavior in which the induced stress or strain is a linear function of the applied electric field. PVDF based microphone is the focus of this dissertation and hence a more thorough examination of this piezoelectric material is provided in the following sections.

1.3 Polyvinylidene Fluoride

1.3.1 Properties and Crystal Structure of PVDF

Piezoelectricity is the ability of some materials to induce an electric field or electric potential in response to applied mechanical stress. The word is derived from the Greek “piezo” or “piezein”, which means to squeeze or press. Piezoelectricity was first discovered by the Curie brothers more than 100 years ago. They found that quartz deformed when subjected to an electrical field, and conversely, produced electrical charge when subjected to a mechanical stress. Before World War II, researchers discovered that certain ceramic materials could be made piezoelectric when highly polarized. PZT, composed of the chemical elements lead and zirconium and the chemical compound titanate, is a well-known ceramic material that shows a marked piezoelectric effect.

Table 1.1: Properties comparison between PVDF and PZT.

Property	Units	PVDF film	PZT
Density	$(10^3)\text{kg/m}^3$	1.78	7.5
Relative Permittivity	ϵ/ϵ_0	12	1,200
Strain Constant d_{31}	$(10^{-12})\text{C/N}$	23	110
Stress Constant g_{31}	$(10^{-3})\text{V/m/Pa}$	216	10
Constant k_{31}	% at 1 kHz	12	30
Acoustic Impedance	$(10^6)\text{kg/m}^2-\text{sec}$	2.7	30

The piezoelectric polymer Polyvinylidene Fluoride (PVDF), first discovered by Kawai [39], has been widely used for sensor development in a wide range of military, industrial and biomedical applications. Sensors based on PVDF piezo-electric polymers have many advantages, such as wide frequency range (0.001-10^9 Hz), vast dynamic range (10^{-8}-10^6 psi), high elastic compliance, high mechanical strength and impact resistance. Their acoustic impedance is low and closely matches water, human tissue, and adhesive systems. PVDF can generate voltages 10-25 times higher than piezoceramics for the same pressure input. PVDF is a superior material for sensor because the stress constant of PVDF is more than 20 times bigger than that of PZT as shown in Table 1.1, whereas PZT exhibits a higher strain constant and thus is a good material for actuators. PVDF polymers are quite stable because they can resist moisture, most chemicals, oxidants and intense ultraviolet and nuclear radiation.

PVDF is synthesized by addition polymerization of the CH2=CF2 monomer (Figure 1.7(a)), and exhibits α, β, γ, and δ phases. The γ and δ phases are not common and will not be addressed here. Figure 1.6 shows space-filling model of a segment of a PVDF molecule with omitting hydrogen. The α phase is the lowest energy conformation and non-polar form. The crystal structure of α phase (Figure 1.6(a)) is

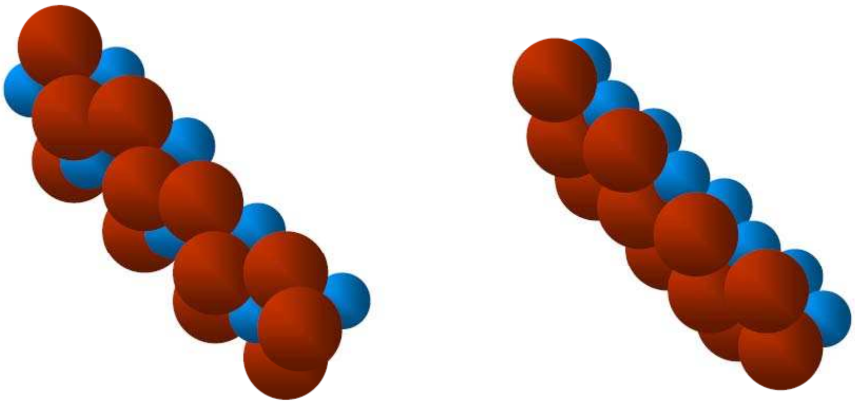
(a) (b)

Figure 1.6: Space-filling model of a segment of a PVDF molecule in the (a) α phase (transgauche conformation), and in the (b) β phase (all-trans conformation) [36].

based on a distorted trans-gauche-trans-gauche' (TGTG') conformation. As one can see in Figure 1.6(a), α phase is more homogenous, which enables it to be stable in nature and is non-polarized because of mixed positive and negative charges. However, the polar β phase exhibits a distorted, planar zigzag, all-trans conformation (Figure 1.6(b)), which has a net dipole moment pointing from the electronegative fluorine to the electropositive hydrogen, produces a net dipole moment nearly normal to the polymer chain [63].

Defect groups of head to head (by definition the CF2 groups are referred to as the “head” and the CH2 groups as the “tail”) and tail to tail (Figure 1.7(b)) are believed to be responsible for the formation of β phase and hence for the piezoelectric properties [14]. Under general polymerization conditions the amount of defect groups accounts for about 3.5-6% of the total synthesizations, although higher ratios of defect groups have been achieved via a special synthesis route [8]. A very popular

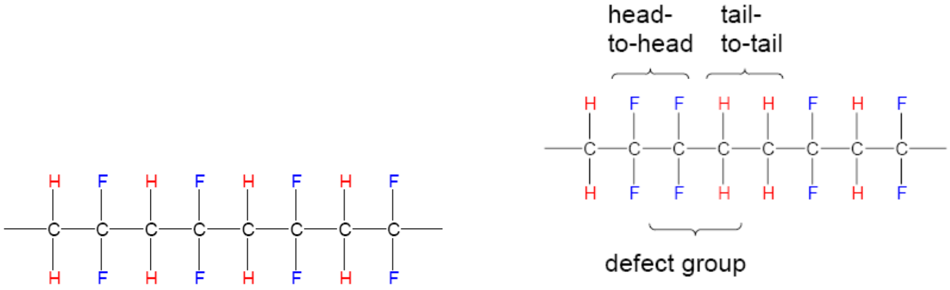

(a) (b)

Figure 1.7: PVDF polymerizations in (a) CH2=CF2 monomer and (b) defect groups (head-to-head and tail-to-tail) [14].

method to artificially introducing defects into PVDF is by use of a comonomer such as trifluoroethylene (TrFE). TrFE is similar to vinylidene fluoride, but with one of the hydrogens replaced by an extra fluorine atom. In essence TrFE is a source of defect groups so that the copolymer with TrFE spontaneously forms the β phase regardless of the processing method. One disadvantage of copolymer is that it has a smaller Curie temperature compared to that of PVDF homopolymer (about 195°C), which could limit its use in some special applications.

1.3.2 Poling Process

Generally speaking, in order to obtain β-PVDF film it is necessary to stretch the inactive α-PVDF film up to four times of its original length, then expose the sample to a very high electric field at elevated temperature, and finally the temperature is then lowered in the presence of the electric field so that the domains are locked in the polarized state. The second step is called “poling process”. After the poling process, the random dipolar moments tend to align along the direction of the external longitude electric field. The stretching process alone does not induce a complete α to β transformation. While the theoretical results of molecular dynamics (MD) carried out by Ramos et al. suggest that this transformation can also be achieved without mechanical stretching, when a sufficiently strong electric field (e.g., 100 MV/m) is applied [63]. Perlman et al. also found that the piezoelectric and pyroelectric constant of PVDF films and copolymers can be increased by nearly 200% when they are simultaneously subjected to stretching and poling process [60]. Non-porous PVDF films with very high ratios of β phase was obtained via a very high pressure applied to porous PVDF films [43]. Poling processes in PVDF are still quite empirical because a thorough understanding of the physical processes involved in poling has not been fully established. There are typically two common techniques for polarization induction of PVDF films: electrode and corona poling.

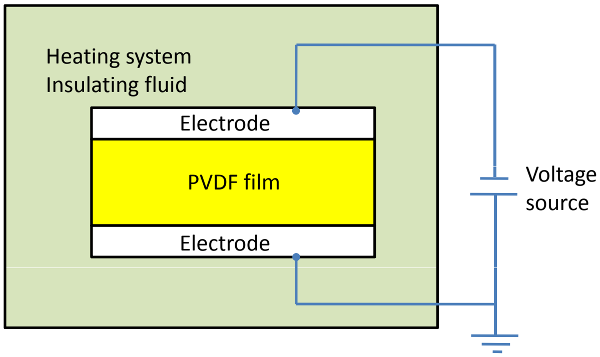

Figure 1.8: Schematic of the electrode poling system.

Figure 1.8 shows the schematic diagram of the electrode poling system [14]. The conducting electrodes (top and bottom), which are either evaporated, sputtered, or painted on the PVDF film surfaces, are required for poling process. An electric field is produced across the sample when the voltage potential is applied to the electrodes. The poling can be done in air without arcing provided that the electrodes do not reach the edge of the film. Otherwise the PVDF film might need to be placed in a vacuum or submerged in an insulating fluid such as Fluorinert, which can prevent arcing that will damage the material. Either static or sinusoidal electric fields at low frequency (mHz) can be applied to the sample during electrode poling. A constant electric field is held on the sample from 10-30 minutes up to 2 hours. A variable field could reduce the probability of dielectric breakdown caused by high voltages for a prolonged period of time [14, 81, 45, 58].

The schematic diagram of corona poling is shown in Figure 1.9. The bottom surface with electrode is placed on a heating plate and connected to the ground. A corona tip is suspended above the sample and is applied to high (8-10 kV) voltages. The grid is usually placed at the distance of 3-4 mm from the sample to control the magnitude of the applied electric field. When the corona discharge is triggered, the ionized particles are accelerated towards the ground and deposited on top surface of the sample, which forms the poling electric field between the top surface and the ground. Corona poling is useful for large area poling and essentially it generates electrodes during the poling. The downside is that it is more difficult to setup and optimize compared to the direct electrode poling [14, 33].

The magnitude of the electric field and sample temperature are the key for the poling process. Generally speaking, the higher the applied electric field, the higher the induced polarization provided that the poling field is larger than the coercive field of PVDF. The coercive field for PVDF and its copolymers is generally between 50

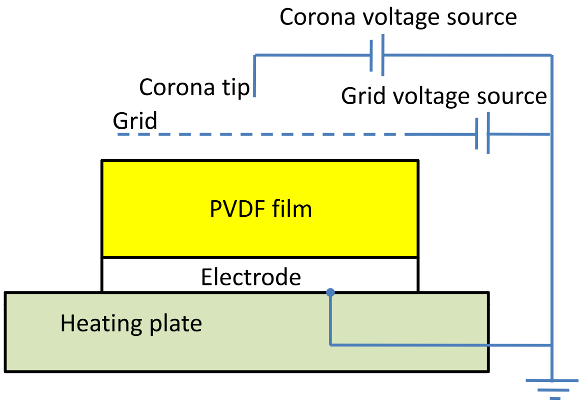

Figure 1.9: Schematic of the corona poling system.

and 120 MV/m [14, 15]. An elevated temperature in the range of 85-130 °C improves dipole mobility and hence increases the material polarizability.

1.4 Literature Review on PVDF and Microphone

Sensors based on PVDF film are attractive due to their high sensitivity and low cost. For example, an in-sleep cardiorespiratory monitoring system uses a PVDF film under sheet to detect pressure fluctuation of human subjects who are in-sleep and separate heart beat signals from the respirations. [77]. PVDF film airflow sensors are investigated as an alternative to the nasal cannula for measuring respiratory events [26]. Uncooled infrared (IR) sensors using PVDF thin film are used to detect temperature changes from low levels of incident IR radiation [22]. Bhatti et al. (2002) proposed an optical antenna using D-fibre for radio-over-fibre applications [4]. The optical D-fibre carrying a transversely poled PVDF polymer coating was modeled by using three-dimensional stress analysis. The response of the D-fibre antenna was determined over a wide frequency range from 1 to 700 MHz. Wang et al. [80] developed a PVDF sensor array for measurement of the impulsive pressure generated by cavitation induced by bubble collapse. A laser micro-machining technique was used to fabricate the PVDF sensor array and each sensor has a sensing area of 4.8×4.8 mm^2 and a height of 25 μm. The capacitance is determined by overlapping isolated electrodes from both sides, which forms the sensing area. It was shown that this sensor can measure the fast-rising gas dynamic shock as fast as 31 ns, while measurements of impact signals from a dropping ball show an insignificant crosstalk level of less than 2%. Toda (2001) proposed a phased-matched ultrasonic transducer based on corrugated PVDF film [70]. In order to obtain the resonant effect of the transducer, the transducer height was chosen as a half of the acoustic wavelength. In this design, PVDF was formed into alternating concave and convex multiple curved sections that eliminates clamps. A strong acoustic beam is formed when corrugation height is approximately one-half of the wavelength. In 2006, Toda et al. developed a novel contact vibration sensor made by bonding a piezoelectric PVDF film to a curved frame structure and a rubber piece with a front contact face [72]. Pressure perpendicular to the PVDF film surface, transmitted from the rubber face, is converted to the internal circumferential stress that induces an electric charge due to piezoelectric effect. An accelerometer mounted between the rubber face and a rigid vibration exciter plate was used to investigate the frequency response of the device, which shows the sensitivity has a flat range from 16 Hz to 3 kHz and a resonance peak at 6 kHz.

Cochlea-inspired transducers investigated by Grosh et al. [28, 82] could achieve levels of miniaturization not possible with existing devices. A flexible tensioned membrane with an exponentially tapered width is employed to obtain a varying acoustic impedance, which can achieve cochlear-like frequency-position mapping. A rigid-walled duct filled with silicone oil is implemented to mimic the environment of the passive mammalian cochlea. Arnold et al. [3] designed a piezoresistive silicon microphone for aeroacoustic measurements that feature small size, high dynamic range, large frequency bandwidth, and low power consumption. The microphone consists of four dielectrically-isolated, single crystal silicon piezoresistors mounted on the top surface of a circular, tensile silicon nitride diaphragm. Several devices were investigated to characterize linearity, frequency response, drift, noise, and power. The sensors show a linear response up to Sound Pressure Level (SPL)160 dB and a 52 dB (SPL) noise floor and consume 15 mW of power when operated at 3 V. Horowitz at al. [32] developed a micromachined piezoelectric microphone for aeroacoustic measurement applications. The microphone was fabricated by combining a lead zirconate-titanate (PZT) deposition process on a silicon-on-insulator wafer with deep reactive ion-etching. An experimental setup in a plane-wave tube was used to characterize the microphone. The device exhibits a sensitivity of 0.75 μV/Pa, a dynamic range of 47.8-169 dB and a resonance frequency of 50.8 kHz. Wang et al. [86] built a PZT-based microacoustic sensor that employs interdigitated electrodes and in-plane polarization instead of commonly used parallel plate-electrodes and through-thickness polarization. The sensitivity is greatly improved because of the small capacitance of the interdigitated capacitor and the large and adjustable electrode spacing, as well as the advantage of the relatively larger piezoelectric stress constant g_{33}. Aoyagi et al.

(2008) developed a capacitive ultrasonic sensor having parylene diaphragm and characterization of receiving performance of arrayed device [2]. An arrayed sensor device comprising 5X5 developed sensors is fabricated and characterized. The developed sensor can receive an impulsive ultrasonic pulse transmitted by a spark discharge and can also be approximated to be non-directional.

1.5 Research Objectives

The goal of this research is to develop an acoustic sensor with superior sensitivity, broad frequency bandwidth, and small footprint. More specifically, the objectives of the research are broadly classified as:

- Packaged in a millimeter-sized enclosure
- Sound Pressure Level of 35 dB - 180 dB (existing 35 - 140 dB)
- Frequency bandwidth of at least 20 Hz to 100 kHz (for micro-pillar based acoustic sensor, it could be up to 1-2 MHz, i.e., ultrasonic range.)

Firstly, regarding the cylindrical curvature microphone based on commercial PVDF film, the author takes advantage of the mature product so that some important/difficult issues such as material polarization and electrode metallization can be avoided. Meanwhile, the author can focus on the investigation and characterization of microphones based on PVDF film and therefore the basic understanding about PVDF microphone is learned/established. Secondly, by developing a microphone based on cross-hair pattern, the author is able to investigate our proposed principle of microphone based on stress amplification as well as patterned electrodes. Finally, the most challenging part of this research is to develop a microphone based on micro-pillar and patterned electrodes. The small size, high stiffness, and reduced mass of MEMS sensors are of great interest because such devices can significantly improve both the temporal and spatial measurement bandwidth. One superior advantage of MEMS sensors is that it can achieve a relative higher area ratio compared to the traditional fabrication processes such as CNC-milling. Lots of significant research issues including micro-fabrication, electrode metallization, poling process, design, signal conditioning, characterization, etc. are fully explored.

1.6 Outline of Dissertation

This dissertation is divided into seven chapters. Chapter 2 focuses on the PVDF rod lumped model, the discrete damped rod model with electromechanical coupling based on piezoelectric constitutive equations and Hamilton's principle, and the curved microphone development and acoustic tests. Chapter 3-5 focus on the acoustic sensors based on stress amplification and patterned electrodes through with design principle, proof-of-concept and validation. As a part of this research, Chapter 6 focuses on micro-tensile machine design and development, and PVDF microfiber characterization.

Chapter 2 presents a PVDF rod lumped model, a discrete damped rod model with electromechanical coupling based on piezoelectric constitutive equations and Hamilton's principle, and design and characterization of a cylindrical curvature microphone based on commercial PVDF film. The lumped model is very important to understand the frequency response of the microphone based on PVDF film and it also define the frequency bandwidth of the system. The simulation results of discrete damped rod model with electromechanical coupling show that the piezoelectric electromechanical coupling increases the overall stiffness of the system if the electrodes are left open and therefore the natural frequencies are smaller if the electromechanical coupling is neglected, which is consistent with the existing literature. The simulation trends demonstrate our models are convergent with the increasing number of elements. Around the natural frequency, the linear piezoelectric constitutive model does not work because it does not include the resonance. The resonance phenomena are observed if we use the dynamic governing equations whether we include the electromechanical coupling or not. A cylindrical curvature microphone is designed and developed to study the sensitivity, frequency bandwidth and other behaviors of the PVDF film based microphone. The acoustic testing results on the curved microphone show that the sensitivity of the microphone is slightly higher than that of the sound level meter in low and high frequency ranges. Further, the involvement of a tube enclosure does not significantly increase the sensitivity. A small resistance value (high cutoff frequency) suppresses the electrical 60 Hz noise, which is always observed and typically significant compared to the signals, but also attenuates the sensor signal.

Chapter 3 is focused on the development of an acoustic pressure sensor with extremely high sensitivity and small footprint. We propose a sensor design consisting of micron-sized PVDF pillars which generate a charge when subjected to normal stresses associated with acoustic waves. The electrode covering the micro-pillars is patterned to decrease the capacitance, and hence increase the sensitivity of the sensor. The key sensor parameters (diameter and height of the micro-pillars, gap between pillar edges, and number of pillars) are determined through a constrained optimization algorithm in which the penalty function is the sensor footprint. The algorithm incorporates the effects of mechanical and electrical properties of the sensor and conditioning amplifier. Details of the fabrication process are described. Nanoindentation tests demonstrate that the PVDF micro-pillar sensor exhibits piezoelectric responses under an applied voltage or strain, thus demonstrating the sensor concept.

Chapter 4 presents the development of an acoustic pressure sensor with extremely high frequency range, wide dynamic range, good sensitivity as well as proof-of-concept of stress amplification through an area ratio and patterned electrodes. This chapter presents the design, sensitivity analysis, finite element analysis, fabrication and testing of a new type of acoustic sensor using PVDF film and crosshair patterned electrodes. Finite element simulations including static structure analysis, modal analysis and harmonic response are performed in ANSYS WORKBENCH to finalize and evaluate the microphone assembly with the design requirements of a frequency range of 100 kHz and a dynamic range of 180 dB. Peak coalescence caused by the first three adjacent natural frequencies and the structure damping ratio is observed and analyzed. The static and dynamic stress distributions make sure of the design within the safety constraint. Experimental setup is developed to characterize the microphone using a commercial available PCB microphone as reference. The theory and design of a circular plane wave tube is presented and the signal conditioning circuit including the preamplifier circuit and the notch filter is also developed. Acoustic tests show that the microphone exhibits a good linearity up to 140 dB (SPL), a relatively flat frequency response up to 10 kHz and a sensitivity of 27.8 mV/Pa. The sensitivity of the sensor itself (without the amplifier) is found to be 27.8 μ/Pa, i.e. 3.01 times the sensitivity of the commercial available PVDF film working in 3-3 mode, which is approximate to the area ratio of 3.2.

Charter 5 presents the fabrication, validation and characterization of a new type of millimeter-size acoustic sensor that uses PVDF micro-pillars and patterned electrodes. The sensor takes advantage of two key design principles: 1) stress amplification mechanism through the area ratio between the overall surface exposed to acoustic waves and the area of the individual micro-pillars; 2) patterned electrodes created to reduce the capacitance of the sensor by excluding the capacitance of the air between micro-pillars. In combination, these design principles enable a sensor which in practice could achieve 100× the sensitivity of flat PVDF film. An analytical sensitivity analysis is presented and sensor fabrication details are described. An experimental setup is developed to characterize the sensor against a commercially available PCB microphone. The theory and design of a circular plane wave tube is presented and the signal conditioning circuit including the preamplifier circuit and notch filter is discussed. Sensitivity calibration tests show that the developed sensor with a gap ratio of 5.8182 exhibits a stress constant of -19.93 V/m/Pa in 33 mode, which is 60.39× bigger than that of commercial available PVDF film. Experimental results also show that the sensitivity of the sensor is in close agreement with theory, thus confirming the performance advantages of the micro-pillar sensor.

In Chapter 6, three main methodologies (i.e., three-point bend test, nanoindentation, and micro-tensile test) for characterization of nanofibers are compared. The advantages and disadvantages of each method is analyzed and discussed. A micro-tensile machine was developed to characterize micro- or nanofibers by incorporating a precision linear actuator (Ultra Motion, Inc.), a mini-load cell (Cooper Instruments and Systems), and a XYZ basis (Sherine, Inc.). Due to the difficulty in manipulating and gripping single nanofibers, a special holder for gripping fibers was designed and developed, which is found to be more convenient than the holder used in commercial micro-tensile machines. Displacement and force resolutions of the developed system are further analyzed. The highest displacement of the system can be 12.7 nm and while the best force resolution is found to be ∼6 μN (p-p) by using the amplifier gain of 1000, 10 Hz low pass filter, and 10 V of the excitation voltage. The force time trace, force-displacement curve, and stress-strain curve for a PVDF single microfiber are obtained through the tensile test. Material creep phenomenon is clearly observed. It is also found that the fiber exhibits a significant large strain (more than 200%), which is not commonly seen in the normal elastic materials. The electrospun PVDF fiber is found to exhibit a Young's Modulus of ∼300 MPa, which is about 1/10 of that of commercially available PVDF film. The reasons for the difference are discussed.

Chapter 7 provides the main contributions to the field. Further, the summary results and finding of this work are presented as well. Some possible future research opportunities are also discussed.

CHAPTER 2

MODELING AND CURVED MICROPHONE

This chapter presents a PVDF rod lumped model, a discrete damped rod model with electromechanical coupling based on piezoelectric constitutive equations and Hamilton's principle, and design and characterization of a cylindrical curvature microphone based on commercial PVDF film. The lumped model is very important to understand the frequency response of the microphone based on PVDF film and it also define the frequency bandwidth of the system.

For materials that are non piezoelectric, the mechanical behavior and the electrical behavior are independent from each other. Whereas for piezoelectric materials, their electrical and mechanical behaviors are known to be coupled where the mechanical variables of stress and strain are correlated to each other as well as the electrical variables of electric field and electric displacement. The full thermodynamic derivation should link mechanical, electrical, and thermal effects, where the thermo-electric coupling produces the pyroelectric effect. The ambient temperature change is relatively slow (the change frequency is typically less than 20 Hz) , while PVDF sensor is basically a high pass filter and therefore the signal generated from the slow temperature change can not be detected from the output of the amplifier, which is highly suppressed before the amplifier. Note that our sensor is used for detecting dynamic acoustic pressure including the frequency components from 20 Hz to 100 kHz (or more). Therefore, the thermal influence can be safely neglected. The linear piezoelectric constitutive model include the resonance and the model needs to be combined with the dynamic governing equations of the system so as to see the resonance phenomena.

Taking advantage of commercially available PVDF film so as to avoid some important/difficult issues such as material polarization and electrode metallization, a cylindrical curvature microphone is designed and developed to study the sensitivity, frequency bandwidth, and other behaviors of the PVDF film based microphone. The experimental results provides a basic understanding of PVDF microphone and thus establishes a solid foundation for the development of an ultrasonic acoustic sensor based on PVDF micro-pillars and patterned electrodes, which is our ultimate goal of this research.

2.1 PVDF Lumped Model

A PVDF rod can be modeled as a system consisting of a second-order mechanical system (Figure 2.1(a)) and a first-order electrical system (Figure 2.1(b)). The charge generated by the deformed PVDF rod is

$$q = K_q X_i, \tag{2.1}$$

where K_q is constant (C/m) and X_i is the induced displacement by the external pressure (or force). Then,

$$i = \dot{q} = K_q \dot{X}_i = K_q X_i(s)s. \tag{2.2}$$

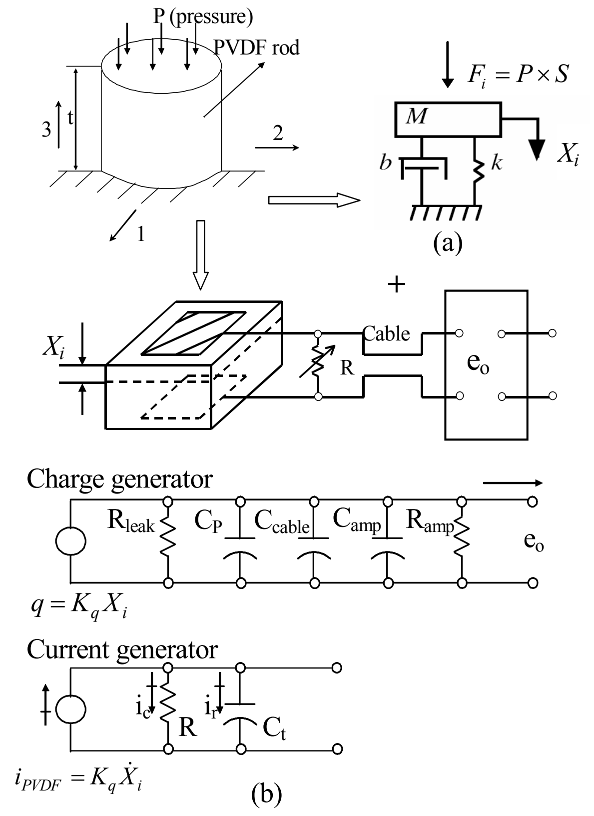

Figure 2.1: PVDF rod model and equivalent circuit.

While,

$$e_o = i\frac{1}{C_t s + 1/R} = K_q X_i(s)s. \tag{2.3}$$

Therefore, the transfer function of the first-order electrical system is

$$\frac{e_o(s)}{X_i(s)} = \frac{G_1 \tau s}{\tau s + 1}, \tag{2.4}$$

where $G_1 = K_q/C_t$ and τ is the time constant of the first-order system. While the transfer function of the second-order mechanical system is

$$\frac{X_i(s)}{F_i(s)} = \frac{1}{Ms^2 + bs + k} = G_2/\left(\frac{1}{\omega_n^2}s^2 + \frac{2\xi}{\omega_n}s + 1\right), \tag{2.5}$$

in which ω_n is the natural frequency of the second order system, ξ is damping ratio, and $G_2 = 1/k$ is the gain of the second order system. Therefore, combination of Eq. (2.5) and (2.4) gives the system transfer function:

$$\frac{E_o(s)}{F_i(s)} = \frac{G_1 \tau s}{\tau s + 1}\left[G_2 / \left(\frac{1}{\omega_n^2}s^2 + \frac{2\xi}{\omega_n}s + 1\right)\right]. \tag{2.6}$$

It is noted that this lumped model can be extended to various PVDF based sensors. If the analytical solution of the second order mechanical system (such as an assembly with complicated structures) is not possible, the natural frequency can be obtained using finite element analysis. This lumped model is very important to understand the fundamental dynamic response of all kinds of PVDF film based applications.

2.2 Discrete Rod Model with Electromechanical Coupling

2.2.1 Piezoelectric Constitutive Equations and Hamilton's Principle

The general constitutive equations commonly used to describe the linear behavior of piezoelectric materials are derived in a straight forward manner from basic thermodynamic principals [34, 69]. Since the independent variables of temperature θ, stress T, and electric field E are chosen for the constitutive equation, then we will use Gibbs free energy as a function. Gibbs free energy is defined by the form

$$G(\theta, T, E) = U - \theta\eta - TS - ED, \tag{2.7}$$

in which U is the internal energy, differentiation of Eq. (2.7) yields

$$dG(\theta, T, E) = -\eta d\theta - SdT - DdE, \tag{2.8}$$

which leads to

$$\eta = \frac{-\partial G}{\partial \theta}|_{T,E} \tag{2.9}$$

$$S_{ij} = \frac{-\partial G}{\partial T_{ij}}|_{\theta,E} \tag{2.10}$$

$$D_n = \frac{-\partial G}{\partial E_n}|_{\theta,T}. \tag{2.11}$$

The dielectric, piezoelectric, thermoelastic, elastic, and pyroelectric material properties are defined by the second derivatives of the Gibbs free energy with respect to the appropriate variables. Then according to Eqs.(2.9-2.11), one can get

$$S_{ijkl} = \frac{-\partial^2 G}{\partial T_{ij}\partial T_{kl}}|_{\theta,E} = \frac{\partial S_{ij}}{\partial T_{kl}}|_{\theta,E} \tag{2.12}$$

$$\epsilon_{mn} = \frac{-\partial^2 G}{\partial E_m \partial E_n}|_{\theta,T} = \frac{\partial D_n}{\partial E_m}|_{\theta,T} \tag{2.13}$$

$$d_{ijk} = \frac{-\partial^2 G}{\partial T_{ij}\partial E_k}|_{\theta} = \frac{\partial D_n}{\partial T_{ij}}|_{\theta,E} = \frac{\partial S_{ij}}{\partial E_n}|_{\theta,T} \tag{2.14}$$

$$p_n = \frac{-\partial^2 G}{\partial \theta \partial E_n}|_{T} = \frac{\partial D_n}{\partial \theta}|_{T,E} = \frac{\partial \eta}{\partial E_n}|_{\theta,T} \tag{2.15}$$

$$\alpha_{ij} = \frac{-\partial^2 G}{\partial \theta \partial T_{ij}}|_{E} = \frac{\partial S_{ij}}{\partial \theta}|_{T,E} = \frac{\partial \eta}{\partial T_{ij}}|_{\theta,E}. \tag{2.16}$$

Therefore, the general piezoelectric constitutive equations are expressed by

$$\{S\} = [s^{E,\theta}]\{T\} + [d^{\theta}]^T\{E\} + \{\alpha^E\}\Theta \tag{2.17}$$

$$\{D\} = [d^{\theta}]\{T\} + [\epsilon^{E,\theta}]\{E\} + \{p^T\}\Theta \tag{2.18}$$

$$\{\Delta\eta\} = [\alpha^E]\{T\} + [p^T]\{E\} + \frac{C^{T,E}}{\theta_0}\Theta. \tag{2.19}$$

Note that these constitutive relations may also be derived if E, S, and Θ are chosen to be independent variables.

If the mechanical strain and the electric field are independent of each other (assuming the constant temperature), the piezoelectric constitutive equations can be written in the form [61]:

$$\{T\} = [c^E]\{S\} - [e]^T\{E\} \tag{2.20}$$

$$\{D\} = [e]\{S\} - [\varepsilon^S]\{E\} \tag{2.21}$$

where $\{T\}$ represents the stress vector, $\{S\}$, the strain vector, $\{E\}$, the electric field, $\{D\}$, the electric displacement, $[c^E]$, the elastic coefficients at constant $\{E\}$, $[\varepsilon^S]$, the dielectric coefficients at constant $\{S\}$, and $[e]$, the piezoelectric coupling coefficients.

The dynamic equations of a piezoelectric continuum can be derived from the Hamilton's principle [48],

$$\delta \int_{t_1}^{t_2} (L + W)dt = 0, \tag{2.22}$$

where t_1 and t_2 define the time interval, L is the Lagrangian and W is the virtual work of external mechanical and electrical forces. The Lagrangian L is defined by the volume integration of the difference of kinetic energy J and electrical enthalpy H. The kinetic energy J can be written in the form,

$$J = \frac{1}{2}\rho\{\dot{u}\}^T\{\dot{u}\}, \tag{2.23}$$

where $\{\dot{u}\}$ is the velocity field. The electrical enthalpy density H of a piezoelectric continuum is defined by

$$H = \frac{1}{2}[\{S\}^T\{T\} - \{E\}^T\{D\}]. \tag{2.24}$$

Therefore, the Lagrangian L can be expressed by

$$L = \int_V (J - H)dV = \int_V [\frac{1}{2}\rho\{\dot{u}\}^T\{\dot{u}\} - \frac{1}{2}[\{S\}^T\{T\} - \{E\}^T\{D\}]]dV \tag{2.25}$$

The virtual work done by the external mechanical forces and the applied electric charges can be written in the form,

$$\delta W = \int_V \{\delta u\}^T\{F_V\}dV + \int_{\Omega_1} \{\delta u\}^T\{F_\Omega\}d\Omega + \{\delta u\}^T\{F_P\} - \int_{\Omega_2} \delta\phi\varrho d\Omega - \delta\phi Q \tag{2.26}$$

where $\{\delta u\}$ and $\{\delta\phi\}$ are respectively the arbitrary variations of the displacement field and the electrical potential, $\{F_V\}$, the body applied forces, $\{F_\Omega\}$ on Ω_1, the surface applied forces, F_P, the point loads, ϕ,the electric potential, ϱ, the surface charge brought on Ω_2, Q, the point electric charges, and ρ, the mass density. Integrating by parts of kinetic energy over the time interval, one gets,

$$\int_{t_1}^{t_2} \rho\{\delta\dot{u}\}^T\{\dot{u}\}dt = [\rho\{\delta u\}^T\{\dot{u}\}]_{t_1}^{t_2} - \int_{t_1}^{t_2} \rho\{\delta u\}^T\{\ddot{u}\}dt. \tag{2.27}$$

Combining Eqs. (2.25), (2.26) and (2.27) with the piezoelectric constitutive equations and substituting them into Hamilton's principle gives

$$\begin{aligned}&\int_V [\rho\{\delta u\}^T\{\ddot{u}\} - \{\delta S\}^T[c^E]\{S\} + \{\delta S\}^T[e]^T\{E\} + \{\delta E\}^T[e]\{S\} + \{\delta E\}^T[\varepsilon^S]\{E\}]dV \\ &= \int_V \{\delta u\}^T\{F_V\}dV + \int_{\Omega_1}\{\delta u\}^T\{F_\Omega\}d\Omega + \{\delta u\}^T\{F_P\} - \int_{\Omega_2}\delta\phi\varrho d\Omega - \delta\phi Q\end{aligned} \tag{2.28}$$

2.2.2 Finite Element Modeling of a Piezoelectric Rod

In the finite element formulation, the displacement field $\{u\}$ and the electric potential ϕ over an element are correlated to the corresponding node values $\{u_i\}$ and ϕ_i by the mean of the shape functions N_u and N_ϕ:

$$\{u\} = [N_u]\{u_i\} \tag{2.29}$$

$$\phi = [N_\phi]\{\phi_i\} \tag{2.30}$$

Also, the strain field $\{S\}$ and the electric field E are correlated to the nodal displacements and potential by the shape functions derivatives $\{B_u\}$ and B_ϕ:

$$\{S\} = [B_u]\{u_i\} \tag{2.31}$$

$$\{E\} = [B_\phi]\{\phi_i\} \tag{2.32}$$

Substituting Eqs. (2.29-2.31) into Eq. (2.28), one can get the discrete governing equations for an element:

$$\begin{aligned}[M]\{\ddot{u}_i\} + [K_{uu}]\{u_i\} + [K_{u\phi}]\{\phi_i\} &= \{f_i\} & (2.33)\\ [K_{\phi u}]\{u_i\} + [K_{\phi\phi}]\{\phi_i\} &= \{g_i\} & (2.34)\end{aligned}$$

with

$$\begin{aligned}
[M] &= \int_V \rho [N_u]^T [N_u] dV & (2.35)\\
[K_{uu}] &= \int_V [B_u]^T [c^E][B_u] dV & (2.36)\\
[K_{u\phi}] &= \int_V [B_u]^T [e]^T [B_\phi] dV & (2.37)\\
[K_{\phi\phi}] &= -\int_V [B_\phi]^T [\varepsilon][B_\phi] dV & (2.38)\\
[K_{u\phi}] &= [K_{\phi u}]^T & (2.39)\\
\{f_i\} &= \int_V [N_u]^T \{F_V\} dV + \int_{\Omega_1} [N_u]^T \{F_\Omega\} d\Omega + [N_u]^T \{F_P\} & (2.40)\\
\{g_i\} &= -\int_{\Omega_2} [N_\phi]^T \varrho d\Omega - [N_\phi]^T Q & (2.41)
\end{aligned}$$

An equivalent discrete model of a piezoelectric rod can be obtained by dividing the rod into equal segments, as shown in Figure 2.2. The new model consists of n equal masses connected by the springs and dampers. The boundary condition is fixed-free. The excitation is the dynamic pressure or force applied to the rod end. The global governing equation can be assembled by the equations for each element, which can be written in the form:

$$\begin{aligned}[M]\{\ddot{U}_i\} + [C]\{\dot{U}_i\} + [K_{UU}]\{U_i\} + [K_{U\Phi}]\{\Phi_i\} = \{F\} && (2.42)\\ [K_{\Phi U}]\{U\} + [K_{\Phi\Phi}]\{\Phi\} = \{G\} && (2.43)\end{aligned}$$

where $[M]$ is mass matrix, $[K_{UU}]$, stiffness matrix, $[K_{U\Phi}]$ and $[K_{\Phi U}]$, piezoelectric coupling matrix, $[K_{\Phi\Phi}]$, capacitance matrix, $\{U\}$, mechanical variables, $\{\Phi\}$, electric

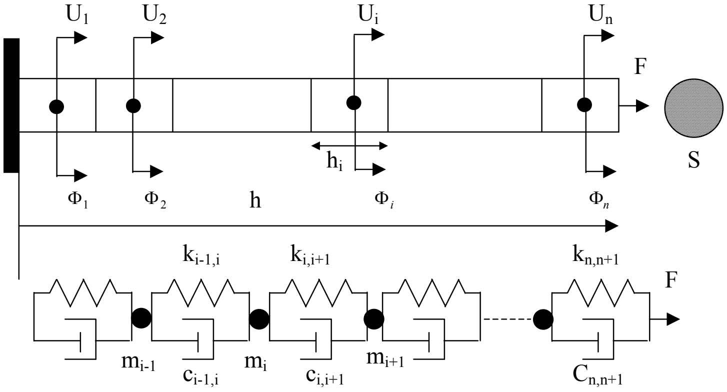

Figure 2.2: Discrete damped rod model with electromechanical coupling.

potentials, $\{F\}$, external forces and $\{G\}$, electric charge brought to the electrodes. These matrices are constructed as follows:

$$M = diag[m_1, m_2, \ldots, m_{n-1}, m_{n-2}] = \rho Sh \cdot diag[m_1, m_2, \ldots, m_{n-1}, m_{n-2}] \tag{2.44}$$

$$C = \begin{bmatrix} c_{0,1}+c_{1,2} & -c_{1,2} & & & \\ -c_{1,2} & c_{1,2}+c_{2,3} & -c_{2,3} & & \\ & \ddots & \ddots & \ddots & \\ & & -c_{n-2,n-1} & c_{n-2,n-1}+c_{n-1,n} & -c_{n-1,n} \\ & & & -c_{n-1,n} & c_{n-1,n}+c_{n,n+1} \end{bmatrix} \tag{2.45}$$

$$K_{UU} = \begin{bmatrix} kuu_{0,1}+kuu_{1,2} & -kuu_{1,2} & & & \\ & \ddots & \ddots & \ddots & \\ & & & -kuu_{n-1,n} & kuu_{n-1,n}+kuu_{n,n+1} \end{bmatrix} \tag{2.46}$$

where $kuu_{i,i+1} = \int_V [B_u]^T [c^E][B_u] dV = \int_V \frac{1}{h_i} Y \frac{1}{h_i} dV = \frac{YS}{h_i}$, for $i = 1, 2, \ldots, n-1$ (when $i = 0$, $h_i = \frac{h_i}{2}$; $i = n$, $kuu_{i,i+1} = 0$). Here, Y and S are Young's modulus and transverse cross-section area respectively. Matrix $K_{U\Phi}$,$K_{\Phi U}$ and $K_{\Phi\Phi}$ have the similar form to that of K_{UU} and the only difference is the corresponding entry (i.e., $ku\phi_{i,i+1} =$

$\int_V [B_u]^T[e]^T[B_\phi]dV = \frac{Yd_{33}S}{h_i}$, $k\phi u_{i,i+1} = ku\phi_{i,i+1}$ and $k\phi\phi_{i,i+1} = -\int_V [B_\phi]^T[\varepsilon][B_\phi]dV = -\frac{\varepsilon S}{h_i}$).

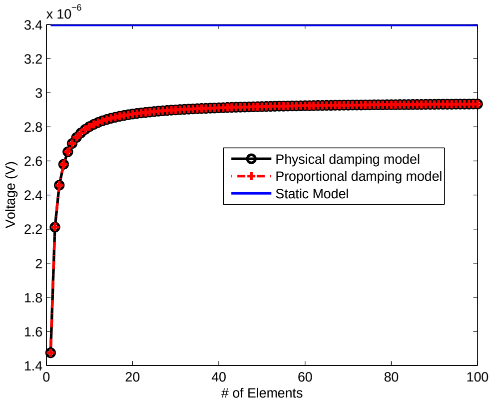

Figure 2.3: Voltage vs. number of elements (Excited by SPL 90 dB at 1 kHz, with electromechanical coupling).

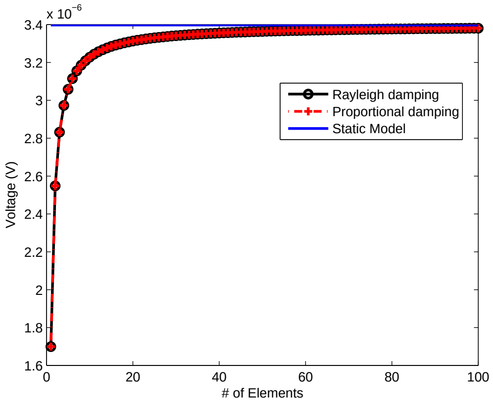

Figure 2.4: Voltage vs. number of elements (Excited by SPL 90 dB at 1 kHz, without electromechanical coupling).

2.2.3 Numerical Solutions

In this section, the numerical solutions of a PVDF rod under the conditions described in Section 2.2.2 are presented. For the rod geometry, the diameter of the rod is 5 μm and the height is 10 μm. For the material properties, permittivity of PVDF is taken as 110e-12 F/m, Young's modulus is 2e9 N/m^2, mass density is 1.78e3 kg/m^3, piezo stress constant g_{33} is -339e-3 v/m/N/m^2 and piezo strain constant d_{33} is -33e-12 m/m/V/m. To complete the numerical simulation, the damping ratio of PVDF, ξ=1.7%, is also used [73]. Either Rayleigh damping or proportional damping is incorporated into the model. It is assumed that the electric boundary condition is open-electrodes, which means $\{G\} = \{0\}$.

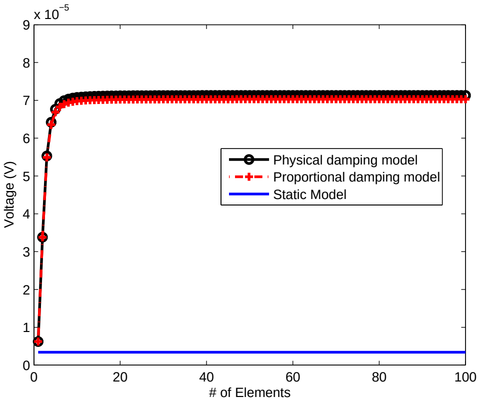

Figure 2.5: Voltage vs. number of elements (Excited by SPL 90 dB at the first natural frequency, with electromechanical coupling).

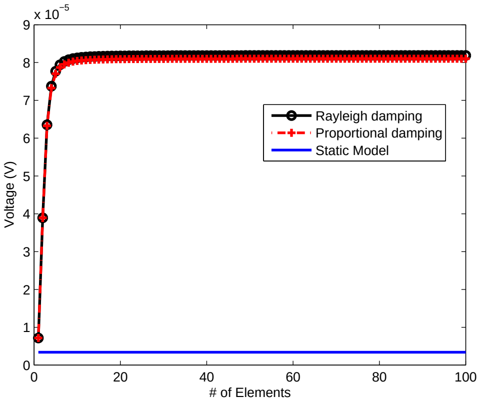

Figure 2.6: Voltage vs. number of elements (Excited by SPL 90 dB at the first natural frequency, without electromechanical coupling).

Tables 2.1 and 2.2 show the first eight eigenfrequencies of a PVDF rod generated with the model with and without electromechanical coupling, respectively. It is shown that the piezoelectric electromechanical coupling increases the overall stiffness of the system if the electrodes are left open (the term $K_{\Phi\Phi}$ being negative) and therefore the natural frequencies are smaller if the electromechanical coupling is neglected, which is consistent with the existing literature. Figures 2.3 and 2.4 show the voltages of a PVDF rod versus number of element with and without electromechanical coupling respectively, when it is exposed to a SPL 90 dB at 1 kHz. In contrast, Figures 2.5 and 2.6 show the comparison results when the rod is excited by the same pressure at the first natural frequency of the rod. The trends demonstrate our models are convergent with the increasing number of elements. There is approximately 15% error between the models with and without electromechanical coupling. Around the natural frequency, the linear piezoelectric constitutive model does not work because

Table 2.1: First eight eigenfrequencies (in Hz) of a PVDF rod with eletromechanical coupling.

n	r=1	r=2	r=3	r=4	r=5	r=6	r=7	r=8
1	2.409e7							
2	2.607e7	6.295e7						
3	2.645e7	7.228e7	9.873e7					
4	2.658e7	7.572e7	1.133e8	1.336e8				
5	2.665e7	7.734e7	1.204e8	1.518e8	1.682e8			
6	2.668e7	7.823e7	1.244e8	1.621e8	1.888e8	2.026e8		
7	2.670e7	7.877e7	1.269e8	1.686e8	2.019e8	2.251e8	2.370e8	
8	2.671e7	7.912e7	1.285e8	1.729e8	2.107e8	2.404e8	2.608e8	2.712e8
100	2.676e7	8.027e7	1.337e8	1.872e8	2.406e8	2.940e8	3.472e8	4.004e8

it does not include the resonance. The resonance phenomena are observed if we use the dynamic governing equations whether we include the electromechanical coupling or not.

2.3 Cylindrical Curvature Microphone

The PVDF film sensors were modeled in beams (Figure 2.7), hemispherical (Figure 2.8)and cylindrical curvature shapes, and the parameters were selected to capture the entire acoustic frequency range. According to the manual of MSI, cylindrical curvature is better than hemispherical curvature because such kind of structure keeps the film smooth and wrinkle free, which reduces distortion and provide a flat frequency response. Through comparison of the models, the cylindrical curvature model in Figure 1.1 shows better properties in terms of size and sensitivity as well as convenience of fabrication.

Table 2.2: First eight eigenfrequencies (in Hz) of a PVDF rod without eletromechanical coupling.

n	r=1	r=2	r=3	r=4	r=5	r=6	r=7	r=8
1	2.385e7							
2	2.582e7	6.234e7						
3	2.619e7	7.157e7	9.777e7					
4	2.633e7	7.498e7	1.122e8	1.323e8				
5	2.639e7	7.659e7	1.192e8	1.503e8	1.666e8			
6	2.642e7	7.747e7	1.232e8	1.606e8	1.870e8	2.007e8		
7	2.644e7	7.800e7	1.256e8	1.670e8	1.999e8	2.229e8	2.347e8	
8	2.645e7	7.835e7	1.272e8	1.712e8	2.086e8	2.380e8	2.583e8	2.686e8
100	2.650e7	7.949e7	1.324e8	1.854e8	2.383e8	2.911e8	3.439e8	3.965e8

2.3.1 Resonance Frequency

The resonance frequency is estimated by

$$f_r \simeq \frac{21}{R(cm)}\ kHz, \tag{2.47}$$

in which R is radius of curvature and f_r is the low frequency corner. Suppose the frequency bandwidth of the microphone is 20-20 kHz, then we can obtain $R \leq 10.5$ cm. It is noted that a typical radius of curvature for piezo film microphones, which optimizes sensitivity and electroacoustic efficiency, is $R = 25$ mm. Therefore, the resonance frequency requires radius of curvature, $R \leq 25$ mm.

2.3.2 Cutoff Frequency

According to Figure 3.6 and the bandwidth requirement, the cutoff frequency constraint is

$$3/\tau \leq 20 \times (2\pi). \tag{2.48}$$

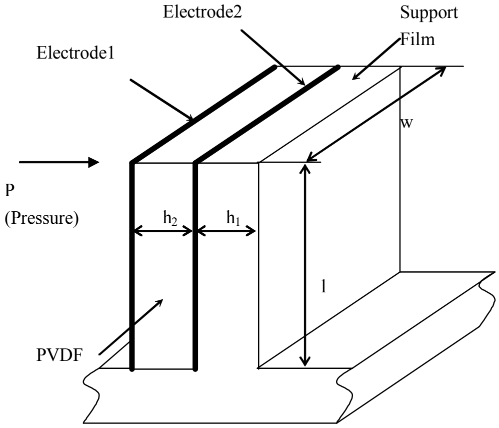

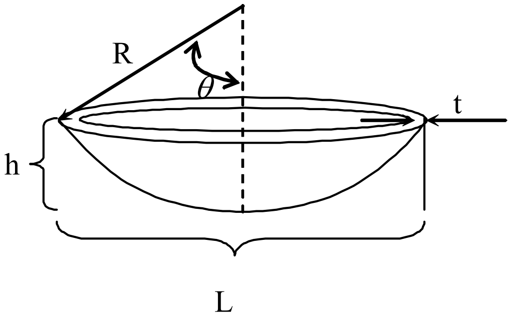

Figure 2.8: PVDF hemispherical model.

Figure 2.7: PVDF beam model.

From Figure 2.1(b), the time constant is $\tau = R_{amp}C_t$. For the case of the cylindrical curvature microphone, the total capacitance of the system is the capacitance of the solid PVDF film (note that the capacitance of the cable and the amplifier is relatively small compared to the capacitance of the PVDF film. The input resistance of Vishay amplifier, 10 MΩ is used for calculation), so that $C_t = C_{PVDF}$. Combining $C_{PVDF} = \epsilon\frac{A}{t}$ and (2.48), one gets that the cutoff frequency constraint is

$$\frac{A}{t} \geq 21.7. \tag{2.49}$$

Substitution of $A = 2R\theta \cdot W$ into the equation above, one can get

$$\frac{2R\theta \cdot W}{t} \geq 21.7, \tag{2.50}$$

where $\theta = arcsin(\frac{L}{2R})$ and W is the width of the film.

2.3.3 Yield Strength

In-plane stress induced in the solid PVDF film can be expressed by

$$\sigma_{\theta\theta} = \frac{(R+t)^2 + t^2}{(R-t)^2 - R^2} \cdot P. \tag{2.51}$$

Considering $R >> t$, one can get

$$\sigma_{\theta\theta} \simeq \frac{R}{t} P. \tag{2.52}$$

Yield strength constraint requires

$$\frac{R}{t} P_{max} \leq \sigma_Y, \tag{2.53}$$

in which P_{max} is the maximum allowable acoustic pressure (SPL=180 dB) and σ_Y is the yield strength of PVDF. Plugging numbers into the equation, one can obtain

$$t \geq 0.00045506R. \tag{2.54}$$

2.3.4 Sensitivity

The open circuit voltage developed across the film thickness is

$$V_o = -g_{31} \cdot \sigma_{\theta\theta} \cdot t = -g_{31} \cdot \frac{R}{t} \cdot P \cdot t = -g_{31} \cdot R \cdot P, \tag{2.55}$$

where g_{31} is the piezoelectric stress constant in the x_1-direction. The static sensitivity is defined as the ratio of the output voltage over the pressure acting on the PVDF material,

$$K = V_o/P. \tag{2.56}$$

Substition of Eq. (2.55) into Eq. (2.57) gives

$$K = -g_{31} \cdot R. \tag{2.57}$$

It is noted that the sensitivity of the microphone is proportional to the radius of curvature, while it is independent of the thickness of the PVDF film. Further, increasing the radius of curvature can lead to the high sensitivity of the microphone, but it will also reduce the frequency bandwidth since the resonance frequency of the microphone is inversely proportional to the radius of curvature as shown in Eq. (2.47). Therefore, a trade-off must be made sometimes in order to meet all the requirements.

2.3.5 Acoustic Tests on the Curved Microphone

We consequently built a microphone based on this cylindrical curvature model with size of 10 mm×6mm×10mm ($R \times L \times W$) and set up an experiment (see Figure 2.9) to detect acoustic signals.

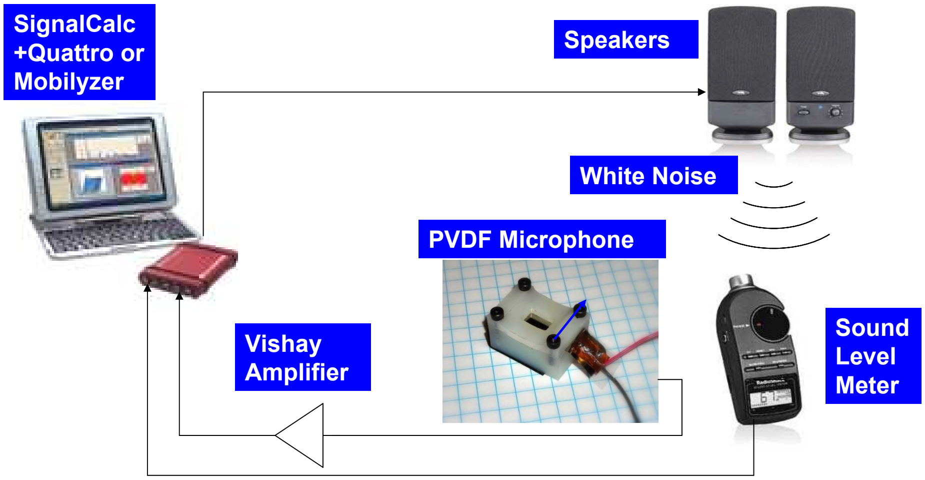

Figure 2.9: Experimental setup.

In order to investigate the frequency responses of the cylindrical curvature microphone under different high-pass filters and different enclosures, the microphone was

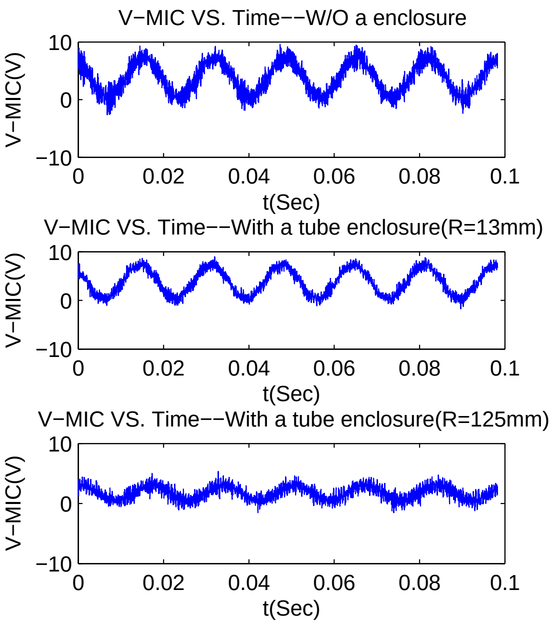

Figure 2.10: Time trace of the microphone under band-limited white noise excitation (f_c=80 Hz).

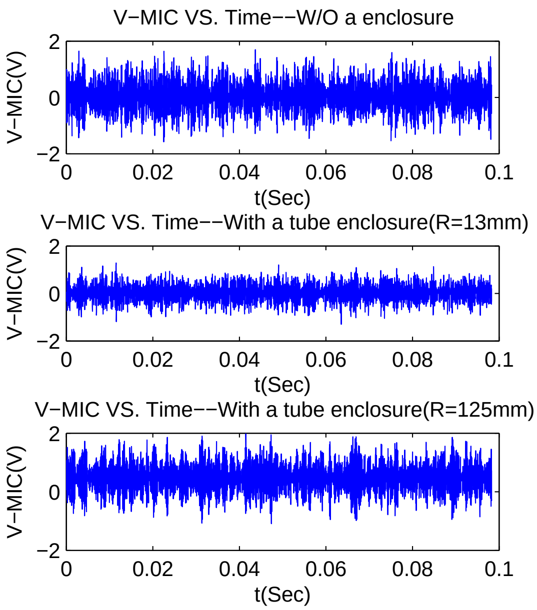

Figure 2.11: Time trace of the microphone under band-limited white noise excitation (f_c=3400 Hz).

tested in 4 cases as follows: 1) cut-off frequency f_c=80 Hz, 2) cut-off frequency f_c=204 Hz, 3) cut-off frequency f_c=3400 Hz, and 4) cut-off frequency f_c=27 kHz. For each case, the microphone was also tested in air, in a small enclosure of tube (R=13mm) and in a big enclosure of tube (R=125mm). All the tests are under band-limited white noise excitation, which includes the frequency components from 0 to 10 kHz. The sound level meter (SLM), acting as a reference, responds mainly to the frequency range of 32 -10 kHz. Figures 2.10 and 2.11 shows the time trace of the microphone with a high pass filter f_c=80 Hz and f_c=3400 Hz, respectively. The 60 Hz electrical noise is suppressed in the latter case.

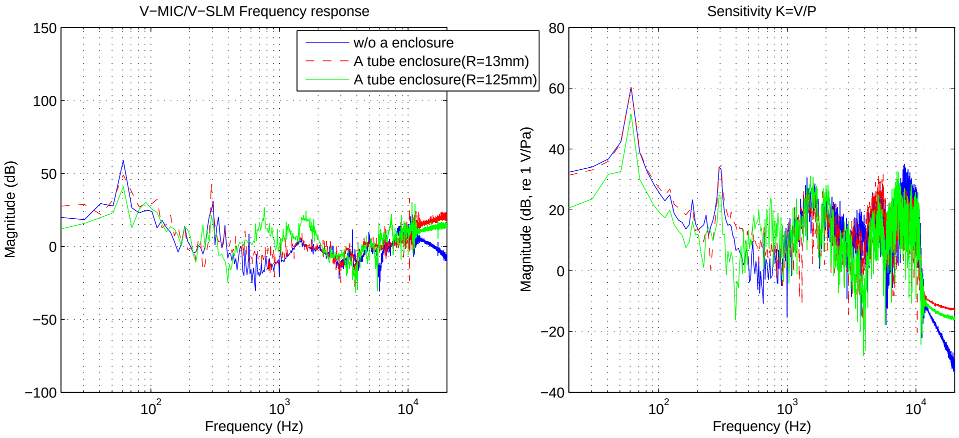

Figure 2.12: Comparison of the sensitivity of a curved PVDF film based microphone with a commercial sound level meter (f_c=80 Hz, amplifier gain=400).

Frequency response experiments were conducted under band-limited white noise excitation and the results were compared with the output of a commercial sound level meter. Figure 2.12 shows the relative sensitivity compared to the results from the sound level meter, and the sensitivity of the microphone itself. The sensitivity of the cylindrical curvature microphone is slightly higher than that of the sound level meter in low and high frequency ranges under the experimental setup shown in Figure 2.9. In addition, the involvement of a tube enclosure does not significantly increase the sensitivity. Figures 2.13 and 2.14 compare the sensitivity frequency response with different filters, in air and a small enclosure of tube, respectively. A small resistance value (high cutoff frequency) suppresses the electrical 60 Hz noise but also attenuates the sensor signal. In practice, a band-rejection filter could be a feasible way to resolve this problem.

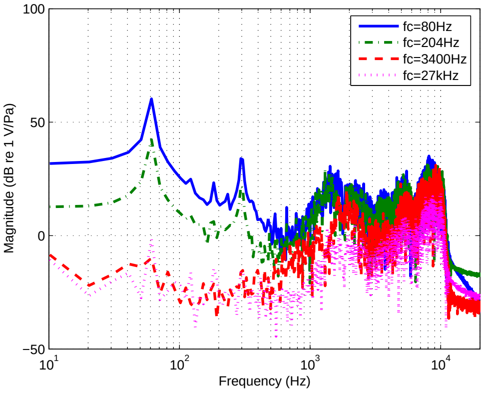

Figure 2.13: Comparison of the sensitivity frequency response with different filters (in air).

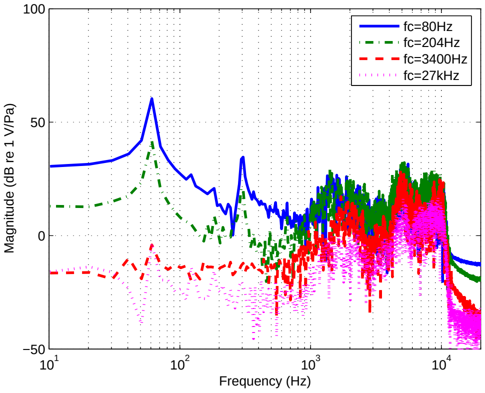

Figure 2.14: Comparison of the sensitivity frequency response with different filters (enclosed a small tube).

2.4 Concluding Remarks

The PVDF rod lumped model shows that a PVDF rod can be divided into a second-order mechanical system and a first-order electrical system. This lumped model is not limited to PVDF rod and can be extended to the other type microphones based on PVDF film. The frequency bandwidth of the microphone is determined by the frequency response of this model. The simulation results of discrete damped rod model with electromechanical coupling show that the piezoelectric electromechanical coupling increases the overall stiffness of the system if the electrodes are left open and therefore the natural frequencies are smaller if the electromechanical coupling is neglected, which is consistent with the existing literature. The simulation trends demonstrate our models are convergent with the increasing number of elements. There is approximately 15% error between the models with and without electromechanical coupling. Around the natural frequency, the linear piezoelectric constitutive model does not work because it does not include the resonance. The resonance phenomena are observed if we use the dynamic governing equations whether we include the electromechanical coupling or not. The acoustic testing results on the curved microphone show that the sensitivity of the microphone is slightly higher than that of the sound level meter in low and high frequency ranges. Further, the involvement of a tube enclosure does not significantly increase the sensitivity. A small resistance value (high cutoff frequency) suppresses the electrical 60 Hz noise (which is always observed and typically significant compared to the signals) but also attenuates the sensor signal. In practice, a band-rejection filter could be a feasible way to resolve this problem.

CHAPTER 3

MICROPHONE BASED ON PVDF MICRO-PILLARS AND PATTERNED ELECTRODES

This chapter is focused on the development of an acoustic pressure sensor with extremely high sensitivity and small footprint. We propose a sensor design consisting of micron-sized PVDF pillars which generate a charge when subjected to normal stresses associated with acoustic waves. The electrode covering the micro-pillars is patterned to decrease the capacitance, and hence increase the sensitivity of the sensor. The key sensor parameters (diameter and height of the micro-pillars, gap between pillar edges, and number of pillars) are determined through a constrained optimization algorithm in which the penalty function is the sensor footprint. The algorithm incorporates the effects of mechanical and electrical properties of the sensor and conditioning amplifier. Details of the fabrication process are described. Nanoindentation tests demonstrate that the PVDF micro-pillar sensor exhibits piezoelectric responses under an applied voltage or strain, thus demonstrating the sensor concept.

3.1 Design of the Proposed Microphone Based on Micro-pillars and Patterned Electrodes

The voltage produced by a capacitive sensor is given by the ratio between charge and capacitance. The proposed microphone exploits the key advantages of PVDF as a sensor material by means of two key design elements aimed at increasing the charge and decreasing the effective device capacitance (Figure 3.1). The first design element is a stress amplification mechanism through the area ratio between the overall surface exposed to acoustic waves and the area of the individual micro-pillars. Because PVDF responds to stress, this mechanism increases the amount of charge for a given pressure level. A rigid membrane placed between the micro-pillars and the acoustic medium ensures high mechanical coupling. The second design element is a top electrode patterned to cover only the surface of the micro-pillars. Excluding the capacitance of the air between pillars, the design with patterned electrodes reduces the capacitance of the sensor. The individual round electrodes above each micro-pillar are interconnected by means of thin conducting tabs. A continuous, flat electrode is placed underneath the array.

The sensitivity of the proposed microphone is analyzed in Section 5.1 and compared against the sensitivity of two sensors: (i) flat continuous PVDF film and (ii) micro-pillars with full flat electrodes. The optimization algorithm for minimization of the microphone's footprint is presented in Section 3.3. Details on the fabrication of the micro-pillars and characterization experiments aimed at understanding the coupled electromechanical response of the PVDF micro-pillars are presented in Section 3.4.

3.2 Sensitivity Analysis

The static sensitivity is defined as the ratio of the output voltage over the pressure acting on the PVDF material,

$$K = V_o/P. \tag{3.1}$$

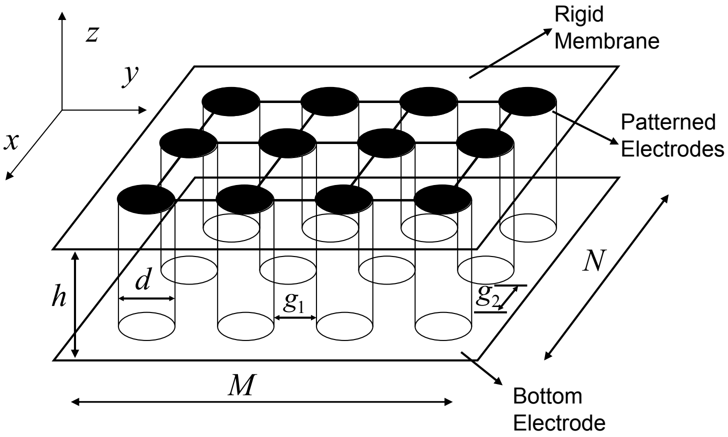

Figure 3.1: Schematic diagram of the proposed acoustic pressure sensor based on PVDF micro-pillars and patterned electrodes. A rigid membrane placed above the micro-pillar array acts as a pressure amplifier. The patterned electrode reduces the device capacitance, thus increasing its sensitivity. h: height of pillars; g_1 and g_2: gap between pillars in the x and y direction; d: diameter of pillars; M and N: pillar numbers in the x and y directions.

The sensitivities of three PVDF sensor designs are compared: flat continuous film, micro-pillars with full electrodes, and micro-pillars with patterned electrodes.

3.2.1 Flat Continuous PVDF Film

Figure 3.2 shows the open circuit of a flat PVDF film sensor. The open circuit voltage developed across the film thickness is

$$V_o = -g_{33} \cdot P \cdot h, \tag{3.2}$$

where g_{33} is the piezoelectric stress constant in the x_3-direction, P is the applied pressure, and h is the thickness of the PVDF film. In this case, the stress induced in the material is equal to the pressure. Substitution of Eq. (4.2) into (4.1) gives the sensitivity as

$$K_1 = -g_{33} \cdot h. \tag{3.3}$$

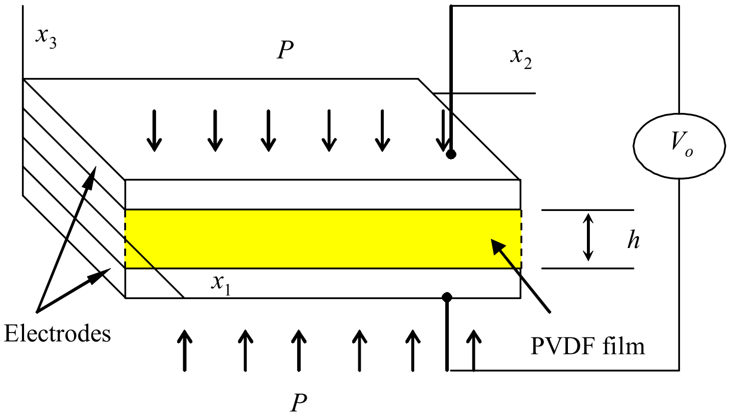

Figure 3.2: PVDF film open circuit.

3.2.2 PVDF Micro-pillars with Full Electrodes

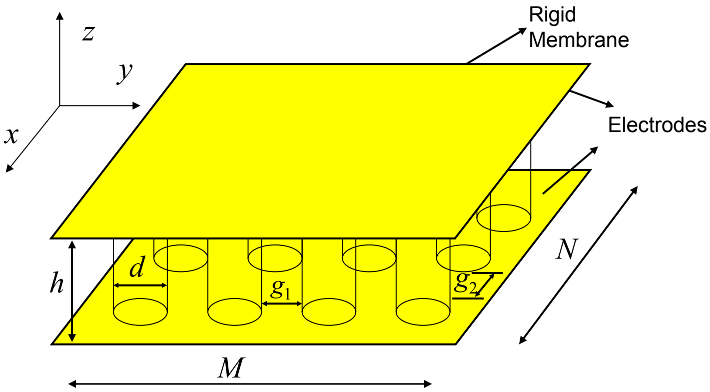

Figure 3.3: Schematic diagram of PVDF micro-pillar sensor based on full electrodes.

Figure 3.3 illustrates the case when an array of micro-pillars is placed between two continuous, flat electrodes. The charge output by the sensor corresponds to the charge generated by the micro-pillars,

$$Q = Q_p \equiv C_p \cdot V_p, \tag{3.4}$$

where Q is the total charge collected at the electrodes, Q_p is the charge generated by the micro-pillars, C_p is the total capacitance of the micro-pillars, and V_p is the potential across the micro-pillars. The total capacitance is, by definition,

$$C_p \equiv \varepsilon \cdot \frac{A}{h} = \varepsilon \cdot \frac{M \cdot N \cdot \pi/4 \cdot d^2}{h}, \tag{3.5}$$

where ε is permittivity of PVDF, M is number of pillars in the x-direction, N is number of pillars in the y-direction, A is the total cross-sectional area of the micro-pillars, and d is the diameter of each micro-pillar. According to the linear constitutive piezoelectric equations, the voltage across the micro-pillars is proportional to the stress,

$$V_p = -g_{33} \cdot h \cdot \sigma. \tag{3.6}$$

The stress on each pillar due to the application of normal pressure on the sensor surface is

$$\sigma = \frac{(d + g_1) \cdot (d + g_2)}{\pi d^2/4} \cdot P, \tag{3.7}$$

where g_1 is gap between pillars in the x-direction and g_2 is the gap between pillars in the y-direction. Substitution of (4.7) into (4.6) gives

$$V_p = -g_{33} \cdot h \cdot \frac{(d + g_1) \cdot (d + g_2)}{\pi d^2/4} \cdot P. \tag{3.8}$$

The total capacitance is the sum of the capacitance of the micro-pillars and the capacitance of the air gap,

$$C_t = C_p + C_o, \tag{3.9}$$

in which the air capacitance is

$$C_o = \varepsilon_o \cdot \frac{M \cdot N \cdot [(d+g_1)(d+g_2) - \pi d^2/4]}{h}. \tag{3.10}$$

Since the two capacitances are connected in parallel, the voltage drop is the same across the micro-pillars and air gap,

$$V_o = \frac{Q}{C_t}. \tag{3.11}$$

Combination of Eqs. (4.4), (4.5) and (4.8)-(4.10) gives the sensitivity of PVDF micro-pillars with full electrodes as

$$K_2 = \frac{\varepsilon_r (d+g_1)(d+g_2)}{\pi d^2/4 \cdot (\varepsilon_r - 1) + (d+g_1)(d+g_2)} \cdot (-g_{33} \cdot h), \tag{3.12}$$

where ε_r is the relative permittivity of PVDF. Assuming without losing generality that $g_1 = g_2 = g$, the sensitivity of the micro-pillar array based on full electrodes relative to the sensitivity of solid PVDF film is

$$K_{r2} \equiv \frac{K_2}{K_1} = \frac{\varepsilon_r (1+g/d)^2}{\pi/4 \cdot (\varepsilon_r - 1) + (1+g/d)^2}. \tag{3.13}$$

The relative sensitivity of the micro-pillar sensor is limited by the relative permittivity of PVDF film, and the upper bound is $K_{r2} = \varepsilon_r$ as g/d goes to infinity.

3.2.3 PVDF Micro-pillars with Patterned Electrodes

In this case both the capacitance and the charge are due solely to the micro-pillars, hence the sensitivity has the form

$$K_3 = \frac{(d+g_1) \cdot (d+g_2)}{\pi d^2/4} \cdot (-g_{33} \cdot h). \tag{3.14}$$

Assuming as before $g_1 = g_2 = g$, the sensitivity of the pillar sensors based on patterned electrodes relative to the sensitivity of PVDF film is

$$K_{r3} \equiv \frac{K_3}{K_1} = \frac{(1+g/d)^2}{\pi/4}, \tag{3.15}$$

which increases monotonically with the ratio of the gap between pillars and the pillar diameter, g/d. The effect of the air gap between pillars is to increase the stress on the sensing material and therefore to increase the sensor's output voltage and sensitivity.

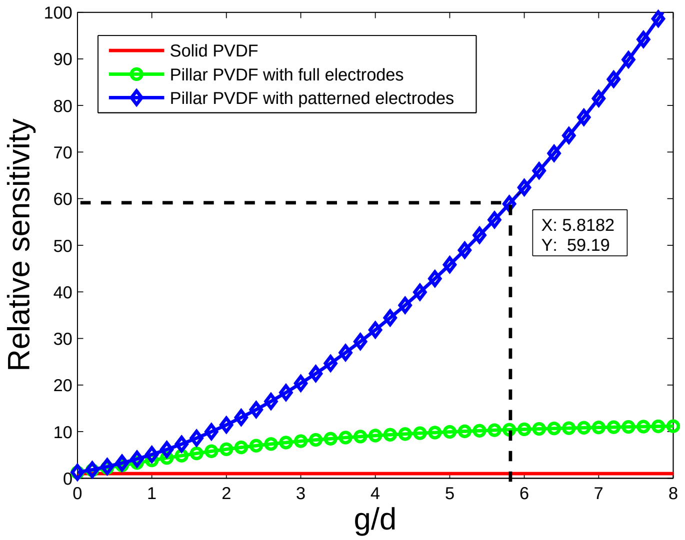

Figure 3.4: Relative sensitivity of the proposed PVDF micro-pillar sensor with patterned electrodes compared to PVDF film and fully electroded micro-pillars. The gaps are assumed equal ($g = g_1 = g_2$).

A comparison of the sensitivities of the two micro-pillar designs relative to that of solid PVDF film is shown in Figure 3.4. The micro-pillar sensor with patterned electrodes theoretically has an unlimited sensitivity with increasing geometry ratio g/d (assuming $g = g_1 = g_2$).

To simplify the design of the micro-pillars with patterned electrodes, we assume that the width of the connecting tabs is negligible compared with the diameter of the micro-pillars. The smallest tab width allowed by our current fabrication techniques

(Section 3.4) is about 2 μm. If the diameter of micro-pillars is not high enough, this factor needs to be included in the calculation of sensitivity.

3.3 Optimization

Nonlinear programming (NLP) techniques are used to find a minimum or maximum of an objective function in N_d dimensions which satisfies arbitrary complex constraints [25]. Many algorithms have been developed for solving such problems, such as Large-Scale Optimization and Medium-Scale Optimization. The large-scale algorithm is a subspace trust region method and is based on the interior-reflective Newton method described in [11]. Each iteration involves the approximate solution of a large linear system using the method of preconditioned conjugate gradients (PCG). The optimization problem can be expressed in the form

$$\begin{cases} minimize & f(x) \\ h_i(x) \leq 0 & i = 1, \ldots, m \\ g_i(x) = 0 & i = 1, \ldots, k \\ l_i \leq x_j \leq u_j & j = 1, \ldots, n \end{cases} \tag{3.16}$$

Here, x is an N_d-dimensional list of design variables; $f(x)$ is the objective function; $h_i(x)$ are inequality constraints; $g_i(x)$ are equality constraints; and $l_i \leq x_j \leq u_j$ are constraints for all design variables.

The functions $f(x)$, $h_i(x)$ and $g_i(x)$ can be any linear or nonlinear combination of the design variables. In this case, a constrained NLP optimization algorithm was developed to obtain the sensor's geometric parameters (M, N, d, g_1, g_2 and h) needed to achieve 100× the sensitivity of existing commercial sensors, dynamic range up to 181 dB, and frequency bandwidth of 100 kHz. The objective function to be minimized is the total sensor area,

$$f(x) = M \cdot N \cdot (d + g_1) \cdot (d + g_2). \tag{3.17}$$

The NLP optimization algorithm was integrated into Matlab.

The design variables that were optimized are M, N, d, g_1, g_2, h and R (total input resistance of the amplifier). The design variables can be treated as independent of each other, while the dependent variables are related by the equality constraints. The total input resistance of the amplifier cannot be chosen arbitrarily as it depends on the actual specifications of available operational amplifiers, although it usually is very high. The height of the pillars is dictated by manufacturing constraints and usually takes values such as 10 μm or 20 μm.

Bounds on the design variables are affected by the ability of the manufacturing process and amplifier input resistance. For this case, they are defined by

$$\begin{cases} 1 \leq M \leq 200 \\ 1 \leq N \leq 200 \\ 1\ \mu\text{m} \leq d \leq 1000\ \mu\text{m} \\ 1\ \mu\text{m} \leq g_1 \leq 1000\ \mu\text{m} \\ 1\ \mu\text{m} \leq g_2 \leq 1000\ \mu\text{m} \\ 1\ \mu\text{m} \leq h \leq 500\ \mu\text{m} \\ 100\ \text{M}\Omega \leq R \leq 1\ \text{T}\Omega. \end{cases} \tag{3.18}$$

The proposed theory has no mechanisms to account for edge effects, though in practice the edges of the electrodes may induce field leakage. In the limit when there is only one pillar ($M = N = 1$), the sensor can still be conceived so long as g_1 and g_2 are defined. In this case, the gaps between pillars do not exist as such but they can be defined at the edge of the sensor. In practice, the number of pillars in each direction must be much bigger than one to minimize edge effects. The determination of geometric parameters that satisfy the various design constraints is presented next.

3.3.1 Resonance Frequency

The basic sensing element, i.e., a PVDF micro-pillar, can be modeled as a continuous rod fixed at one end and free at the other end, as shown in Figure 3.5. Assuming

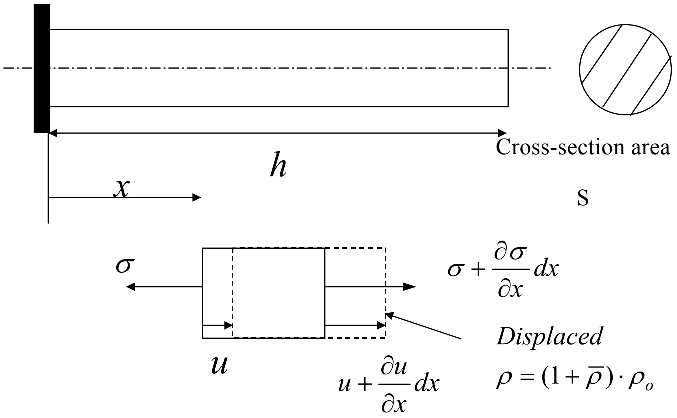

Figure 3.5: Schematic of a continuum rod model.

a slender rod and ignoring inertias and electromechanical coupling, the governing equation for the longitudinal vibrations of a rod is a partial differential equation [35]

$$\frac{\partial^2 u}{\partial x^2} - \frac{1}{c^2}\frac{\partial^2 u}{\partial t^2} = 0, \tag{3.19}$$

where u denotes the axial displacement at position x and time t, and $c = E/\rho_0$, where E and ρ_0 are the Young's modulus and mass density of the material, respectively. Considering fixed-free boundary conditions, the natural frequencies of Eq. (3.19) have the form [5]

$$\omega_r = \frac{(2r-1)\pi}{2h}\sqrt{\frac{E}{\rho_0}}, \quad r = 1, 2, 3, \ldots \tag{3.20}$$

A PVDF rod can be modeled as a system comprising a second-order mechanical system (Figure 2.1(a)) and a first-order electrical system (Figure 2.1(b)). The system transfer function is expressed by

$$\frac{E_o(s)}{F_i(s)} = \frac{G_1 \tau s}{\tau s + 1}\left[G_2/\left(\frac{1}{\omega_n^2}s^2 + \frac{2\xi}{\omega_n}s + 1\right)\right], \tag{3.21}$$

in which τ is the time constant of the first order system, ω_n is the natural frequency of the second order system, ξ is damping ratio, and G_1 and G_2 are the gains of the first order system and second order system, respectively.

The frequency response associated with Eq. (3.21) is shown in Figure 3.6. If the sensor is operated in the flat magnitude range of the frequency response function and the passband error is ±5%, the bandwidth of the system will be from $3/\tau$ to $\omega_n/5$. The desired frequency bandwidth of the acoustic sensor is 20 Hz to 100 kHz, which implies

$$\omega_n/5 \geq 100 \times 10^3 \times (2\pi). \tag{3.22}$$

From Eq. (3.20), the first natural frequency of the PVDF rod (let $r = 1$) is

$$\omega_n = \frac{\pi}{2h}\sqrt{\frac{E}{\rho_0}}. \tag{3.23}$$

Substitution of Eq. (3.23) into Eq. (3.22) and solution for h gives,

$$h \leq 530\ \mu\text{m}, \tag{3.24}$$

which represents the natural frequency constraint.

3.3.2 Cutoff Frequency

According to Figure 3.6 and the bandwidth requirement, the cutoff frequency constraint is

$$3/\tau \leq 20 \times (2\pi). \tag{3.25}$$

From Figure 2.1(b), the time constant is $\tau = RC_t$. For the case of micro-pillars with patterned electrodes, the total capacitance of the system is the capacitance of the pillars. Combining Eqs. (4.5) and (3.25), one gets that the cutoff frequency

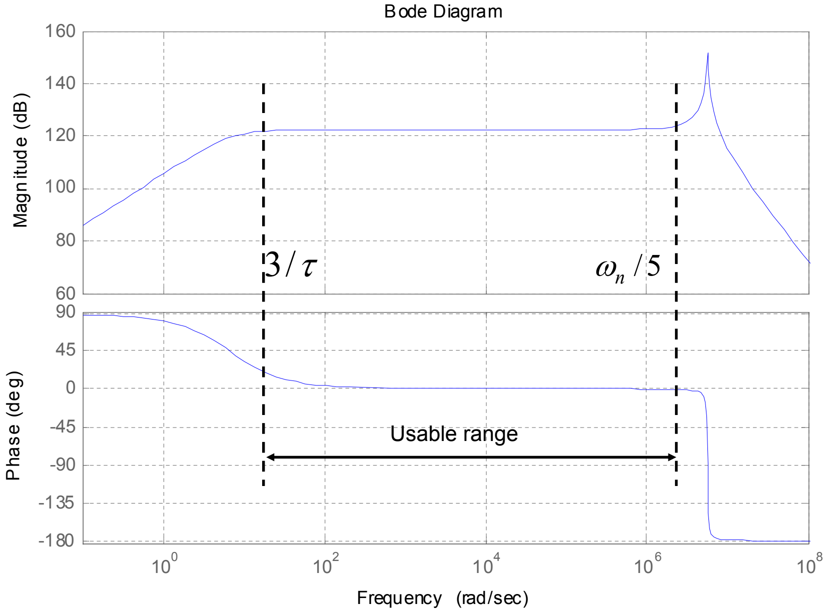

Figure 3.6: Bode plot associated with the electromechanical system shown in Figure 2.1.

constraint is

$$\frac{3h}{R \cdot M \cdot N \cdot \varepsilon \cdot \pi d^2/4} - 40\pi \leq 0. \tag{3.26}$$

3.3.3 Dimensional Limits in the x and y Directions

The acoustic sensor is designed to be packaged in a 9 mm^2 enclosure, which requires that the dimensions in the x and y directions cannot be greater than 3 mm. The dimensional constraints in the x and y directions thus are:

$$M \cdot (d + g_1) - 3 \times 10^{-3} \leq 0, \tag{3.27}$$

$$N \cdot (d + g_2) - 3 \times 10^{-3} \leq 0. \tag{3.28}$$

3.3.4 Sensitivity

Based on the specifications of existing commercial products, the acoustic sensor must have a sensitivity of no less than 0.3 V/psi, i.e., 4.35×10^{-5} V/Pa, before amplification. A gain of 1000 would increase the sensitivity to about the same level as the most sensitive commercial microphones. According to Eq. (4.12), the sensitivity constraint has the form

$$4.35 \times 10^{-5} - (-g_{33}) \cdot \frac{(d+g_1)(d+g_2)}{\pi d^2/4} \cdot h \leq 0. \tag{3.29}$$

3.3.5 Yield Strength

If the sensor is assumed to have a pressure limit equivalent to a sound pressure level (SPL) of 181 dB, the maximum allowable acoustic pressure (P_{max}) is given by

$$20 \log \left(\frac{P_{max}}{20 \cdot 10^{-6}} \right) = 181 \text{ dB}. \tag{3.30}$$

The constraint to avoid surpassing the yield strength of PVDF is

$$P_{max} \cdot \frac{(d+g_1)(d+g_2)}{\pi d^2/4} \leq \sigma_Y \tag{3.31}$$

where σ_Y is the yield strength.

3.3.6 Buckling Load

The Euler formula for columns is

$$F_{max} = \frac{\pi^2 EI}{(rh)^2}, \tag{3.32}$$

where F_{max} is the maximum or critical force (vertical load on a column), E is modulus of elasticity, I is area moment of inertia, h is unsupported length of column, and r is column effective length factor. For both ends pinned, $r = 1.0$; for both ends fixed,

$r = 0.50$; for one end fixed and the other end pinned, $r = 0.70$; for one end fixed and the other end free to move laterally, $r = 2.0$. For the micro-pillar sensor, the buckling load condition is

$$P_{max}(d + g_1)(d + g_2) \leq F_{max}. \tag{3.33}$$

Substitution of Eq. (3.32) into Eq. (3.33) and considering the area moment of inertia of a round pillar,

$$P_{max}(d + g_1)(d + g_2) - \frac{\pi^2 \cdot E \cdot \pi d^2/4}{(r \cdot h)^2} \leq 0. \tag{3.34}$$

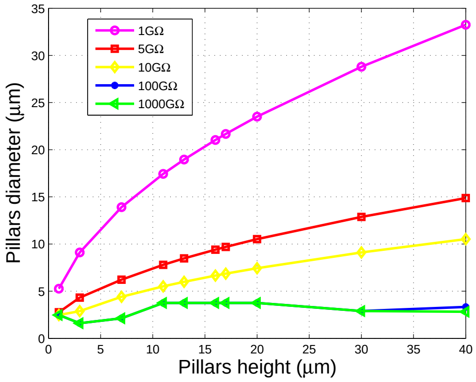

Figure 3.7: Optimal pillar diameter vs. pillar height as a function of amplifier input resistance.

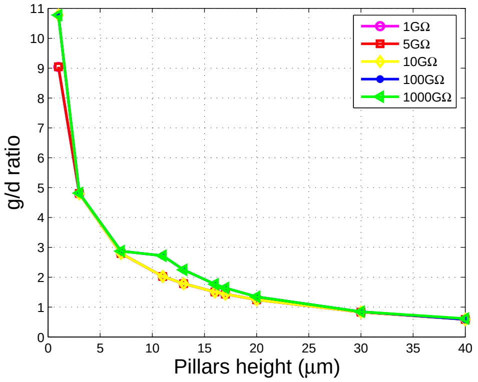

Figure 3.8: Optimal g/d ratio vs. pillar height as a function of amplifier input resistance.

Figures 3.7-3.10 show design curves calculated with the optimization procedure described above. Specifically, the figures show calculations of pillar diameter, pillar gap, g/d ratio and aspect ratio vs. pillar height based on various practical amplifier input resistances ranging from 1 GΩ to 1000 GΩ. These plots provide information on the selection of the amplifier input resistances and the pillar height. Figure 3.7 shows

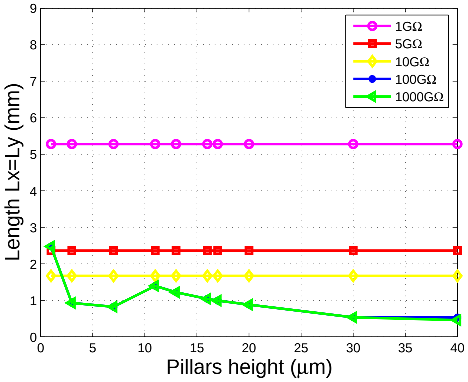

Figure 3.9: Optimal length vs. pillar height as a function of amplifier input resistance.

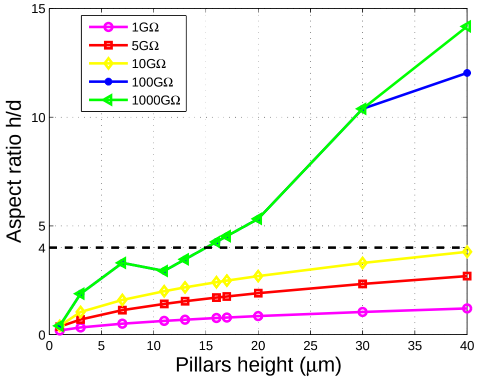

Figure 3.10: Optimal aspect ratio vs. pillar height as a function of amplifier input resistance.

that for $R \leq 10$ GΩ the calculated optimal pillar diameter monotonically increases with pillar height. For higher input resistance values the optimal pillar diameter is approximately constant (2 - 4 μm), i.e., it is approximately independent of pillar height. Figure 3.8 shows that the optimal g/d ratio monotonically decreases with pillar height. Figure 3.9 shows that if the amplifier input resistance is $R \geq 100$ GΩ, an overall sensor footprint of less than 1 mm^2 can be achieved. According to Figure 3.10, if aspect ratios of $g/d = 4$ could be manufactured as is expected to be the case in the near future, any amplifier input resistance from 1 GΩ to 10 GΩ would be suitable. The pillar height should be less than 15 μm if the amplifier input resistance was greater than 100 GΩ. A limit on the pillar ratio of 2 implies either $R = 1$ GΩ combined with arbitrary pillar heights or increasingly higher input resistances combined with increasingly lower pillar heights.

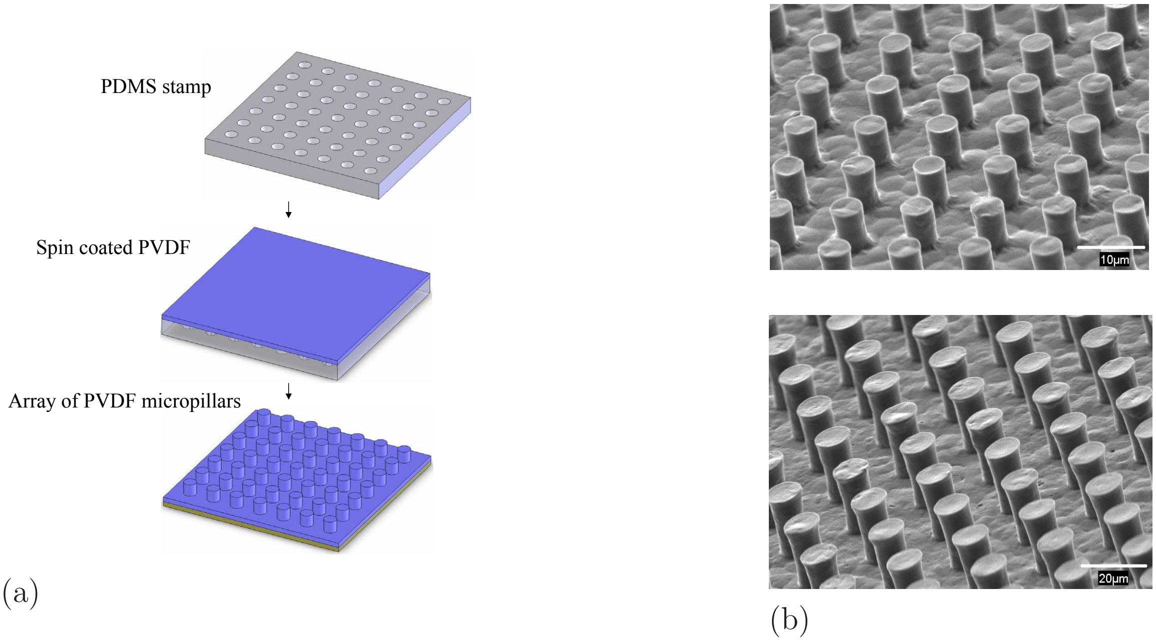

(a)

(b)

Figure 3.11: (a) Fabrication schematic of PVDF micro-pillars. (b) SEM micrograph of ∼5×5 μm pillars (top) and ∼10×20 μm pillars (bottom).

3.4 Fabrication and Characterization of PVDF Micro-structures

Polyvinylidene fluoride (PVDF) micro-structures were fabricated using a procedure which is described in detail elsewhere [23]. Previously patterned polydimethylsiloxane (PDMS) stamps molded from photolithographically fabricated masters were used to obtain arrays of PVDF micro-pillars with designed dimensions (Figure 3.11(a)). A 10% PVDF solution in dimethylacetamide/acetone was spin coated on the PDMS stamps at 1000-2000 rpm for 1 minute. The stamps were placed on a hot plate at 100°C for 5 minutes in order to drive off residual solvent and anneal the PVDF. The spin coated PVDF film was then transferred onto the adhesive side of copper tape using slight pressure. Figure 3.11(b) shows scanning electron micrographs of PVDF pillars with two different micro-pillar dimensions.

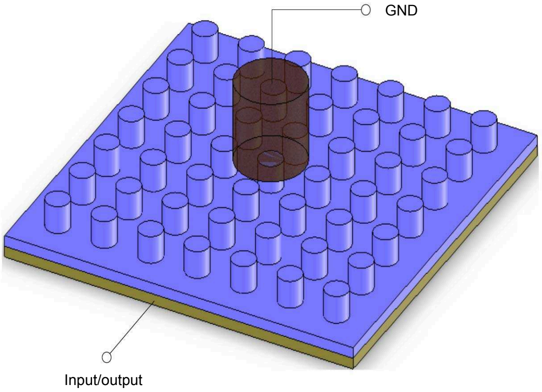

Figure 3.12: Schematic of the indentation test conducted with a nanomechanical test instrument.

Preliminary experiments were conducted with the goal to characterize the piezoelectric response of the PVDF micro-pillars. These proof-of-concept experiments were conducted on a non-optimal micro-pillar array (d= μm, g= 5 μm, h= 6 μm, N=M=1000). A gold-coated glass slide was placed on top of the micro-pillars (top electrode), and an electric field of ∼120 MV/m was applied across the electrodes (top positive and bottom negative) at 160°C for 3 hours, and then at room temperature for an additional hour to pole the PVDF micro-structures. The direct and inverse piezoelectric responses were characterized using a Hysitron TriboIndenter nanomechanical test instrument equipped with the nanoECR package (Figure 3.12) [75]. A boron-doped diamond 14.5 μm flat punch indenter probe was used in the experiments.

The inverse piezoelectric effect was tested by measuring the displacement of a micro-pillar when it is subjected to simultaneous force and voltage inputs. Running the instrument in load-control mode to ensure that a constant preload force of 3 μN was preserved throughout the test, a 40 V pulse was applied across the electrodes.

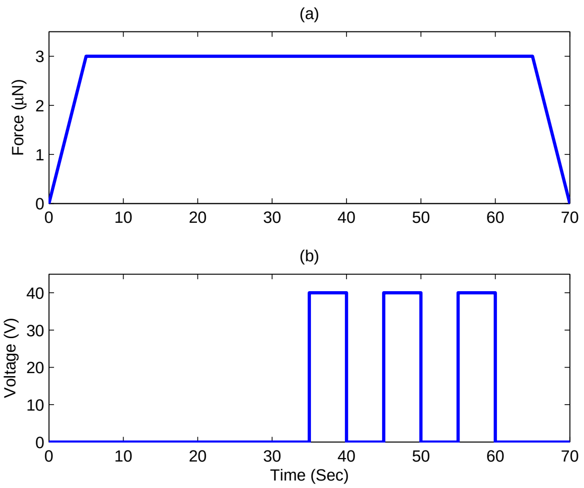

Figure 3.13: Load-controlled nanoindentation inputs of (a) 3 μN force and (b) 40 V square wave.

The preload was gradually applied on a pillar from t= 0-5 seconds and maintained for 60 additional seconds as shown in Figure 3.13(a). The 40 V pulse was applied for 5 second intervals at t= 35, 45, and 55 seconds, as shown in Figure 3.13(b). The sample was subjected to a preload to ensure a good flat contact between the tip of the instrument and the top of the pillar before starting each test. As shown in Figure 3.11(b), the top surface of the PVDF pillars is not completely flat, due in part to the crystalline nature of the polymer. Figure 3.14 shows displacement versus time results. The five lines correspond to five different tests conducted on the same sample. There are two distinct sets of lines, which correspond to two separate sets of tests (conducted 4 days apart). We note that the static displacement differs by about 10 nm for the five measurements. This difference is insignificant considering the dimensions of the pillars (5000 nm). What is important is that the relative change in displacement caused by the 40 V input was very consistent for all five tests. The curves show an average displacement change of approximately 4.4±0.56 nm (strain of ∼0.001) with the applied 40 V pulse. The direct piezoelectric effect was tested by measuring the voltage generated by a micro-pillar in displacement-controlled nanoindentation tests. Figure 3.15 shows force and voltage versus time results. A voltage of roughly 0.18±0.026 V was generated during each test. A total of 5 measurements (represented by 5 different lines) were taken in both characterizations. The results confirm a piezoelectric response of the PVDF micro-pillars under an applied voltage or mechanical input.

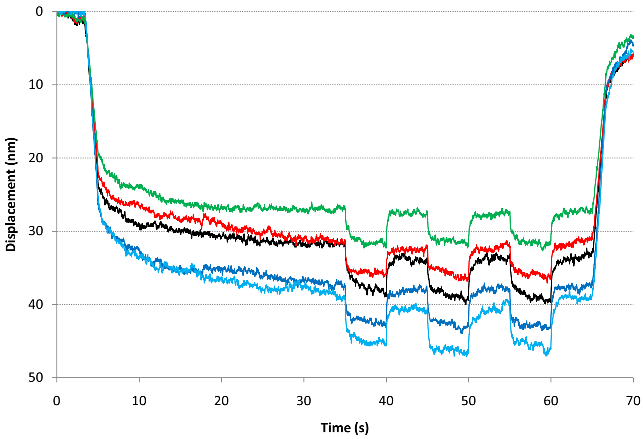

Figure 3.14: Plot of displacement versus time from the 40 V square wave tests.

The piezoelectric constants d_{33} and g_{33} estimated from the data are -110 pC/N and -1092 mV/m/N, respectively [79]. These two values are nearly 3 times greater than those typically reported for flat PVDF films, approximately -33 pC/N and -330 mVm/N, respectively [50]. The high values of these coefficients are consistent with results obtained from microfabricated PVDF from AFM results reported in the

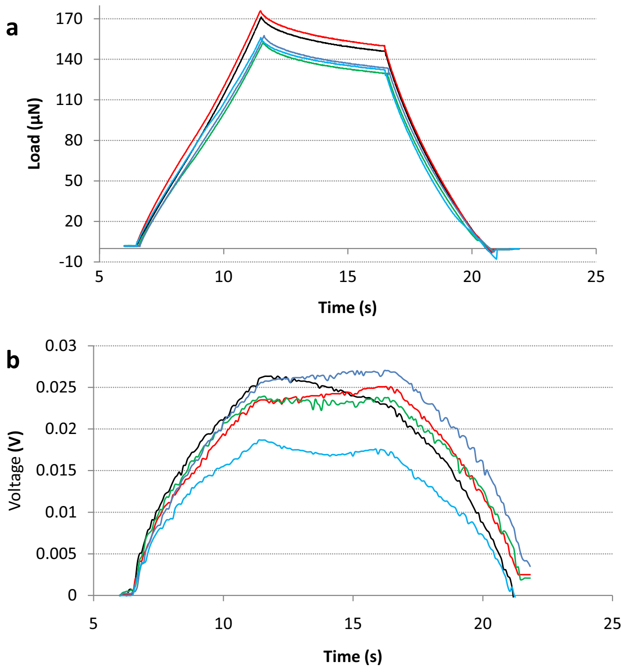

Figure 3.15: Plots of force and voltage versus time for the 4 μm displacement-controlled indents.

literature [6, 42]. The large coefficients could be attributed to several factors including potential effects of micro-structure and electrode geometry and expected differences in mechanical compliance between the micro-pillars and flat PVDF. The micro-pillars are subjected to lower mechanical loading as they are not constrained by surrounding material, hence they are expected to deform more than solid film for a given electric field input [16].

3.5 Discussion

Micro-electromechanical MEMS technology has traditionally been focused on silicon based fabrication techniques. With the development of sacrificial layer micro-molding (SLaM) and patterned substrate micro-molding (PSM), the micro-fabrication of polymer micro-structures is becoming increasingly promising [44, 19]. An acoustic sensor with small size, high sensitivity, wide dynamic range and high frequency bandwidth is of great need due to the special requirements of aeroacoustic and clinical applications. The small size, high stiffness, and reduced mass of MEMS sensors are of great interest because such devices can significantly improve both the temporal and spatial measurement bandwidth. This chapter presents the design, theoretical analysis, micro-fabrication and proof-of-concept characterization of a new type of millimeter-size acoustic sensor using PVDF micro-pillars and patterned electrodes, with the potential to achieve 100× the sensitivity of existing commercial sensors in combination with a dynamic range of 181 dB and a frequency bandwidth of at least 100 kHz. A constrained optimization algorithm has been developed as a function of geometric parameters and electrical parameters of the sensor and conditioning amplifier. A micro-fabrication process of the acoustic sensor based on PVDF micro-pillars and patterned electrodes is described. In order to determine the piezoelectric properties, a PVDF sample that consists of a uniform pattern of 5 μm pillars was manufactured and tested on a Hysitron TriboIndenter nanomechanical test instrument. The nanoindentation testing results show that the PVDF micro-pillar sample exhibits obvious piezoelectric responses under an applied voltage or strain.

One potential application of the proposed micro-acoustic sensor would be vehicle positioning. Like animal echolocation, the vehicle would emit ultrasonic waves and an array of micro-sensors placed on the vehicle skin would measure in real time the echo of the emission (both magnitude and direction). The time difference between the emitted and reflected waves would provide localization of objects around the vehicle and would create safer driving conditions. Spatial location requires pointpoint accuracy, hence sensor dimensions much smaller than possible to fabricate with conventional designs.

This chapter presents the theoretical design and analysis of an acoustic sensor based on PVDF micro-structures. Proof-of-concept of the fabrication of electroactive PVDF micro-structures was presented. Optimal sensor manufacturing and testing is out of the scope of this paper and will be addressed in future work. Future work will be focused on the customized micro-pillar sensor fabrication, amplifier circuit design for the device and acoustic tests. Specialized amplifier circuit design is crucial for acoustic tests of the micro-acoustic sensor. There are three amplifier options for this application: DC coupled amplifier, AC coupled amplifier and DC servo loop amplifier. The advantages and disadvantages of the three amplifier designs will be analyzed. Frequency response analysis, sensitivity calibration, linearity measurement and power spectrum analysis will also be used for the future acoustic tests on the sensor.

CHAPTER 4

DEVELOPMENT OF A PVDF MICROPHONE BASED ON A CROSSHAIR PATTERN WITH AN AREA RATIO AMPLIFICATION

This chapter presents the development of an acoustic pressure sensor with extremely high frequency range, wide dynamic range, good sensitivity as well as proof-of-concept of stress amplification through an area ratio and patterned electrodes. This chapter presents the design, sensitivity analysis, finite element analysis, fabrication and testing of a new type of acoustic sensor using PVDF film and crosshair patterned electrodes. Finite element simulations including static structure analysis, modal analysis and harmonic response are performed in ANSYS WORKBENCH to finalize and evaluate the microphone assembly with the design requirements of a frequency range of 100 kHz and a dynamic range of 180 dB. Peak coalescence caused by the first three adjacent natural frequencies and the structure damping ratio is observed and analyzed. The static and dynamic stress distributions make sure of the design within the safety constraint. Experimental setup is developed to characterize the microphone using a commercial available PCB microphone as reference. The theory and design of a circular plane wave tube is presented and the signal conditioning circuit including the preamplifier circuit and the notch filter is also developed. Acoustic tests show that the microphone exhibits a good linearity up to 140 dB (SPL), a relatively flat frequency response up to 10 kHz and a sensitivity of 27.8 mV/Pa. The sensitivity of the sensor itself (without the amplifier) is found to be 27.8 μ/Pa, i.e. 3.01 times the sensitivity of the commercial available PVDF film working in 3-3 mode, which is approximate to the area ratio of 3.2.

4.1 Design and Fabrication of the Crosshair Pattern PVDF Microphone

Figure 4.1 shows the fabrication process flow for the patterned PVDF microphone. A pattern is placed firmly on the top of a 28 μm thick silver ink metalized polarized PVDF film (1-1004346-0, Measurement Specialties, Inc., USA) by applying M-Bond 200 adhesive (Vishay Micro-Measurements, USA) to the bonding surface of them (Figure 4.1(a)). The next step is to utilize acetone etch the electrodes of the inactive area as shown in Figure 4.1(b). The sensitive area of the microphone is formed by overlapping isolated electrodes from both sides. Third, also using M-Bond 200 adhesive, a rigid membrane is bonded together with the pattern to be subject to external pressure. The two conductive-adhesive coated copper foil tapes (3M 1181) with the wires previously soldered on the surface are adhered to the top and bottom electrodes of the PVDF film (Figure 4.1(c)).

It is noted that the pattern could be created by various techniques such as milling, laser cutting, photolithography etc., which makes this process pliable and less dependent to the manufacturing ability. The user can choose their favorable fabrication method depending on their interests and the fabrication availability. In general, laser cutting and photolithography can achieve a larger area ratio compared with CNC-milling. To fabricate the crosshair pattern, three steps are implemented: 1) a CAD

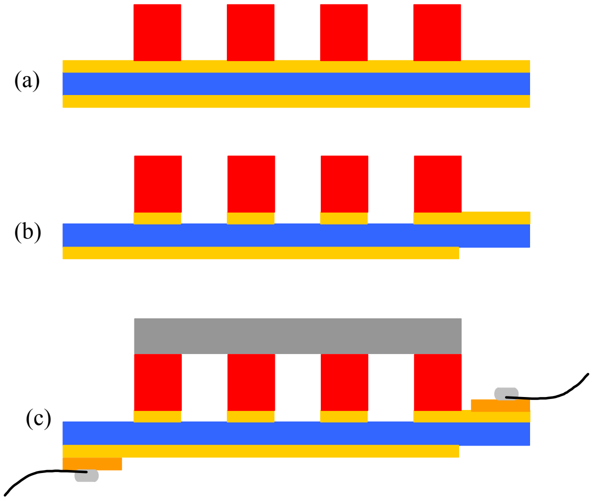

Figure 4.1: Schematic of the fabrication process of the patterned PVDF microphone.

model of the crosshair pattern was developed in Solid Edge. 2) The CAD model was imported into FeatureCAM and FeatureCAM generates CNC G-codes based on user settings. 3) The G-codes was loaded into a Sherline vertical mill (Model 2000) combined with FLASHCUT CNC controller and implemented to fabricate the crosshair aluminum alloy pattern, with an area of about 17.733 mm^2 and a thickness of 0.254 mm (Figure 4.2(a)). A circular aluminum alloy top plate with a diameter of 8.5 mm (i.e., an area of 56.745 mm^2) and a thickness of 0.254 mm was also machined by the CNC-miller in the same way and therefore the area ratio between the pattern and the plate is 3.2. After the crosshair pattern is obtained, the microphone based on this pattern is fabricated by the process as described in Figure 4.1. In addition, if the NiCu alloy metalized PVDF film is used, other etchants such as ferric fluoride solvent might be employed to dissolve the electrodes.

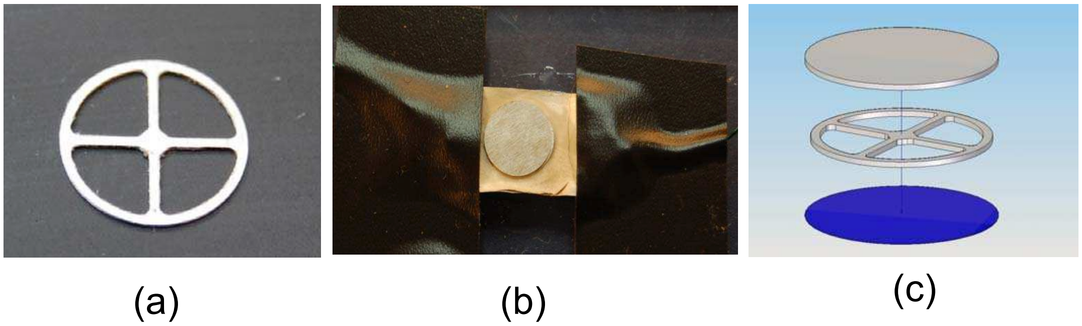

(a) (b) (c)

Figure 4.2: (a) The aluminum crosshair pattern. (b) Photograph of the assembled microphone. (c) Exploded view of the assembly.

4.2 Sensitivity Analysis

The static sensitivity is defined as the ratio of the output voltage over the pressure acting on the PVDF material,

$$K = V_o/P. \tag{4.1}$$

The sensitivities of three PVDF sensor designs are compared: flat continuous film, crosshair PVDF microphone with full electrodes, and crosshair PVDF microphone with patterned electrodes.

4.2.1 Flat Continuous PVDF Film

Figure 3.2 shows the open circuit of a flat PVDF film sensor. The open circuit voltage generated across the film thickness is

$$V_o = -g_{33} \cdot \sigma \cdot h, \tag{4.2}$$

where g_{33} is the piezoelectric stress constant in the x_3-direction, σ is the stress induced in the material (in this case, $\sigma = P$), and h is the thickness of the PVDF film.

Substitution of Eq. (4.2) into (4.1) gives the sensitivity as

$$K_1 = -g_{33} \cdot h. \tag{4.3}$$

4.2.2 Crosshair PVDF Microphone with Full Electrodes

Here, the crosshair PVDF microphone with full electrodes is analyzed. In this case, the crosshair pattern still acts as stress amplification. Without creating patterned electrodes as described in Section 4.1, the charge induced in the material is distributed over the full electrodes. The charge output by the sensor corresponds to the charge generated by the active area (i.e., the area of the crosshair pattern),

$$Q = Q_{ch} \equiv C_{ch} \cdot V_{ch}, \tag{4.4}$$

where Q is the total charge collected at the electrodes, Q_{ch} is the charge generated by the crosshair pattern, C_{ch} is the capacitance of the crosshair pattern, and V_{ch} is the potential across the crosshair pattern. The capacitance is, by definition,

$$C_{ch} = \varepsilon \cdot \frac{A_{ch}}{h}, \tag{4.5}$$

where ε is permittivity of PVDF, and A_{ch} is the total cross-sectional area of the crosshair pattern. According to the linear constitutive piezoelectric equations, the voltage across the crosshair pattern is proportional to the stress,

$$V_{ch} = -g_{33} \cdot h \cdot \sigma. \tag{4.6}$$

The stress on the active area due to the application of normal pressure on the sensor surface is

$$\sigma = \alpha \cdot P, \tag{4.7}$$

where α is the area ratio between the circular top-plate and the crosshair pattern. Substitution of (4.7) into (4.6) gives

$$V_p = -g_{33} \cdot h \cdot \alpha \cdot P. \tag{4.8}$$

The total capacitance is the sum of the capacitance of the active area and the capacitance of the inactive area

$$C_t \equiv C_{ch} + C_{in} = \alpha \cdot \varepsilon \cdot \frac{A_{ch}}{h}, \tag{4.9}$$

where C_{in} is the capacitance of the inactive area. Since the two capacitances are connected in parallel, the voltage drop is the same across the active area and the inactive area,

$$V_o = \frac{Q}{C_t}. \tag{4.10}$$

Combination of Eqs. (4.4), (4.5) and (4.8)-(4.10) gives the sensitivity of PVDF micropillars with full electrodes as

$$K_2 = -g_{33} \cdot h. \tag{4.11}$$

It is interesting that the sensitivity of the crosshair PVDF microphone with full electrodes is same as the flat continuous PVDF film. Although the stress is amplified by the effect of the area ratio, the microphone also introduce the inactive area that leads to an additional capacitance and the charge induced by the active area has to be distributed over the two capacitances, which causes the overall voltage drop. Both effects are cancelled out. This issue is well taken care of in the crosshair PVDF microphone with patterned electrodes that takes advantage of the stress amplification as well as the exclusion of the capacitance of the inactive area.

4.2.3 Crosshair PVDF Microphone with Patterned Electrodes

In this case, both the capacitance and the charge are due solely to the crosshair pattern, hence the sensitivity has the form

$$K_3 = \alpha \cdot (-g_{33} \cdot h), \tag{4.12}$$

which increases monotonically with the area ratio. The crosshair PVDF microphone with patterned electrodes theoretically has an unlimited sensitivity with increasing geometry ratio α.

In Chapter 3, we proposed two designs: PVDF micro-pillars with patterned electrodes (Figure 3.1) and with full electrodes. The sensitivity of PVDF micro-pillars with patterned electrodes is expressed by

$$K_{m3} = \frac{(d+g_1) \cdot (d+g_2)}{\pi d^2/4} \cdot (-g_{33} \cdot h). \tag{4.13}$$

While the sensitivity of PVDF micro-pillars with patterned electrodes has the form

$$K_{m2} = \frac{\varepsilon_r (d+g_1)(d+g_2)}{\pi d^2/4 \cdot (\varepsilon_r - 1) + (d+g_1)(d+g_2)} \cdot (-g_{33} \cdot h). \tag{4.14}$$

Therefore, compared to the flat continuous PVDF film, the sensitivity amplification ratios of PVDF micro-pillars with patterned electrodes and with full electrodes are $(d+g_1) \cdot (d+g_2)/(\pi d^2/4)$ and $\varepsilon_r(d+g_1)(d+g_2)/[\pi d^2/4 \cdot (\varepsilon_r - 1) + (d+g_1)(d+g_2)]$, respectively. A comparison of the sensitivities of the two micro-pillar designs relative to that of solid PVDF film is shown in Figure 3.4. The micro-pillar sensor with patterned electrodes theoretically has an unlimited sensitivity with increasing geometry ratio g/d (assuming $g = g_1 = g_2$).

It is noted that if the area ratios of crosshair PVDF microphone with patterned electrodes and PVDF micro-pillars with patterned electrodes are equal and the transverse stress from the surrounding materials of the former case is neglected (relative smaller compared to the normal stress), both cases have the same sensitivity. However, the relative sensitivity of PVDF micro-pillars with full electrodes is limited by the relative permittivity of PVDF film, $\varepsilon_r =\sim 12$, as g/d goes to infinity, which is different with 1, the relative sensitivity of crosshair PVDF microphone with full electrodes. This is due to the air introduced in crosshair PVDF microphone with full electrodes, which has a different permittivity with the PVDF film. The designs with patterned electrodes exclude this capacitance whether it is from the air or the PVDF film.

4.3 Finite Element Analysis

Considering the requirements for the frequency bandwidth up to 100 kHz and dynamic range up to SPL 180 dB, finite element simulations including static structure analysis, modal analysis and harmonic response are performed in ANSYS WORKBENCH to finalize and evaluate the crosshair pattern PVDF microphone assembly. As shown in Figure 4.2(c), the microphone assembly consists of three components (top circular plate, crosshair pattern and PVDF film), which are imported to ANSYS. Boundary condition between the surfaces of the top plate and the crosshair pattern is bonded, which is applied to the interface between the crosshair pattern and the PVDF film as well. The bottom surface of the PVDF film is fixed.

Figure 4.3 shows the mode shapes of the first four resonant modes of the microphone assembly as predicted by the finite element (ANSYS WORKBENCH) design model. Typically, the fundamental mode is of interest because it determines the frequency bandwidth of the design system. However, in this design, the first four natural frequencies are very close (Figure 4.3) and therefore it is necessary to study

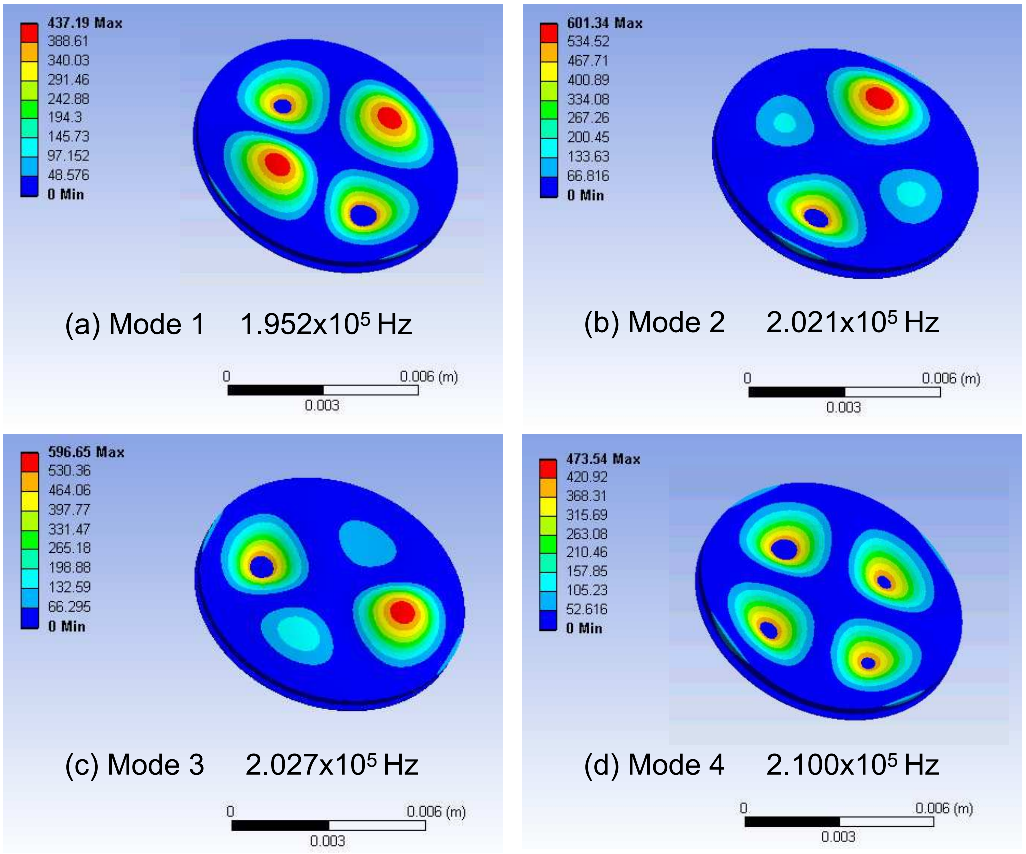

(a) Mode 1 1.952×10^5 Hz

(b) Mode 2 2.021×10^5 Hz

(c) Mode 3 2.027×10^5 Hz

(d) Mode 4 2.100×10^5 Hz

Figure 4.3: The mode shapes of the first four resonant modes of the microphone assembly as predicted by the finite element (ANSYS WORKBENCH) design model.

and analyze all the first four modes. The first mode, having two pairs of holes move out-of-phase, has a predicted resonant frequency of 195.2 kHz while the fourth mode, consisting of in-phase of motion of the four holes, has a predicted resonant frequency of 210.0 kHz. Due to the symmetry of the design, the mode shapes of the second mode and the third mode are 90 degree symmetric. The predicted natural frequencies are 202.1 kHz and 202.7 kHz, respectively. The small difference could be from CAD model conversion, mesh and calculated errors.

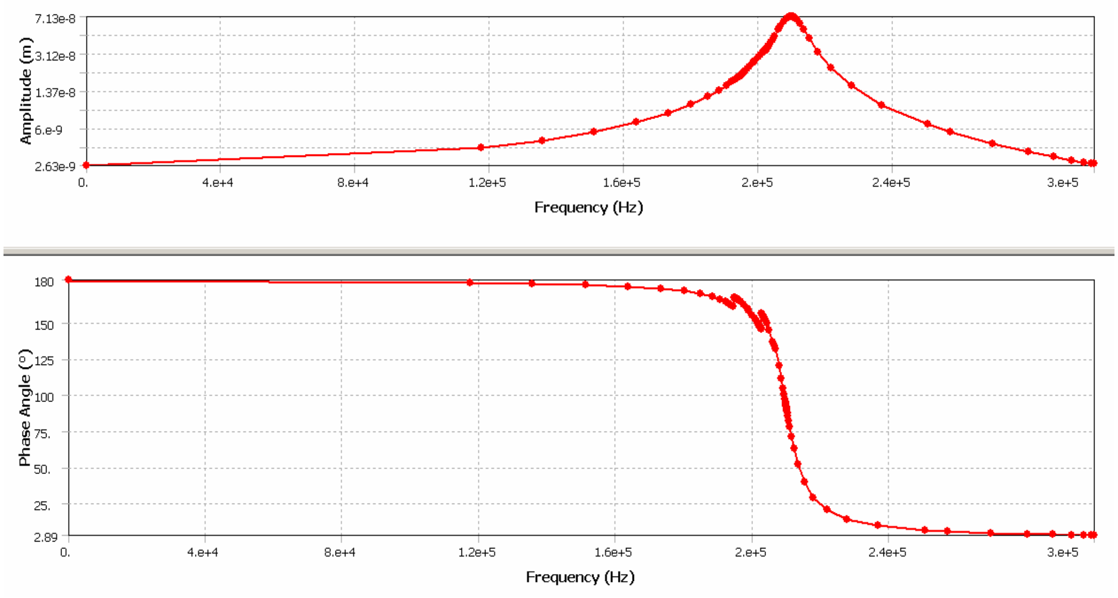

Figure 4.4: Harmonic response of the system (Damping ratio = 2%).

To perform harmonic response analysis, a sound pressure level (SPL = 180 dB) is applied normal to the top plate and the same boundary conditions as described before are used. According to the existing literature [73], commercial PVDF film has a damping ratio of around 1.7% while the damping ratio of aluminum structures is approximately 2%. A damping ratio of 2% is chosen for this simulation. As shown in Figure 4.4, this microphone has a nearly flat response up to 100 kHz, with a phase change less than 3 degree in the frequency range less than 100 kHz. The peak coalescence is clearly observed due to three close natural frequencies. Typically, there are two main factors to lead to peak coalescence: one is calculation resolution of simulation (for instrumentation, frequency resolution of measurement system) and the other is a system with a very big damping leading to the adjacent resonant peaks

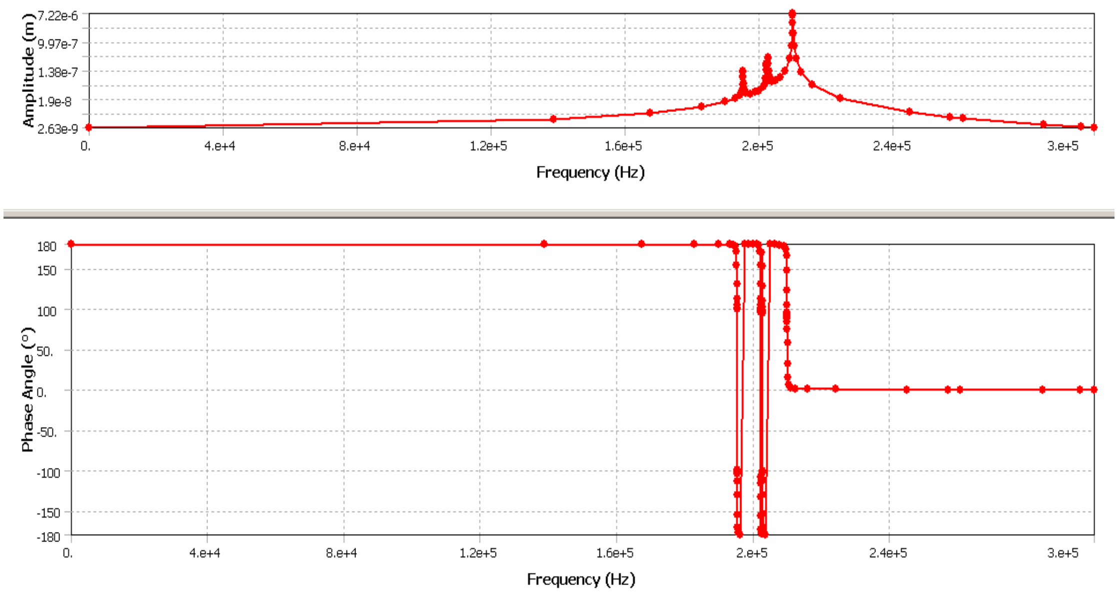

Figure 4.5: Harmonic response of the system (Assuming damping ratio = 0.02%).

coupled together. In order to investigate the reason for this case, a supposed damping ratio of 0.02% is applied to the same structure to run the simulation again. As one can see in Figure 4.5, the other two peaks appear, which verifies that the peak coalescence of this structure is caused by the latter factor.

Stress is also a concern for the microphone assembly design. The microphone is designed to bear a high acoustic pressure (SPL up to 180 dB). An finite element simulation of static structure analysis is also conducted to analyze the stress distribution over the microphone assembly. Figure 4.6(a) shows the static stress distribution over the microphone assembly under SPL 180 dB applied perpendicular to the surface of the top aluminum plate. The maximum equivalent (von-Mises) stress is found to 67.457 kPa, which is much smaller than the yield strength of the PVDF film (45-55 MPa) or that of the aluminum alloy (∼280 MPa). Since the microphone is subject

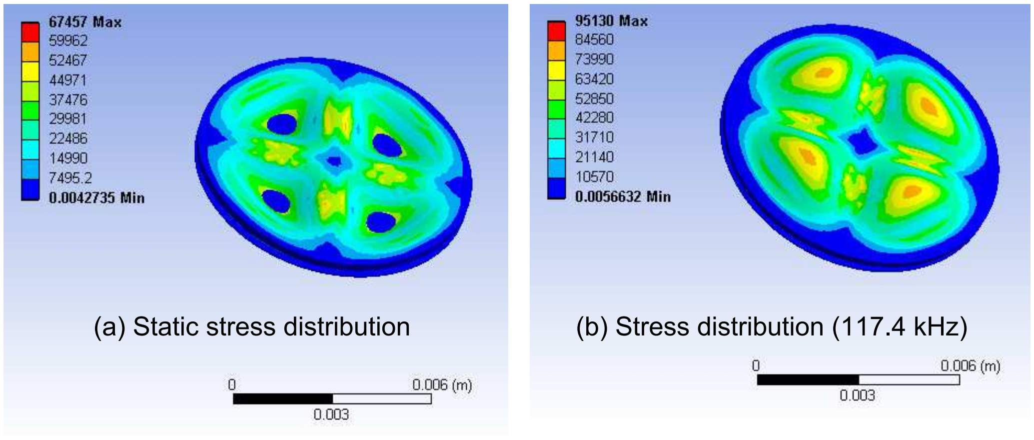

(a) Static stress distribution

(b) Stress distribution (117.4 kHz)

Figure 4.6: (a) Static stress distribution over the microphone assembly. The maximum stress is 67.457 kPa. (b) Harmonic stress distribution over the microphone assembly (at 117.4 kHz). The maximum stress is 95.13 kPa.

to dynamic pressure (SPL up to 180 dB, frequency bandwidth up to 100 kHz), the harmonic stress distribution of SPL 180 dB at 117.4 kHz, as shown in Figure 4.6(b), is extracted from the harmonic response simulation. The maximum dynamic stress of 95.13 kPa is obtained. This maximum dynamic stress is bigger than that of static pressure, but it is also much smaller than the yield strengths of two materials.

4.4 Experimental Setup and Results

The experimental setup shown in Figure 4.7 is developed to conduct various acoustic tests including relative sensitivity response, sensitivity calibration and sensor linearity. To calibrate the dynamic response of the microphone, a speaker, driven by the sinusoidal wave or band-limit white signal generated from USB data acquisition system Quattro, is attached to one end of a circular plane wave tube (PWT). A commercial available microphone, PCB 130C10, is used as reference. The crosshair

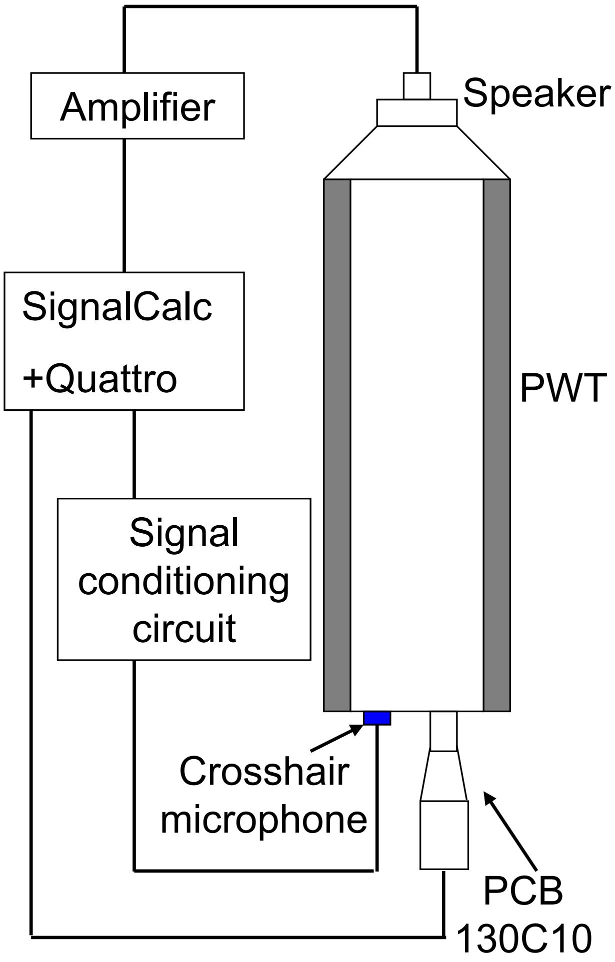

Figure 4.7: Schematic of experimental setup.

microphone is placed at the opposite end of the PWT next to the commercial microphone. A PWT is used to only propagate the fundamental mode (0,0) plane wave and make sure that the higher order modes are evanescent for various acoustic tests. The signals induced from the crosshair microphone is processed by the signal conditioning circuit and fed into the data acquisition system (Quattro+SignalCalc) while the signals from the commercial microphone are also recorded and analyzed by the data acquisition system with the interface of ICP coupling. How to design circular PWT and the signal conditioning circuit is discussed next.

4.4.1 Circular Plane Wave Tube Design

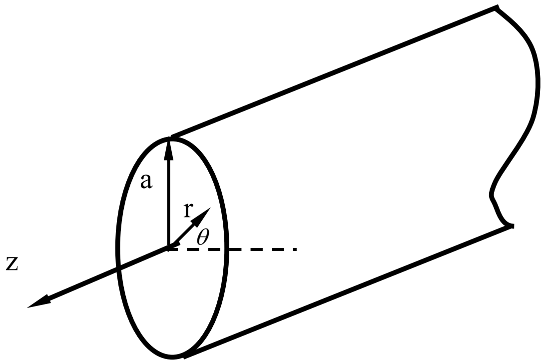

Figure 4.8: Infinite circular tube with a radius of a.

Assuming an infinite tube with rigid wall shown in Figure 4.8, the linearized wave equation for the propagation of acoustical waves in cylindrical co-ordinates can be expressed in the form [67, 54]

$$\bigtriangledown^2 \phi(r,\theta,z,t) = \frac{1}{c_0^2}\frac{\partial^2 \phi(r,\theta,z,t)}{\partial t^2}, \tag{4.15}$$

where $\bigtriangledown^2$ is Laplacian operator, ϕ is velocity potential and c_0 is speed of sound. Let $\phi(x,y,z,t) = \phi'(x,y,z)e^{j\omega t}$, then one gets the Helmholtz's equation as

$$\bigtriangledown^2 \phi'(r,\theta,z) = k^2 \phi'(r,\theta,z), \tag{4.16}$$

i.e.,

$$\frac{\partial^2 \phi'}{\partial r^2} + \frac{1}{r}\frac{\partial \phi'}{\partial r} + \frac{1}{r^2}\frac{\partial^2 \phi'}{\partial \theta^2} + \frac{\partial^2 \phi'}{\partial z^2} + k^2 \phi' = 0, \tag{4.17}$$

where k is wave number (ω/c_0) and ω is angular frequency. Considering separation of variables (let $\phi'(r,\theta,z) = R(r)\Theta(\theta)Z(z)$) gives three ordinary differential equations (ODE) as

$$\begin{cases} \frac{1}{R^2}\frac{d^2R}{dr^2} + \frac{1}{rR}\frac{dR}{dr} + \frac{1}{r^2\Theta}\frac{d^2\Theta}{d\theta^2} = -k_r^2 \\ \frac{1}{\Theta}\frac{d^2\Theta}{d\theta^2} = -m^2 \\ \frac{1}{Z}\frac{d^2Z}{dz^2} = -k_z^2, \end{cases} \tag{4.18}$$

where $k_z^2 = k^2 - k_r^2$. The solutions of the second and third ODEs are $\Theta(\theta) = A_\theta e^{-jm\theta} + B_\theta e^{jm\theta}$ and $Z(z) = A_Z e^{-jk_z z} + B_Z e^{-k_z z}$, respectively. The first ODE can be transformed to

$$r^2\frac{d^2R}{dr^2} + \frac{1}{r}\frac{dR}{dr} + (k_r^2 r^2 - m^2)R = 0, \tag{4.19}$$

which is known as m order Bessel's equation and the solution is given by $R(r) = A_r J_m(K_r r) + B_r N_m(K_r r)$, where J_m and N_m are Bessel and Neumann function of order m respectively. Therefore, the overall solution is

$$\begin{aligned} \phi(r,\theta,z,t) =& [A_r J_m(K_r r) + B_r N_m(K_r r)][A_\theta e^{-jm\theta} + B_\theta e^{jm\theta}] \\ & [A_Z e^{-jk_z z} + B_Z e^{jk_z z}]e^{j\omega t}. \end{aligned} \tag{4.20}$$

The periodicity of θ requires $\Theta(\theta = 0) = \Theta(\theta = 2\pi)$, then $\Theta(\theta) = A_\theta e^{-jm\theta} + B_\theta e^{jm\theta} = C_\theta\{\begin{matrix} cos(m\theta) \\ sin(m\theta) \end{matrix}\}$. It is noted that m must be integer, otherwise $cos(m\theta)$ and $sin\theta$ will not be single-valued. Since $N_m(k_r r \to 0) \to -\infty$ and ϕ has to be finite at $r = 0$, then $B_r = 0$. Therefore, $R(r) = A_r J_m(K_r r)$. At $r = a$, rigid wall demands $u_r = \frac{\partial\phi}{\partial r}|_{r=a} = 0$, i.e., $\frac{dR}{dr}|_{r=a} = 0$. So,

$$\frac{d}{r}(J_m(k_r r))|_{r=a} = k_r J'_m(k_r a) = 0. \tag{4.21}$$

The solution of Eq. (4.21) is

$$k_{rmn}a = \alpha_{mn}, \tag{4.22}$$

where m and n represent the diametral and radial mode numbers. α_{mn} can be available by looking up Table 4.1. Therefore, the total solution can be written in the form [67, 66]

$$\begin{aligned}\phi(r,\theta,z,t) = &\sum_{m=0}^{\infty}\sum_{n=0}^{\infty}\left\{\begin{array}{c}\cos(m\theta)\\ \sin(m\theta)\end{array}\right\} J_m(\alpha_{mn}\frac{r}{a}) \\ &(A_{zmn}e^{-jk_{zmn}z} + B_{zmn}e^{jk_{zmn}z})e^{j\omega t},\end{aligned} \tag{4.23}$$

where $k_{zmn}^2 = k^2 - (\frac{\alpha_{mn}}{a})^2$. k_{zmn} must be real-valued for wave propagation, otherwise, if k_{zmn} is imaginary, (m,n) mode waves are damped exponentially along the tube length. Therefore, only propagation of plane wave requires

$$k < \frac{\alpha_{10}}{a}. \tag{4.24}$$

Please note $\alpha_{10} = 1.841$ is the smallest value for all higher modes. Assuming $c_0 = 343$ m/s, substitution of $k = \frac{2\pi f_c}{c_0}$ into Eq. 4.24 gives

$$a < \frac{100.5}{f_c}, \tag{4.25}$$

where f_c is the cut-off frequency of the circular tube, which is the highest permitting characterization frequency. For instance, 1) for our relative frequency response test, the frequency range spans up to $f_c = 10$ kHz, then $a < 0.0101$ m, i.e, $a < 10.1$ mm; 2) our calibration tests at the frequencies less than 2 kHz requires $a < 50.3$ mm. In addition, far field wave excitation demands $kl >> 1$, where l is the tube length. If the microphone is calibrated at 1 kHz, plugging the numbers gives $l >> 0.0546$ m. For simplicity, tube length of 1 m is used for all acoustic tests.

4.4.2 Signal Conditioning Circuit

Figure 4.9 shows the schematic diagram of signal conditioning circuit of the PVDF crosshair microphone. It consists of a buffer circuit with two operational amplifiers

Table 4.1: The roots, α_{mn}, of the Bessel function $J'_m(\alpha_{mn})$=0 [67]

m	n=0	n=1	n=2	n=3	n=4
0	0	3.832	7.016	10.174	13.324
1	1.841	5.331	8.536	11.706	14.864
2	3.054	6.706	9.970	13.170	16.348
3	4.201	8.015	11.346	14.586	17.789
4	5.318	9.282	12.682	15.964	19.196

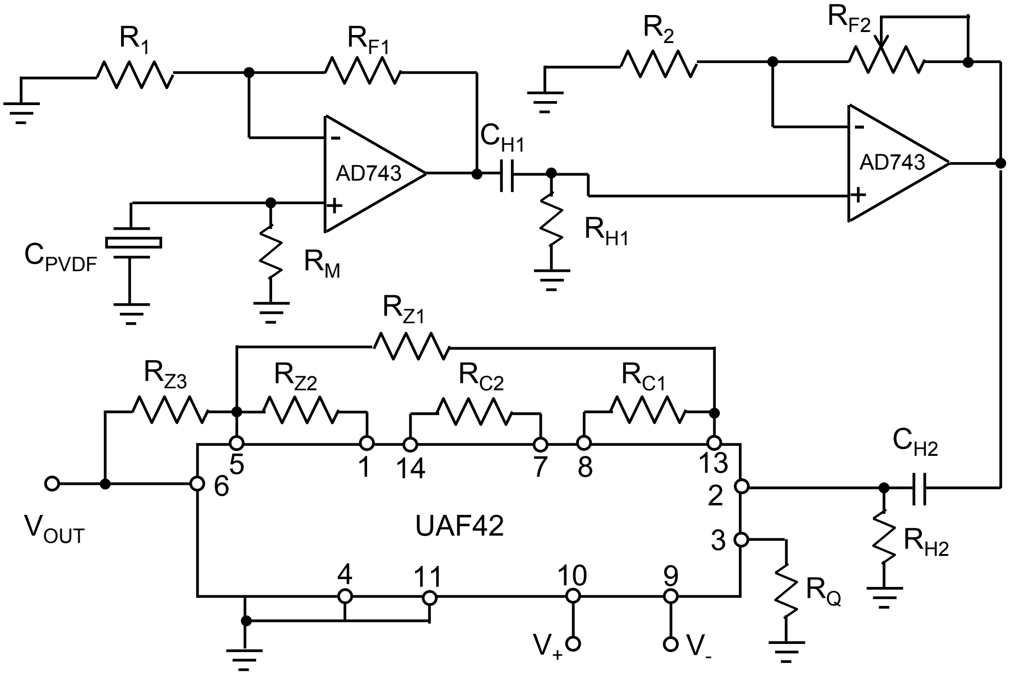

Figure 4.9: Schematic diagram of signal conditioning circuit.

in series, two high-pass RC filters and a 60 Hz noise notch filter. The preamplifier circuit is very important for the signal conditioning of the PVDF crosshair microphone. There are two types of integrated circuits generally used in piezoelectric sensors: charge and voltage amplifiers. For the charge amplifiers, the output voltage is equal to Q_o/C_f (where C_f is the capacitance of the feedback capacitor), which means that the output voltage is independent of the sensor capacitance. Using a small C_f can lead to a very large voltage output. However, it is impractical to use charge amplified systems above 50 kHz since the feedback capacitor exhibits filtering characteristics above this range. Therefore, the voltage amplifier is employed in our circuit design. A PVDF microphone behaves as a capacitor, hence it generates output voltages with a high impedance level. The source impedance combined with the load resistance provided by the amplifier generates a voltage divider. As the ratio of the load resistance to the source impedance decreases, the output voltage also decreases, which is known as the loading effect. This issue can be addressed by a buffer circuit using an operational amplifier such as the Analog Devices AD743. This amplifier has very high input resistance (300 GΩ) and small output resistance (around 10 Ω). The buffer circuit converts the high output impedance of the microphone into a low impedance signal which eliminates the loading effect and thus minimizes the signal loss. A first order high-pass filter after the output of each operational amplifier is also utilized to decouple DC voltage and low frequency components generated by thermal effects, which is useful to avoid the potential for signal drift and the saturation of the amplifier. Therefore, the first amplifier gain ($\mathrm{R_{F1}/R_1}$) should be relatively smaller compared to that of the second amplifier ($\mathrm{R_{F2}/R_2}$). The total gain of 1000 is used for the acoustic tests.

60 Hz powerline frequency noise is one of the most influential components of interference that contaminates acoustic signals induced in PVDF film based microphone. One effective solution to this problem is a 60 Hz notch filter. A notch filter can

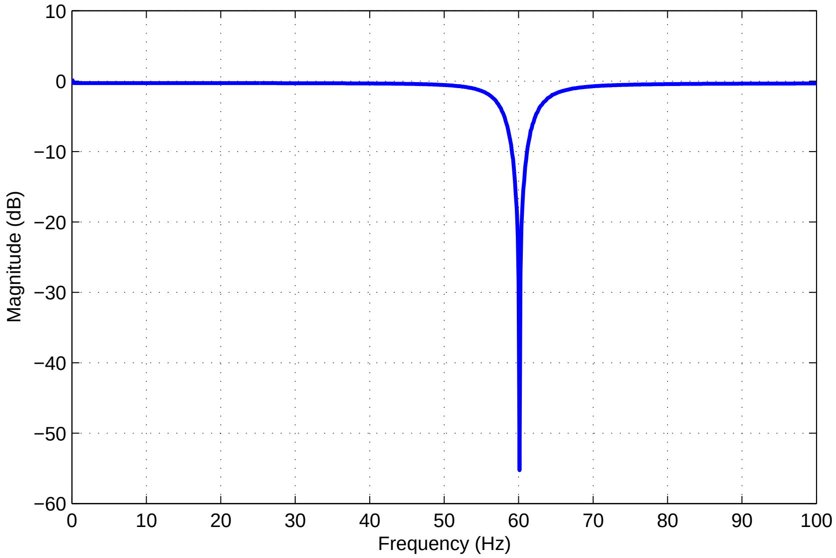

Figure 4.10: 60 Hz notch filter frequency response.

eliminate the 60 Hz noise while not deleteriously affect the integrity of the rest of the signal. The notch filter having the notch frequency of 60 Hz and Q factor of 10 is realized with the UAF42 chip and six external resistors (Figure 4.9). $\mathrm{R_{C1}} = \mathrm{R_{C2}}$ of 2.65 MΩ is given by $1/(2\pi f_o C)$, where f_o is the notch frequency of 60 Hz and C is the internal capacitance of 1 nF. $\mathrm{R_Q}$ of 2.78 kΩ is calculated by $25/(\mathrm{Q}-1)$. The Q factor should be adjusted by setting $\mathrm{Q} = \mathrm{R_{Z3}}/\mathrm{R_{Z1}} = \mathrm{R_{Z3}}/\mathrm{R_{Z2}}$, which guarantees the unit of the pass-band gain. Figure 4.10 shows the measured frequency response of the transfer function of the 60 Hz notch filter. Approximately 55 dB reduction at 60 Hz is obtained for the designed notch filter.

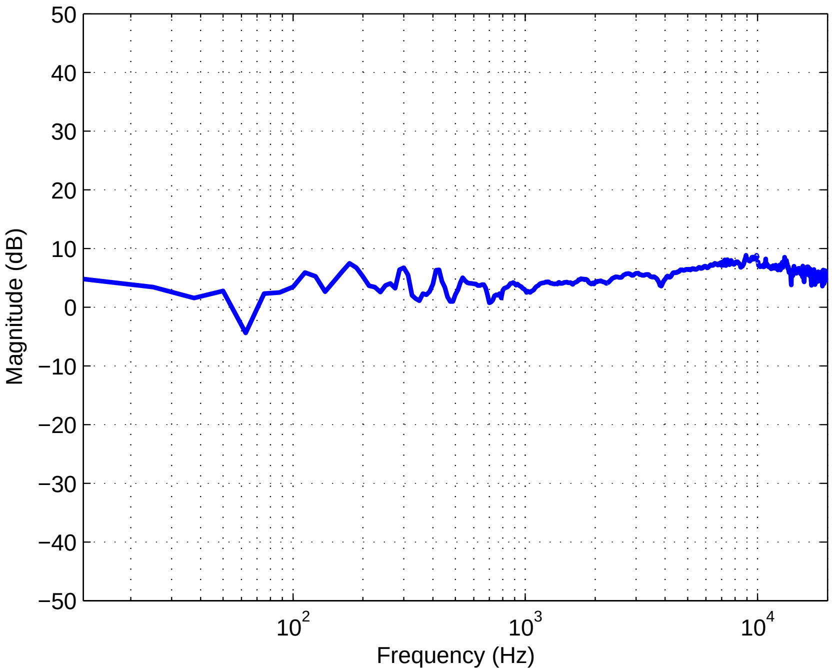

Figure 4.11: Relative sensitivity frequency response.

4.4.3 Experimental Results

The relative sensitivity frequency response (Figure 4.11, the crosshair PVDF microphone versus PCB 130C10) was measured using band-limited random noise of 94 dBA with a frequency range spanning up to 20 kHz. A tube with a diameter of 3/4" and a length of 1 meter was used. The data were obtained by averaging single-sided auto-power spectral density (PSD), G_{xx} and cross PSD, G_{xy}, estimates from 20 records of the measured signals. The spectrum, with a frequency resolution of 12.5 Hz, was computed using the Fast Fourier Transform (FFT) algorithm and Hanning window applied to the discrete time domain data. The response is nearly flat and has a fluctuation of about ±3 dB over the frequency range up to 20 kHz, except for the notch frequency of 60 Hz (actually 62.5 Hz shown in Figure 4.11 due to the frequency resolution).

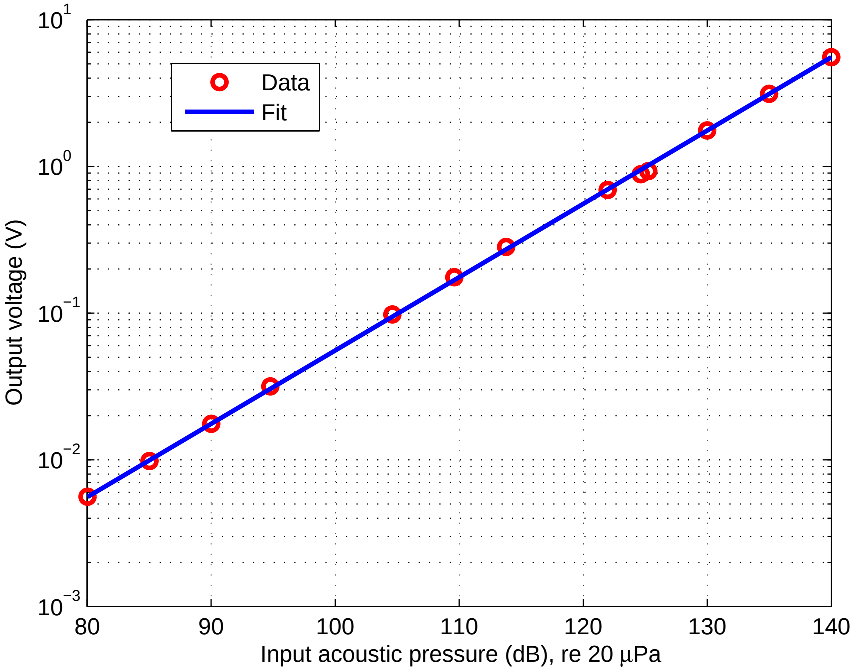

Figure 4.12: Measured microphone linearity at 1 kHz.

The measured linearity of the microphone at 1 kHz is shown in Figure 4.12. A tube with a diameter of 4" and a length of 1 meter was used. 1 kHz sinusoidal wave was generated by Quattro to drive the speaker to excite the crosshair PVDF microphone and the reference microphone. The linearity plot shows that the crosshair PVDF microphone exhibits an almost linear response (constant sensitivity) to sound pressure up to 140 dB. The maximum testable level is limited here by the output capacity of the speaker.

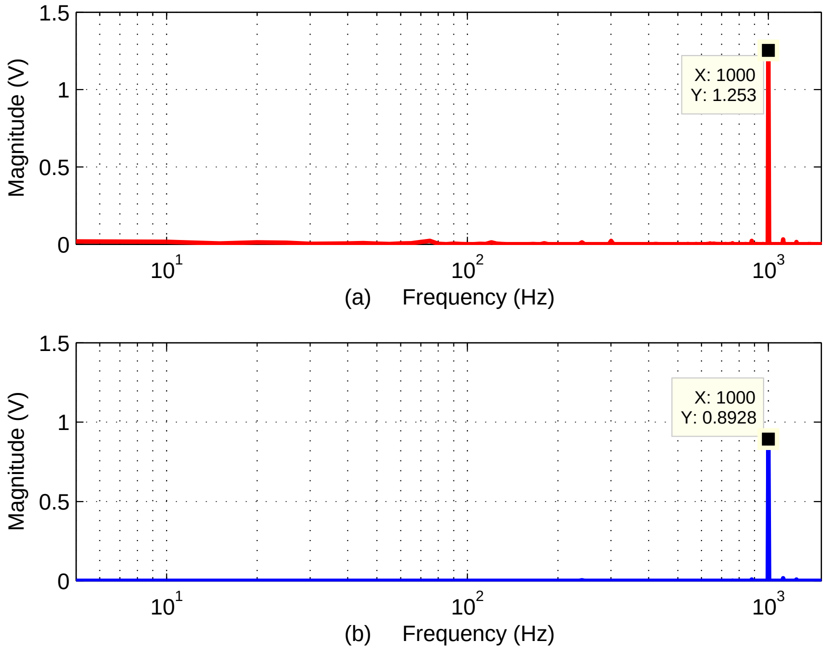

Figure 4.13: Comparison of voltage spectra of the two microphones at 1 kHz and SPL = 124 dB. (a) Voltage spectrum of the crosshair PVDF microphone. (b) Voltage spectrum of the reference microphone.

The sensitivity calibration tests of the microphone were conducted under 1 kHz sine wave at SPL of 124 dB. A tube with a diameter of 4” and a length of 1 meter was used to generate 1 kHz plane wave. The linear spectrum is obtained by using FFT and a uniform window. Figure 4.13 shows the spectra comparison between the two microphones for one test. Please note that for a sinusoidal wave with an amplitude of A, the double-sided linear spectrum will show a spike with magnitude of A, but the root mean square (RMS) value of the sinusoidal wave is $A/\sqrt{2}$. For the reference microphone having a sensitivity of 19.9 mV/Pa, in order to maintain SPL = 124 dB (i.e., RMS pressure of 31.6979 Pa), the RMS output voltage of the reference microphone is 0.6308 V and it should be shown at 0.8921 V (i.e., $\sqrt{2} \times 0.6308$ V) in the linear spectrum. Table 5.1 shows the recorded peak values of 1 kHz from the double-side spectra of ten test runs on the two microphones. According to this table, the sensitivity of the crosshair PVDF microphone is found to be 27.8±0.235 mV/Pa, or equivalently -15.563±0.0367 dB (re 1 V/Pa).

The sensitivity of a flat continuous PVDF film working under 3-3 mode is expressed by $K = -g_{33} \cdot h$, where g_{33} the piezoelectric stress constant in the x_3 direction (for the used MSI PVDF film, it is -330 mVm/N) and h is the thickness, with a value of 28 micron. Then the theoretical sensitivity of the MSI PVDF film is 9.24 μV/Pa. For the crosshair PVDF microphone, since the amplifier gain of 1000 is used, the sensitivity of the sensor itself (without including the amplifier) is 27.8 μV/Pa and therefore the sensitivity amplification ratio of 3.01 (27.8/9.24) is obtained. The obtained ratio of 3.01 is close to the area amplification ratio of 3.2, which verifies the principle of this design. The small difference might come from fabrication errors and signal loss due to the cable capacitance and the input capacitance of the amplifier.

Table 4.2: The peak values obtained from the linear spectra of the developed microphone and the reference microphone for ten test runs

n	1	2	3	4	5	6	7	8	9	10
V_C (V)	1.212	1.226	1.209	1.273	1.253	1.248	1.262	1.236	1.271	1.262
V_P (V)	0.872	0.866	0.875	0.902	0.893	0.894	0.901	0.892	0.912	0.914

The directivity of the microphone is measured using the experimental setup as shown in Figure 4.14. A speaker is placed in front of the microphone and the distance between the speaker and the microphone is also set to 1 m. The directivity result

(Figure 4.15) is obtained by changing the angle of the microphone using a rotary table (from -90 degree, i.e. 270 degree, to 90 degree). 1 kHz sinusoidal wave is also utilized as the excitation wave and the induced voltage at 0 degree is used as the reference. The result illustrates that a decay of about -10.5 dB at 90 degree or -90 degree is measured.

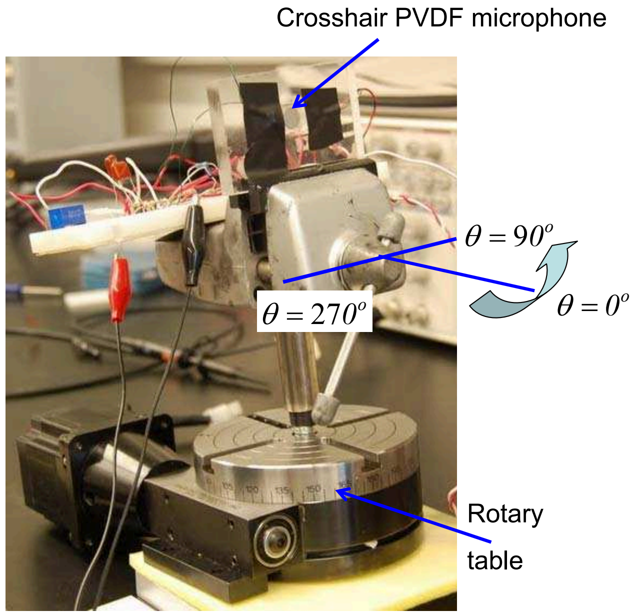

Figure 4.14: Experimental setup for characterizing the directivity.

4.5 Discussion

New acoustic sensors with high sensitivity, wide dynamic range and high frequency bandwidth are needed for addressing emerging requirements of many acoustic, aeroacoustic, and clinical applications. This chapter presents the design, sensitivity

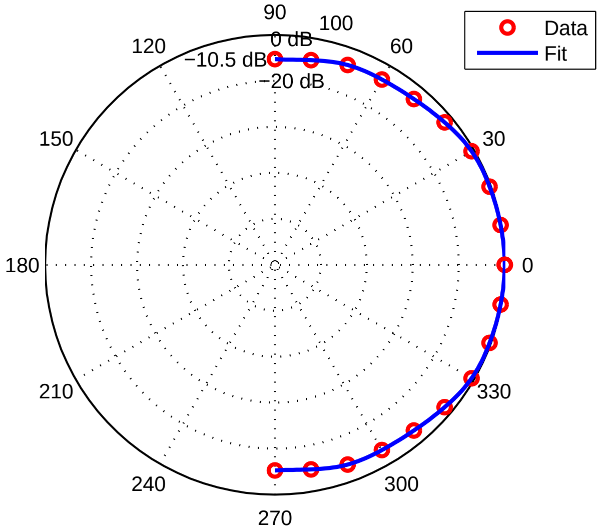

Figure 4.15: Directivity of the developed microphone.

analysis, finite element analysis, fabrication and characterization of a new type of millimeter-size PVDF acoustic sensor based on a crosshair pattern with an area ratio amplification principle, which can theoretically achieve 3.2× the sensitivity of existing commercial available PVDF film in combination with a dynamic range of 180 dB and a frequency bandwidth of approximately 100 kHz. Increased sensitivity is achieved through pressure amplification (created by the area ratio between the rigid surface exposed to acoustic waves and the crosshair pattern) in combination with reduced capacitance (created by a patterned top electrode.)

Various techniques such as CAD/CAM and FEM are employed for the development of design and fabrication of the microphone. Finite element simulations including static structure analysis, modal analysis and harmonic response are performed in ANSYS WORKBENCH to finalize and evaluate the microphone assembly with a requirement of a dynamic range up to 180 dB and a frequency bandwidth of 100 kHz. Three adjacent resonant frequencies including the fundamental natural frequency are found through modal analysis results. Peak coalescence is observed from the harmonic response of the device. The static and dynamic stress distributions make sure of the design within the safety constraint. Experimental setup is developed to characterize the microphone using a commercial available PCB microphone as reference. The theory and design of a circular plane wave tube is presented and signal conditioning circuits including the preamplifier circuit and the notch filter are also developed. Acoustic tests show that the microphone exhibits a good linearity up to 140 dB (SPL) and a relatively flat frequency response up to 10 kHz (The maximum testable level is limited by the output capacity of the speaker and the data acquisition system). The microphone has a sensitivity of 27.8 mV/Pa. Most importantly, the sensitivity of the sensor itself (without the amplifier) is found to be 27.8 μ/Pa that is 3.01 times the sensitivity of the commercial available PVDF film working in 3-3 mode, which is approximate to the area amplification ratio of 3.2.

One goal of this chapter is to develop a proof-of-concept PVDF sensor based on stress amplification and patterned electrodes. The small size, high stiffness, and reduced mass of MEMS sensors are of great interest because such devices can significantly improve both the temporal and spatial measurement bandwidth [51]. One superior advantage of MEMS sensors can achieve a relative higher area ratio (100× is possible) compared to the traditional fabrication processes. Optimal MEMS sensors based on PVDF micro-pillars and patterned electrodes with various area amplification ratios (up to$\sim$ 60) will be discussed in Chapter 5.

CHAPTER 5

VALIDATION AND CHARACTERIZATION OF AN ACOUSTIC SENSOR BASED ON PVDF MICRO-PILLARS AND PATTERNED ELECTRODES

This chapter presents the fabrication, validation, and characterization of a new type of millimeter-size acoustic sensor that uses Polyvinylidene Fluoride (PVDF) micro-pillars and patterned electrodes. The sensor takes advantage of two key design principles: 1) stress amplification mechanism through the area ratio between the overall surface exposed to acoustic waves and the area of the individual micro-pillars; 2) patterned electrodes created to reduce the capacitance of the sensor by excluding the capacitance of the air between micro-pillars. In combination, these design principles enable a sensor which in practice could achieve 100x the sensitivity of flat PVDF film.

An analytical sensitivity analysis is presented and sensor fabrication details are described. An experimental setup is developed to characterize the sensor against a commercially available PCB microphone. The theory and design of a circular plane wave tube is presented and the signal conditioning circuit including the preamplifier circuit and notch filter is discussed. Sensitivity calibration tests show that the developed sensor with a gap ratio of 5.8182 exhibits a stress constant of -19.93 V/m/Pa in 33 mode, which is 60.39× bigger than that of commercial available PVDF film.

Experimental results also show that the sensitivity of the sensor is in close agreement with theory, thus confirming the performance advantages of the micro-pillar sensor.

5.1 Sensitivity Analysis

In chapter 3, we proposed two designs: PVDF micro-pillars with patterned electrodes (Figure 3.1) and with full electrodes. The sensitivities of three PVDF sensor designs are compared: flat continuous film, PVDF micro-pillars with full electrodes, and PVDF micro-pillars with patterned electrodes.

Compared to the flat continuous PVDF film, the sensitivity amplification ratios of PVDF micro-pillars with patterned electrodes and with full electrodes are $(d+g_1)\cdot(d+g_2)/(\pi d^2/4)$ and $\varepsilon_r(d+g_1)(d+g_2)/[\pi d^2/4\cdot(\varepsilon_r-1)+(d+g_1)(d+g_2)]$, respectively. In other words, PVDF micro-pillars with patterned electrodes has a new stress constant of $(d+g_1)\cdot(d+g_2)/(\pi d^2/4)\cdot g_{33}$ and with full electrodes desgin it has a new stress constant of $\varepsilon_r(d+g_1)(d+g_2)/[\pi d^2/4\cdot(\varepsilon_r-1)+(d+g_1)(d+g_2)]\cdot g_{33}$. A comparison of the sensitivities of the two micro-pillar designs relative to that of solid PVDF film is shown in Figure 3.4. The micro-pillar sensor with patterned electrodes theoretically has an unlimited sensitivity with increasing geometry ratio g/d (assuming $g = g_1 = g_2$). It is possible that an PVDF sensor based on micro-pillars and patterned electrodes with a gap ratio of ~ 8 could achieve 100× the sensitivity of flat PVDF film. For the developed PVDF micro-pillar sensor with patterned electrodes (details described in Section 5.2), the gap ratio (g/d) of the sensor is 5.8182. Therefore, the stress constant of the fabricated sensor is theoretically 59.19× larger than that of flat continuous PVDF film (Figure 3.4).

5.2 Sensor Fabrication

5.2.1 Patterned Electrode Fabrication

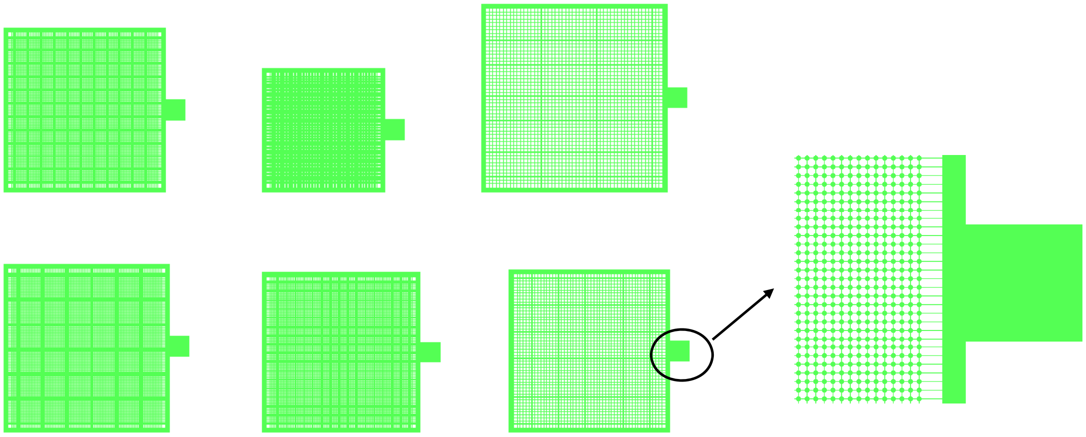

Figure 5.1: Photomask designed in ADS.

Figure 5.1 shows the photomask used for the patterned electrode fabrication. The mask contains six designs, and one (left and bottom) was, with the biggest gap ratio, chosen for the fabricated sensor. The negative of the electrode pattern, which consisted of 11 μm diameter circles (~64 μm spacing) interconnected by 2 μm wide lines, was first defined on a glass slide via photolithography using a positive photoresist (Shipley 1813). A ~50 nm Au/Pd layer was then sputter-coated on the patterned surface, followed by acetone-assisted dissolution of the photoresist in a sonicator. The fabrication process and optical micrographs of the electrode are depicted in Figure 5.2.

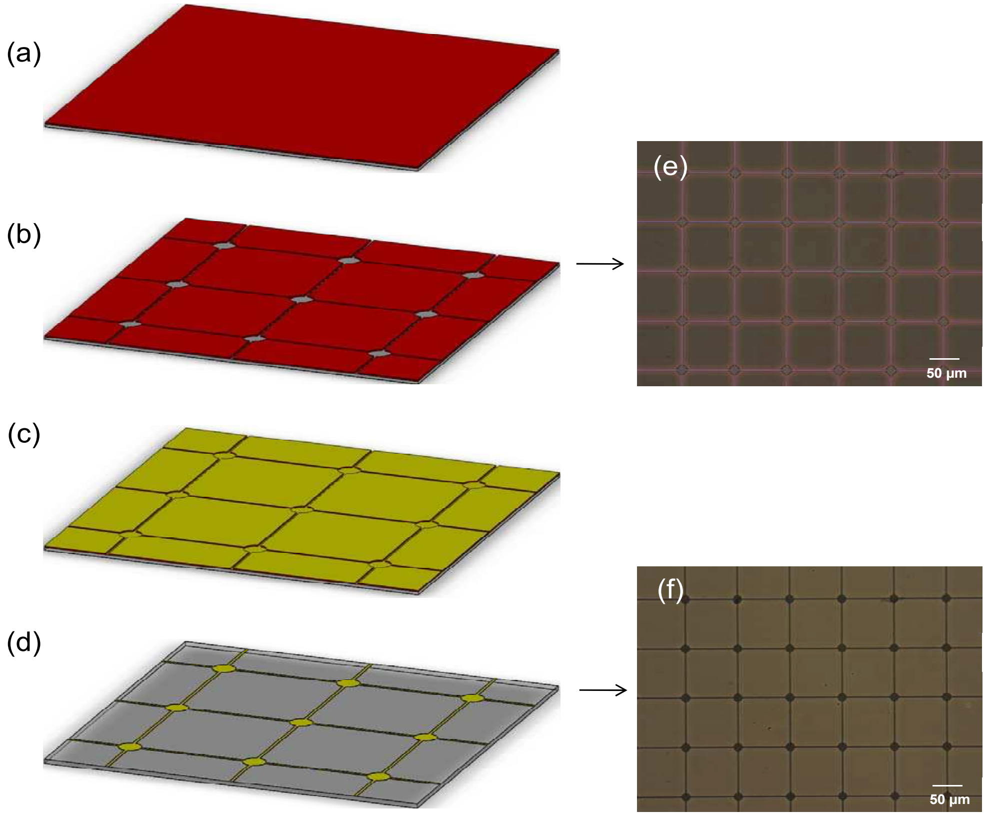

Figure 5.2: Patterned electrode fabrication. (a) Photoresist is deposited over the glass slide. (b) Photoresist patterning via photolithography. (c) Au/Pd layer is deposited over the patterned surface. (d) Photoresist is selectively removed with acetone. (e) and (f) Optical micrographs of the patterned photoresist and patterned electrode, respectively.

5.2.2 PVDF Microfabrication

PVDF micropatterning and poling was conducted via previously established techniques, described in more detail elsewhere. Standard photolithography was used to define the footprint pattern of the sensor (11 μm diameter circles spaced by 64 μm) on a silicon master. A polydimethylsiloxane (PDMS) stamp bearing the negative replica of the pattern was created by pouring silastic T-2 PDMS (Dow Corning) mixed with its curing agent over the master, vacuum degassing and curing at room temperature for 48 hours before removal. Patterned PDMS stamps were then used for the fabrication of PVDF micropillars. Briefly, a 10 wt % PVDF (Aldrich) solution in dimethylacetamide (Sigma-Aldrich) and acetone was spin coated on the PDMS stamp at 1000 rpm for 45 seconds. The stamp was then heated up to $\sim$150°C for 2-3 minutes to evaporate the solvent and anneal the PVDF. The micropatterned PVDF film was optically aligned with the patterned electrode, and bonded together via thermal pressing at $\sim$150°C and 35 kPa for 5 minutes. Figure 5.3 illustrates the fabrication process of PVDF micropillars. Scanning electron microscopy (SEM) images of the patterned PVDF films are shown in Figure 5.3 (e) and (f). Cross sectional analysis via SEM confirmed that the patterned film had a thickness of 9.5 $\pm$0.67 μm (average $\pm$standard deviation). Finally, the PVDF pillars were overlaid with adhesive copper tape (3M), and poled by applying an electric field of $\sim$120 MV/m.

5.3 Experimental Validation and Characterization

5.3.1 Experimental Setup

The experimental setup shown in Figure 4.7 is developed to conduct various acoustic tests including sensitivity calibration and validation, sensitivity frequency response, and sensor linearity. To calibrate the dynamic response of the sensor, a speaker, driven by the sinusoidal wave or band-limit white signal generated from Quattro, is attached to one end of a circular plane wave tube (PWT). A commercially available microphone, PCB 130C10, is used to characterize the developed sensor. The

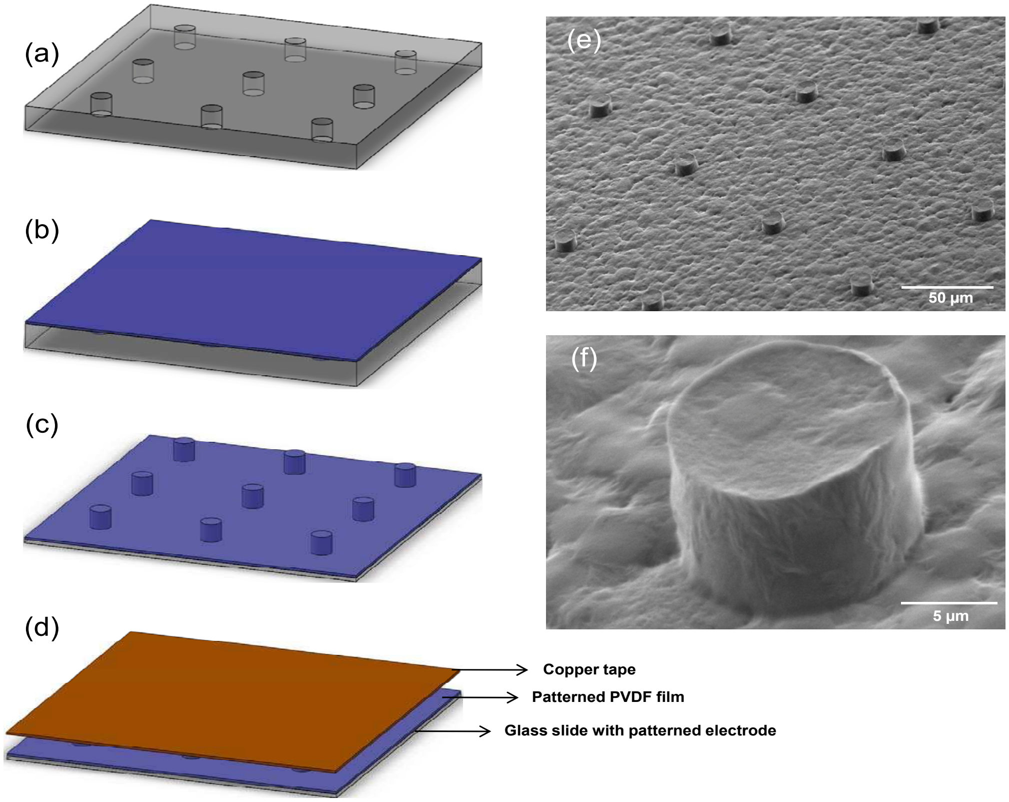

Figure 5.3: PVDF patterning and sensor assembly. (a) Patterned PDMS mold. (b) PVDF solution is spin coated over the PDMS. (c) Patterned PVDF film is aligned and transferred onto the patterned electrode. (d) Copper tape is overlaid on top of the pillars. (e) and (f) show lower and higher magnification SEM micrographs of the PVDF pillars, respectively.

micro-pillars microphone is placed at the opposite end of the PWT next to the commercial microphone. A PWT is also designed as discussed before, and used to only propagate the fundamental mode (0,0) plane wave and make sure that the higher order modes are evanescent for various acoustic tests. The signals induced from the micro-pillar sensor is processed by the signal conditioning circuit and fed into the data acquisition system (Quattro+SignalCalc) while the signals from the commercial microphone are also recorded and analyzed by the data acquisition system with the interface of ICP coupling.

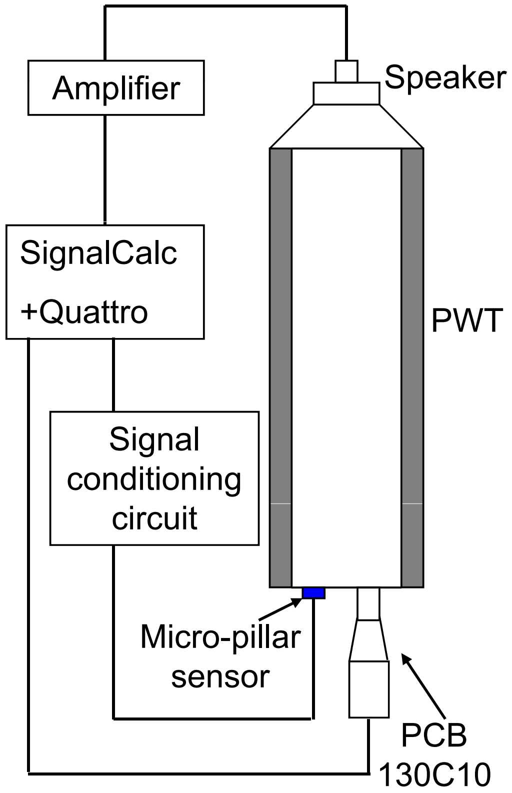

Figure 5.4: Schematic of experimental setup.

5.3.2 Signal Conditioning Circuit

Figure 5.5 shows the schematic diagram of signal conditioning circuit of the PVDF crosshair microphone. It consists of a buffer circuit with two operational amplifiers in series, two high-pass RC filters and a 60 Hz noise notch filter. The preamplifier circuit is very important for the signal conditioning of the micro-pillar sensor. A PVDF

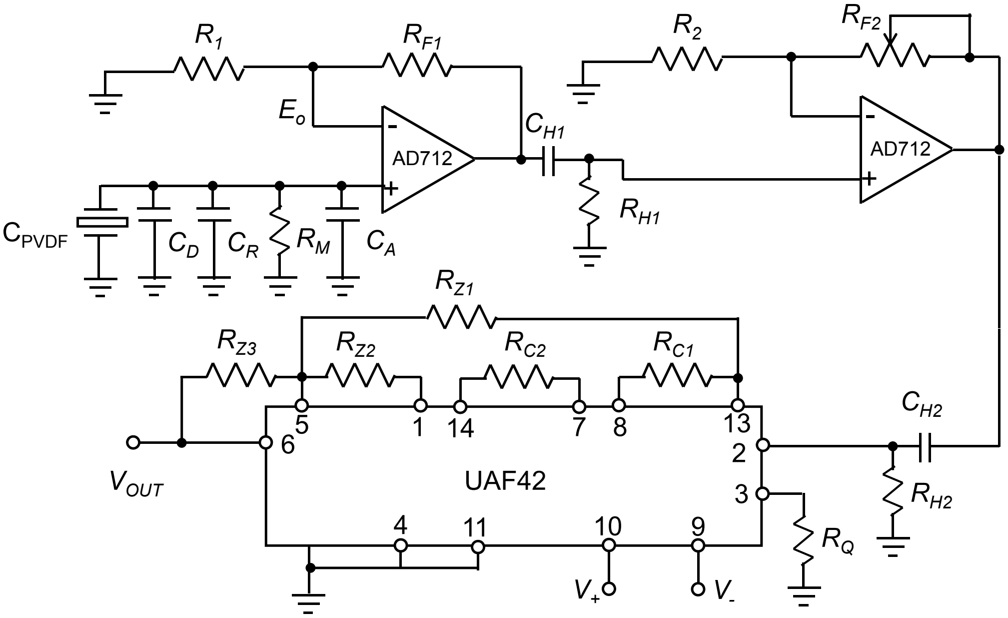

Figure 5.5: Schematic diagram of signal conditioning circuit.

microphone behaves as a capacitor, hence it generates output voltages with a high impedance level. The source impedance combined with the load resistance provided by the amplifier generates a voltage divider. As the ratio of the load resistance to the source impedance decreases, the output voltage also decreases, which is known as the loading effect. This issue can be addressed by a buffer circuit using an operational amplifier such as the Analog Devices AD712. This amplifier has very high input resistance (300 GΩ), small capacitance (5.5 PF) , and small output resistance (around 10 Ω). The buffer circuit converts the high output impedance of the microphone into a low impedance signal which eliminates the loading effect and thus minimizes the signal loss. A first order high-pass filter after the output of each operational amplifier is also utilized to decouple DC voltage and low frequency components generated by thermal effects, which is useful to avoid the potential for signal drift and the saturation of the amplifier. Therefore, the first amplifier gain (R_{F1}/R_1) should be relatively smaller compared to that of the second amplifier (R_{F2}/R_2). The total gain of 1000 is used for the acoustic tests. A notch filter can eliminate the 60 Hz noise while not deleteriously affect the integrity of the rest of the signal. The notch filter having the notch frequency of 60 Hz and Q factor of 10 is realized with the UAF42 chip and six external resistors, which has been discussed in chapter 4. Approximately 55 dB reduction at 60 Hz is measured for the designed notch filter.

For many PVDF film based applications, the capacitance of the PVDF film (typically around a few nanofarads) is much larger than the input capacitance of the amplifiers (typically about a few picofarads), which is therefore negligible. However, in terms of the acoustic sensor based on micro-pillars and patterned electrodes, its capacitance (C_{PVDF}, 9.5 pF) has the same order of magnitude compared to the input capacitance of the operational amplifier (C_A, 5.5 pF) and thus it must be taken into account in the sensitivity calibrations of the sensor. Similarly, the same treatment will be taken for the capacitance (C_R, 3.4 pF) of the parallel resistance, R_M. An additional parallel capacitance, C_D, is critical to the stability of the signal conditioning circuit. If this capacitance is too small, the output of the signal conditioning circuit will be bounded by the dual power supply (±10 V). A capacitor with capacitance of 104.4 pF is utilized for the circuit.

5.3.3 Sensitivity Calibration and Validation

PVDF micro-pillar sensor with the signal conditioning circuit can be modeled as a system comprising a second-order mechanical system, a first-order electrical system, two operational amplifiers in series, two high-pass RC filters, and a 60 Hz noise notch filter. The system transfer function (the sensitivity of the microphone with the signal conditioning circuit) is expressed by

$$K_{mic} = \frac{V_{out}(s)}{P(s)} = \frac{V_{out}(s)}{E_o(s)} \frac{E_o(s)}{P(s)}. \tag{5.1}$$

The system transfer function between $V_{out}(s)$ and $E_o(s)$ is expressed by

$$\frac{V_{out}(s)}{E_o(s)} = \frac{R_{F1}}{R_1} \frac{R_{H1}C_{H1}s}{R_{H1}C_{H1}s+1} \frac{R_{F2}}{R_2} \frac{R_{H2}C_{H2}s}{R_{H2}C_{H2}s+1} H_{nth}(s), \tag{5.2}$$

in which $H_{nth}(s)$ is the transfer function of the notch filter. The system transfer function between $E_o(s)$ and $P(s)$ is expressed by [83]

$$\frac{E_o(s)}{P(s)} = \frac{G_1 \tau s}{\tau s + 1} \left[G_2 S / \left(\frac{1}{\omega_n^2} s^2 + \frac{2\xi}{\omega_n} s + 1 \right) \right], \tag{5.3}$$

in which τ is the time constant of the first order system, ω_n is the natural frequency of the second order system, ξ is damping ratio, S is the area of the footprint of the sensor, and G_1 and G_2 are the gains of the first-order system and second-order system, respectively. Here, $G_1 = K_q/C_t$, where K_q is constant (C/m) and $C_t = C_{PVDF} + C_D + C_R + C_A$ is the total capacitance. $G_2 = 1/k$, where k is the equivalent stiffness of the mechanical system. Therefore,

$$\begin{aligned} \frac{E_o(s)}{P(s)} &= \frac{K_q}{C_t} \frac{\tau s}{\tau s + 1} \left[(S/k) / \left(\frac{1}{\omega_n^2} s^2 + \frac{2\xi}{\omega_n} s + 1 \right) \right] \\ &= \frac{C_{PVDF}}{C_t} \frac{K_q S}{C_{PVDF} k} \frac{\tau s}{\tau s + 1} \left[1 / \left(\frac{1}{\omega_n^2} s^2 + \frac{2\xi}{\omega_n} s + 1 \right) \right], \end{aligned} \tag{5.4}$$

in which $\frac{K_q S}{C_{PVDF} k}$ is defined as the static sensitivity of the sensor based on PVDF micropillars and patterned electrodes. In order to avoid the confusion of this sensitivity with the sensitivity of Eq. (4.13), we called it as the measured sensitivity

$$K_{mpm} = \frac{K_q S}{C_{PVDF} k}. \tag{5.5}$$

Because the cut-off frequency of the first order system and the high pass filters is chosen at 20 Hz and the natural frequency of the sensor is much greater than 100 kHz, at 1 kHz the magnitudes of $\frac{R_{H1}C_{H1}s}{R_{H1}C_{H1}s+1}$, $\frac{R_{H2}C_{H2}s}{R_{H2}C_{H2}s+1}$, $H_{nth}(s)$, $\frac{\tau s}{\tau s+1}$, and $1/\left(\frac{1}{\omega_n^2}s^2+\frac{2\xi}{\omega_n}s+1\right)$ are nearly 1. Further, $\frac{R_{F1}}{R_1}\frac{R_{F2}}{R_2}$ is adjusted to be 1000. Substitution of these values and Eq. (5.5) into Eqs. (5.2), (5.4), and (5.1) gives

$$K_{mic} = 1000\frac{C_{PVDF}}{C_t}K_{mpm}. \tag{5.6}$$

Or, the measured sensitivity of the sensor itself is

$$\begin{aligned} K_{mpm} &= K_{mic}\frac{C_t}{C_{PVDF}}\frac{1}{1000} \\ &= K_{mic}\frac{C_{PVDF}+C_D+C_R+C_A}{C_{PVDF}}\frac{1}{1000}. \end{aligned} \tag{5.7}$$

It is noted that for most PVDF film based applications the capacitance of PVDF film is typically much greater than the other capacitances such as the input capacitance of amplifier and also there is no need to employ a parallel capacitance to maintain the stability of the signal conditioning circuit. Under this circumstance, the total capacitance is almost equal to the capacitance of the PVDF film and thus the sensitivity of the sensor itself can be simply obtained by only considering the total gain of the signal conditioning circuit. Due to the small capacitance of PVDF micro-pillars with patterned electrodes comparable to the other capacitances, the measured sensitivity of the sensor should be calculated by the Eq. (5.7) including the capacitance ratio.

The sensitivity calibration tests of the microphone were conducted under 1 kHz sine wave at SPL of ∼120 dB. A PVC pipe with a diameter of 3” and a length of 1 meter was used to generate 1 kHz plane wave. The linear spectrum is obtained by using FFT and a Hanning window. Figure 5.6 shows the spectra comparison between

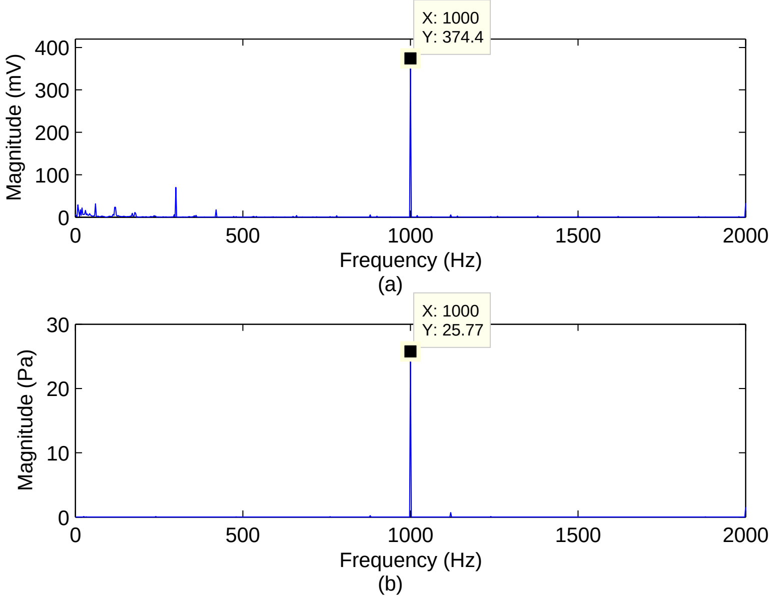

Figure 5.6: Comparison of voltage spectra of the two microphones at 1 kHz and SPL = 124 dB. (a) Voltage spectrum of the micro-pillar microphone. (b) Voltage spectrum of the reference microphone.

the two microphones for one test. Figure 5.7 shows the spectrum waterfall of ten test runs on the two microphones. Table 5.1 shows the recorded peak values of 1 kHz from the double-side spectra of ten test runs . Please note that for a sinusoidal wave with an amplitude of A, the double-sided linear spectrum will show a spike with magnitude of A, but the root mean square (RMS) value of the sinusoidal wave is $A/\sqrt{2}$. For the reference microphone having a sensitivity of 19.9 mV/Pa, the mean value of the pressure spikes of ten test runs is 26.49 Pa and thus the RMS pressure is $26.49/\sqrt{2} = 18.73$ Pa, i.e., 119.4 dB. According to this table, the sensitivity of the micro-pillar microphone (K_{mic}) is found to be 14.647±0.138 mV/Pa, or equivalently -18.343±0.041 dB (re 1 V/Pa). The measured sensitivity of the developed sensor

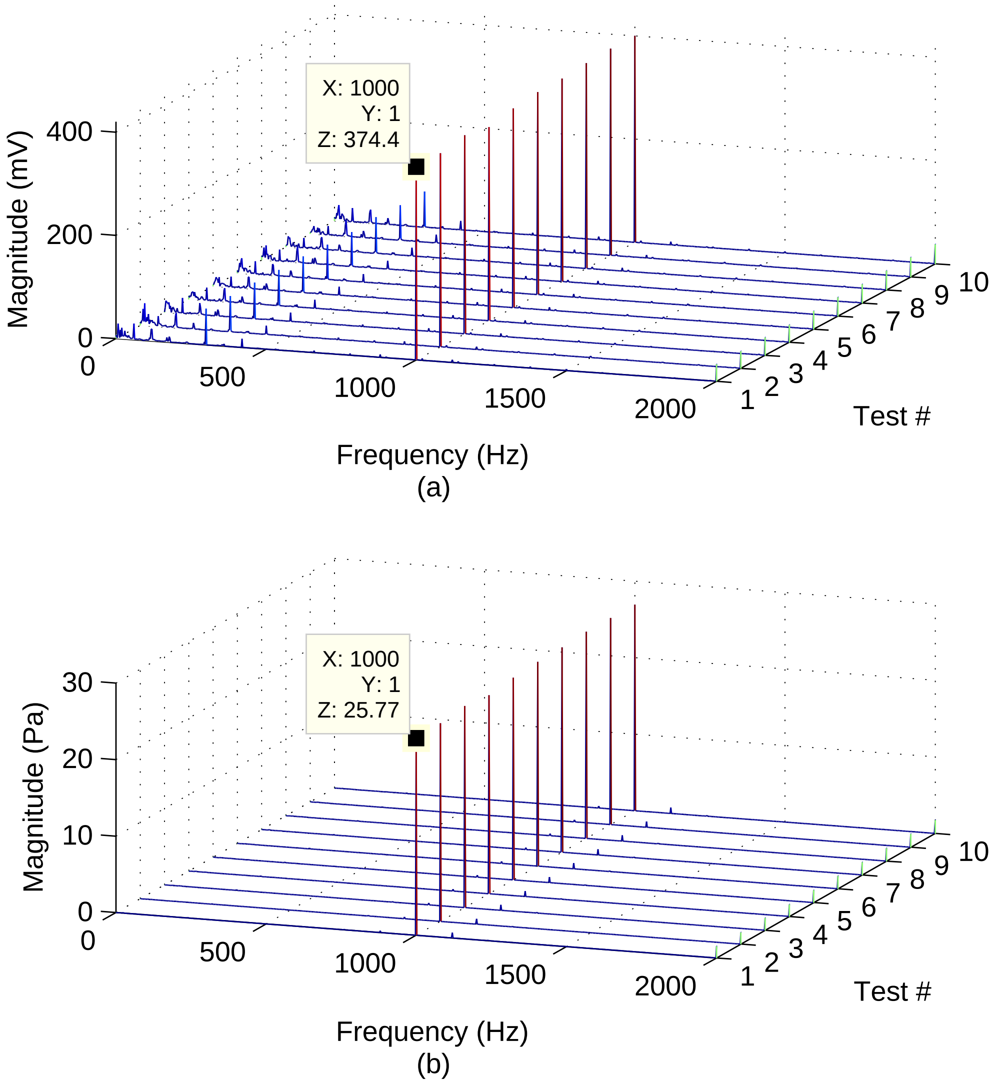

Figure 5.7: Spectrum waterfall of the two microphones at 1 kHz and SPL = ~120 dB. (a) Spectrum waterfall of the PVDF microphone. (b) Spectrum waterfall of the reference microphone.

(K_{mpm}) is 189.3±1.8 μV/Pa, calculated by $K_{mic}\frac{9.5+104.4+3.4+5.5}{9.5}\frac{1}{1000}$, or equivalently -37.228±0.041 dB (re 1 V/Pa).

Table 5.1: The peak values obtained from the spectrum waterfall of the developed microphone and the reference microphone

n	1	2	3	4	5	6	7	8	9	10
V_{OUT}(mV)	374.4	375.1	384.6	375.3	386.3	392.6	393.4	398.1	400.6	400.0
P_{PCB} (Pa)	25.77	25.92	26.34	25.96	26.43	26.71	26.79	27.03	26.99	26.95

Substitution of K_{mpm} and the thickness of PVDF micro-pillars, 9.5 μm, into Eq. (4.3) gives the measured piezoelectric stress constant in the x_3 direction is -19.93 V/m/Pa. While the stress constant of commercially available PVDF film (Measurement Specialties, Inc., USA), g_{33}, is -0.33 V/m/Pa. Therefore, the obtained stress constant amplification ratio is 60.39 (19.93/0.33). The obtained amplification ratio of 60.39 is close to the theoretical prediction of 59.19, thus confirming the performance advantages of the micro-pillar sensor. The small difference might come from the mask design, the fabrication errors, the measurements, and the poling process.

5.3.4 Sensitivity Frequency Response

In order to measure the sensitivity frequency response of the micro-pillar sensor, first the relative sensitivity frequency response $H_{x,y}(s)$ between the developed microphone and the reference microphone, PCB 130C10, is measured. So,

$$\begin{aligned}|H_{x,y}(s)| &= 20log(\frac{|V_{OUT}(s)|}{|V_{PCB}(s)|}) \\ &= 20log(\frac{|V_{OUT}(s)/P(s)|}{|V_{PCB}(s)/P(s)|}) \\ &= 20log(\frac{|K_{mic}(s)|}{|K_{PCB}(s)|}) \\ &= 20log(1000\frac{C_{PVDF}}{C_t}\frac{|K_{mpm}(s)|}{|K_{PCB}(s)|}),\end{aligned} \tag{5.8}$$

where, $|K_{PCB}(s)|$ is the sensitivity of the PCB microphone. Therefore,

$$|K_{mpm}(s)| = |K_{mic}(s)| \frac{C_t}{1000 C_{PVDF}} 10^{|H_{x,y}(s)|}. \tag{5.9}$$

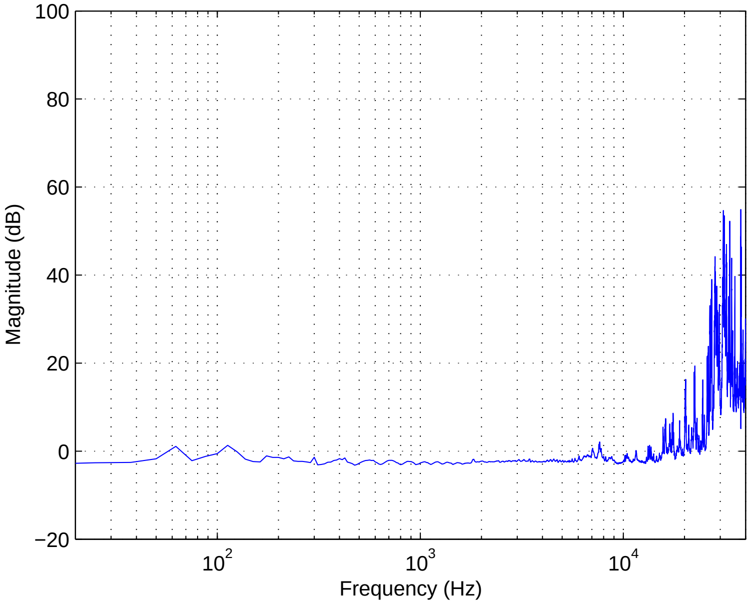

Figure 5.8: Relative sensitivity frequency response.

The relative sensitivity frequency response (Figure 5.8, the micro-pillar microphone versus PCB 130C10) was measured using band-limited random noise with a frequency range spanning up to 40 kHz. A tube with a diameter of 3/4" and a length of 1 meter was used. The data were obtained by averaging single-sided auto-power spectral density (PSD), G_{xx} and cross PSD, G_{xy}, estimates from 50 records of the measured signals. The spectrum, with a frequency resolution of 12.5 Hz, was computed using the Fast Fourier Transform (FFT) algorithm and Hanning window applied to the discrete time domain data. The sensitivity frequency response of the

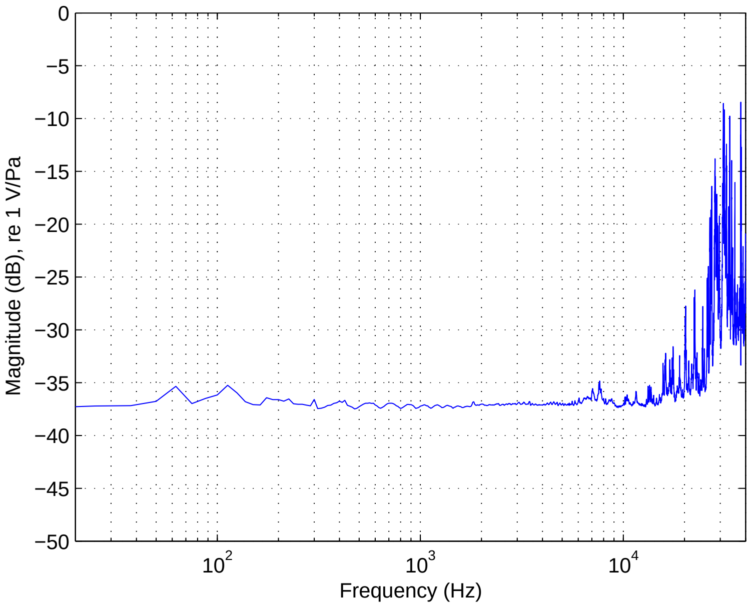

Figure 5.9: Sensitivity frequency response of the developed micropillar sensor.

developed micropillar sensor (Figure 5.9) is obtained using Eq. (5.9). The response is nearly flat and has a fluctuation of about ±2 dB over the frequency range up to 15 kHz. While the frequency response of 15-40 kHz can not be fully determined because the PCB 130C10 (PCB Piezotronics, Inc.) has a frequency bandwidth of 10-15000 Hz and the frequency response beyond 15 kHz in the calibrated sheet is truncated. Most likely, the commercial microphone has a low pass filter with a cut-off frequency of ∼15 kHz and our micro-pillar sensor still has a relatively flat frequency response beyond 15 kHz, the pseudo increasing trend in the frequency response after 15 kHz could be due to the decreasing trend in the frequency response of the commercial microphone, PCB 130C10.

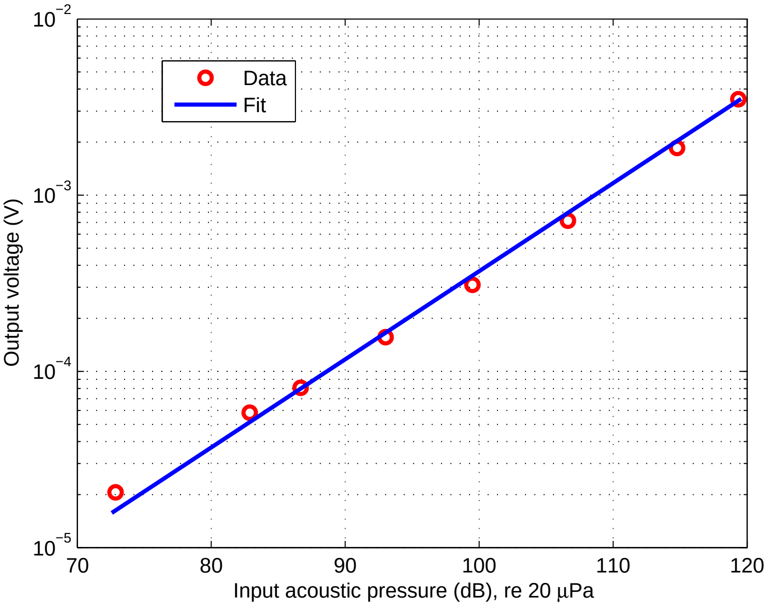

Figure 5.10: Measured sensor linearity at 1 kHz.

5.3.5 Sensor Linearity

The linearity of a sensor is an expression of the extent to which the actual measurements of the sensor departs from the ideal curve. The measured linearity of the sensor at 1 kHz is shown in Figure 5.10. A 1 kHz sinusoidal wave was generated by Quattro to drive the speaker to excite the micro-pillar microphone and the reference microphone. A PVC pipe with a diameter of 3” and a length of 1 meter was used. The linearity plot shows that the micro-pillar sensor exhibits an almost linear response (constant sensitivity) to sound pressure up to 120 dB. The maximum testable level is limited here by the output capacity of the speaker.

5.4 Concluding Remarks

New acoustic sensors with high sensitivity and high frequency bandwidth are needed for addressing emerging requirements of many acoustic, aeroacoustic, and clinical applications. This chapter presents the design, fabrication, sensitivity analysis, validation, and characterization of a new type of millimeter-size PVDF acoustic sensor based on micro-pillar array and patterned electrodes, which can theoretically achieve 59.19x the sensitivity of existing commercially available PVDF film. Increased sensitivity is achieved through pressure amplification (created by the area ratio between the rigid surface exposed to acoustic waves and the micro-pillars array) in combination with reduced capacitance (created by a patterned top electrode.)

Detailed fabrications of patterned electrode and sensor assembly are described. An experimental setup is developed to characterize the microphone using a commercially available PCB microphone as reference. Signal conditioning circuits including the preamplifier circuit and the notch filter are also developed. Acoustic tests show that the microphone exhibits a good linearity up to 120 dB (SPL) and a relatively flat frequency response up to 15 kHz. The testing was limited by the PCB microphone used for characterization. The sensor should be theoretically capable of a frequency range greater than 100 kHz considering that the sensor works in the thickness mode **??**. The sensitivity calibration test shows that the developed sensor has a sensitivity of 189.3 μV/Pa, which is 60.39× greater than that of the commercial solid PVDF with the same footprint area and the thickness. More specifically, the measured stress constant of the sensor is -19.93 V/m/Pa, which is 60.39× bigger than that of commercial solid PVDF (g_{33} =-0.33 V/m/Pa). Meanwhile the measured stress constant amplification ratio is in good agreement with the predicted amplification ratio.

CHAPTER 6

DEVELOPMENT OF MICRO-TENSILE TESTER AND CHARACTERIZATION OF NANOFIBERS

6.1 Preamble

Nanofibers with their large surface-to-volume ratio have found numerous applications in many different areas including energy storage, healthcare, biotechnology, environmental engineering, and defense and security [62]. With the increased popularity in academic research, potential applications of electrospun fibers have also been identified such as high-performance air filters, protective textiles, solar cells and full cells, polymer batteries, sensors, advanced composites, photovoltaic cells, and scaffolds in tissue engineering [27, 65, 78, 20, 85].

Studies show that the stiffness of the scaffold plays an important role in various cellular functions at the micro level such as cell growth, differentiation and motility [68]. For next generation of flexible sensors, it is indispensable to characterize the morphological, mechanical, electrical, and electromechanical properties of electrospun flexible structures using micron to macroscale techniques. Therefore, there is a great need to study the nanomechanical properties of individual nanofibers. Tensile testing of specimens with a size of a few millimetres or larger can be conducted using conventional universal testing machines. However, for micro- and nanoscale fibers, this kind of equipment is not suitable and some alternative means need to be explored and studied. In order to characterize nanofibers, it requires a tensile tester capable of detecting micro-Newtons range force or even smaller depending on the method chosen by the user. Further, due to the small size of nanofibers, the manipulation of the fibers is quite a challenge compared to the conventional holder used in the commercially available MTS machines.

Viscoelasticity is the property of materials that exhibit both viscous and elastic characteristics when subjected to deformation. Viscous materials, like honey, resist shear flow and strain linearly with time when a stress is applied. While elastic materials, such as steel, produce strain instantaneously when stretched and can return to their original state immediately after the stress is removed. Generally speaking, polymers are viscoelastic materials and they exhibit elasticity in glassy state whereas they exhibit viscoelasticity in rubbery state.

6.2 Electrospinning Process

Electrospinning was first patented in the US in 1902 by Morton [53]. The process was, however, gaining in increasing popularity in the 1990s. With interest in the field of nanoscience and nanotechnology, more and more researchers began new study and investigations of nanofiber production using electrospinning process. Startups such as eSpin Technologies, NanoTechnics, and KATO Tech are just some of the companies

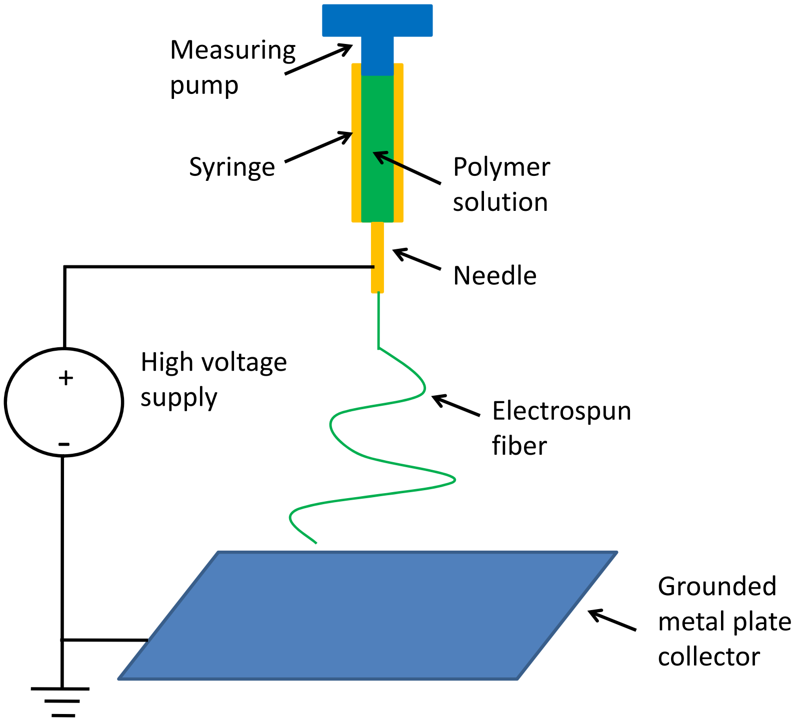

Figure 6.1: Schematic of elctrospinning process.

looking for the unique advantages offered by electrospinning process, while companies such as Donaldson Company and Freudenberg have been successfully employing electrospun fibers in their air filtration products for the last two decades [62].

Figure 6.1 shows the basic principle of elctrospinning process. Electrospinning is a process that produces polymer fibers with diameter ranging from nanometers to micrometers from melt or polymer solution when subjected to a large electric field. When an electric potential is applied to polymer solution, the charged polymer solution forms a cone-shaped droplet at the tip of the nozzle[84]. If the electrostatic force is sufficient enough to overcome the surface tension of the solution droplet, the droplet is ejected towards a grounded metal plate. This charged jet undergoes whipping mode, referred to as an instability region where it splits into multiple fine fibers and travels to the collector. The solvent evaporates afterwards and thus the dry ultrafine fibers are formed on the collection plate.

6.3 Methodologies

There are generally three main methodologies used to characterize nanofibers: three-point bend test, nanoindentation, and micro-tensile test. Atomic Force Microscope (AFM) is widely used for probing mechanical properties of soft polymeric nanofibers. However, there are a number of issues that have to be considered. Commercially available material testing machines have been successfully used to conduct tensile testing of specimens with a size of a few millimeters or larger for a few decades. This technique needs to be adapted for characterization of the material properties of nanofibers due to the small force during the test. Further, due to the difficult of nanofiber manipulation, a special holder should be designed to meet this requirement. These three methodologies will be compared and analyzed next, and the design and development of micro-tensile tester will be presented.

6.3.1 Three-point Bend Test

The elastic modulus of a single nanofiber can be obtained by performing a nanoscale three-point bend test on the nanofiber suspended over the etched groove in a silicon wafer using AFM as shown in Figure 6.2. An AFM cantilever tip is utilized to apply a small force leading to deflection at the center of the nanofiber using the force mode. During the process, it is assumed that the nanofiber is an elastic beam with both

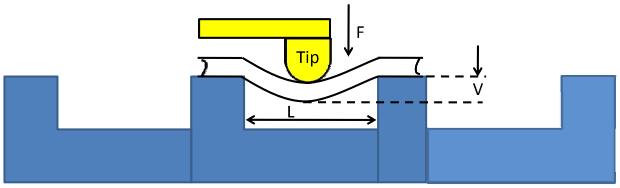

Figure 6.2: Schematic diagram of three-point bend test of a single nanofiber using AFM tip.

ends fixed, and undergoing pure bending (i.e., it means that shear deformation is neglected) as the force is applied. According to beam bending theory for a three-point bending of a beam with two ends fixed, the elastic modulus is expressed by

$$E = \frac{FL^3}{192VI}, \tag{6.1}$$

in which F is the maximum applied force, L is the suspended length, V is the deflection of the beam at the center, and I is the second moment of area of the beam (where $I = \pi d^4/64$ and d is beam diameter).

The advantage of this method is that a small force (low as a few nano-Newtons) can be applied so that thin nanofibers can be investigated and characterized. Meanwhile, there are several concerns about this technique: 1) In order for the elastic beam theory to be valid, the deflection slope of the nanofiber should be less than 5°, which needs to be checked and is not always true. 2) In order not to produce indentation on the surface of the nanofiber, a AFM tip with big radius is used, which could change the load condition (not a point force any more). 3) The ends fixed assumption could not hold if sliding happens between the nanofiber surface and the etched groove.

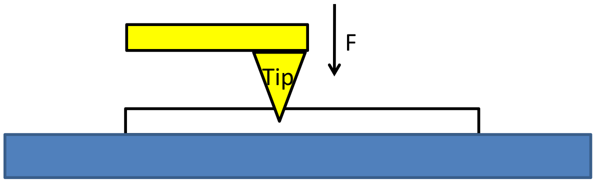

Figure 6.3: Schematic diagram of nanoindentation of a single nanofiber using AFM tip.

6.3.2 Nanoindentation

Nanoindentation might be the most popular method used for characterization of various nanofibers or other flat soft polymers. It has gained increased interest of researchers because of the simplicity of sample preparation as well as implementation of the test. Figure 6.3 shows nanoindentation process using AFM tip insertion into a nanofiber, which is sufficiently adhered on the hard substrate.

Young's modulus is calculated from force spectroscopy data using the Hertz model [37], which defines a relationship between contact radius, nanoindentation load, and nanoindentation depth:

$$E = \frac{3F(1-\mu^2)}{4\sqrt{R_e}\delta^{3/2}}, \tag{6.2}$$

where F is the applied force, μ is the Poisson's ratio of the nanofiber, δ is the indentation depth, and R_e is the equivalent radius ($R_e = \frac{R_a^2 R_f}{R_a+R_f}$, where R_a is the AFM tip radius and R_f is the radius of the fiber). Note that a sphere shape of the AFM tip is assumed for the equation before. In the case of indentation using a rigid conical indenter, a different equation needs to be chosen accordingly.

Although there are numerous advantages of nanoindentation, there are several issues that must be considered: 1) The actual values of tip radius and cantilever spring constant usually deviate from the nominal values that, however, have often been used for the calculation of Young's modulus for convenience, which could lead to some errors. 2) Nanofiber surface roughness will cause a reduced contact pressure for a given load compared to the smooth surface. 3) The curved surface of the fiber has to be taken into account of when using Hertz theory whereas most indentations are performed on the flat surface. 4) Non-perpendicular loading could lead to slip and friction between the AFM tip and the sample surface during indentation [46].

6.3.3 Micro-tensile Test

micro- and nanoscale fibers tensile test requires low load and displacement resolutions not associated with traditional servohydraulic testing systems, which are typically widely used in larger conventional universal testing machines. Figure 6.4 shows the schematic diagram of micro-tensile test of a single nanofiber. The principle of this micro-tensile tester is almost same as larger conventional universal testing machines. During the tensile test, the micro- or nanofiber is driven by a linear actuator and the induced force generated by the elongation of the tensile test is detected by the load cell. The data acquisition system records the corresponding displacement and force for obtaining force-displacement curve, stress-strain curve, etc. The load cell can be replaced with a force sensor using servo electromagnetic actuation combined with a precise capacitive gauge, which is utilized in commercially available system, Agilent T150 UTM (Figure 6.5).

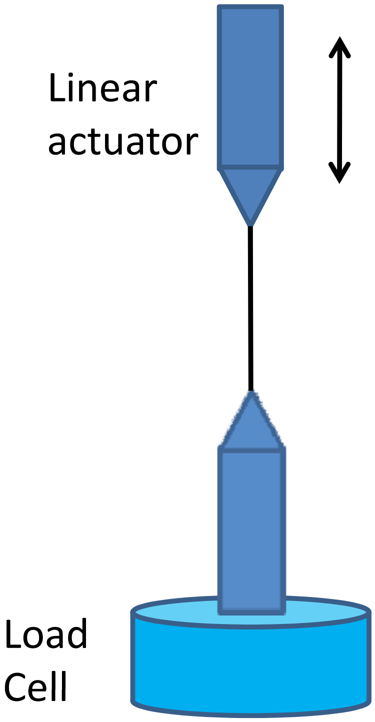

Figure 6.4: Schematic diagram of micro-tensile test of a single nanofiber.

Due to the difficulty in manipulating and gripping single nanofibers, an appropriate holder for gripping fibers is very important for the mciro-tensile testing. Figure 6.5 (a) shows the fiber holder used in Agilent T150 UTM. The end of the microfiber dipped in glue is attached to the tip of a base plate using tweezers. A needle is used to transfer the glue onto the hook-shape tip so as to minimize any disturbance to the sensitive force sensor underneath. By the same way, the other end of the fiber is adhered to the hook-shape tip mounted to the linear actuator using tweezers and the needle. The needle is also utilized to adjust the position of the microfiber such that

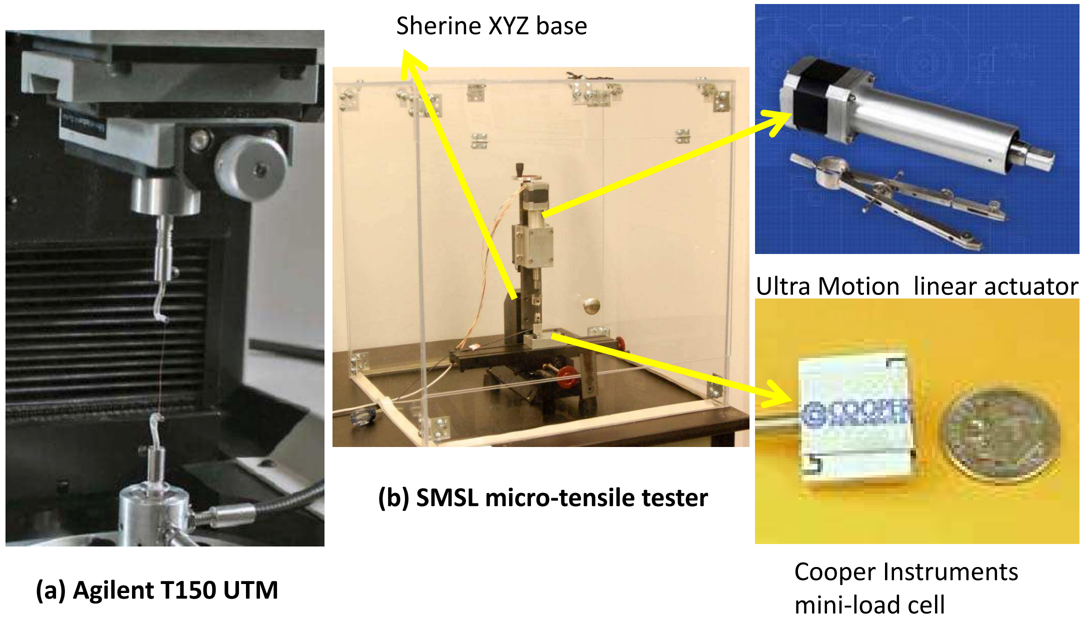

(a) Agilent T150 UTM

(b) SMSL micro-tensile tester

Figure 6.5: Micro-tensile machines. (a) Agilent T150 UTM. (b) Our developed micro-tensile machine.

the fiber is properly aligned in the axial direction of the tensile test. The glue is left to dry for a few hours prior to the test. We developed a similar holder to manipulate nanofibers and found out that it is a doable way, but an inconvenient way to grip nanofibers. The nanofibers sometimes tend to adhere to the tweezers and the whole process is very time consuming.

Due to the drawbacks of the holder of the commercial tensile machine, another kind of novel holder (as shown in Figure 6.6) was designed and developed for nanofibers' manipulation. In general, it includes three steps of preparing a single naofiber for tensile tests: 1) a copper tape with a prepunched hole of some special diameters such as 3/32 inch is used to sandwich and hold the nanofiber along the diameter axis of

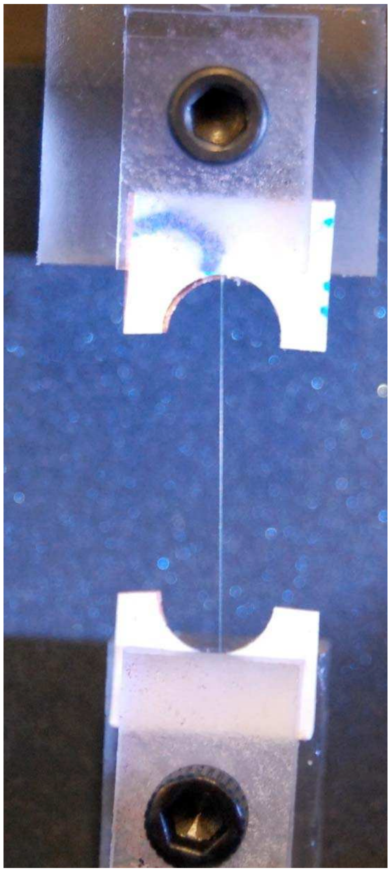

Figure 6.6: Photograph of our developed holder for nanofibers.

the hole. The hole is penetrated by some special punch tool and a thin aluminum sheet is used as a back-up substrate so as not to create wrinkle and warp during the punch process; 2) both ends of the copper tape are clamped by the lead screw driven holder; 3) the center partitions of the copper tape is cut perpendicular to the nanofiber, carefully to not touch the fiber. Figure 6.5 (b) shows that the developed micro-tensile machine incorporating a precision linear actuator (Ultra Motion, Inc.), a mini-load cell (Cooper Instruments and Systems), and a XYZ basis (Sherine, Inc.). After the nanofiber is mounted in the micro-tensile machine, the sample can be stretched to failure at a user defined strain rate and thus the data containing force vs. time information are measured, and further are converted to stress-strain curve.

6.4 Displacement and Force Resolutions

Displacement and force resolutions are two critical specs for a micro-tensile machine because very small force is produced during the fiber elongation. For example, the Micro Bionix 250 system offers load test capability from 1 mN to 250 N and displacement resolution of 1 μm. While Agilent T150 UTM provides force amplitude range of 0.1 μN to 4.5 mN and extension resolution of 35 nm. The displacement of our developed micro-tensile machine is determined by the lead screw pitch of the linear actuator and the step size setting of the stepper motor and it is calculated by

$$r_d = p/200 \cdot s_{step}, \tag{6.3}$$

where p is the lead screw pitch of the linear actuator (0.025 inch) and s_{step} is the step size that sets the amount of rotation per input step. For all 1.8^o step motors, without step size setting it requires 200 input step pulses for one revolution. So if the step size is 1/250, the displacement resolution of the linear actuator is 12.7 nm ($0.025 \times 25.4 \times 10^{-3}/200 \times 1/250$). Since the step size of 1/250 is the smallest micro step size that can be selected, the highest displacement resolution of the developed micro-tensile machine is 12.7 nm.

The force resolution of the system is a complicated problem. It depends on the load cell, table, signal conditioner, amplifier gain, signal filter, and excitation voltage of the load cell. The force peak-peak noise level was investigated with respect to these issues. The testing results show that 1) vibration isolation table (air cushion) does not increase force resolution of the system provided there is no hard hit on the table by users; 2) larger amplifier gain of the signal conditioner tends to improve force resolution; 3) a low pass filter can suppress the high frequency noise in the system and hence lowers the force peak-peak noise level; 4) using a high voltage excitation for the load cell can increase force resolution (Roughly speaking, double the excitation voltage and 1/2 of the force resolution can be achieved). The best force resolution is found to be ∼6 μN (peak-peak) by using the amplifier gain of 1000, 10 Hz low pass filter, and 10 V of the excitation voltage.

6.5 Experimental Results and Discussion

The force time trace, force-displacement curve, and stress-strain curve for a PVDF single microfiber are shown in Figure 6.7. Micro step size of the stepper motor drive is set to be 1/25 and thus the displacement resolution is 127 nm. A 1 kHz PWM wave, generated by data acquisition system Quattro, was fed into the stepper motor drive so as to drive the linear actuator. Material creep phenomenon is clearly observed. Creep is referred to as the property of viscoelastic materials: if the stress is held constant, the strain increases with time. It is also found that the fiber exhibits a significant large strain (more than 200%), which is not commonly seen in the normal elastic materials. The electrospun PVDF fiber is found to exhibit a Young's Modulus of ∼300 MPa, which is about 1/10 of that of commercially available PVDF film.

Regarding the obtained stress-strain curve, there are a couple of issues that need to be considered: 1) the fiber diameter of 10 μm, which was measured by optical microscopy as shown in Figure 6.8, is used for calculation. As we can see, the fiber is not a perfect cylindrical rod and it has different diameter values at different places along the fiber. Further, the measurement error form the optical microscopy could

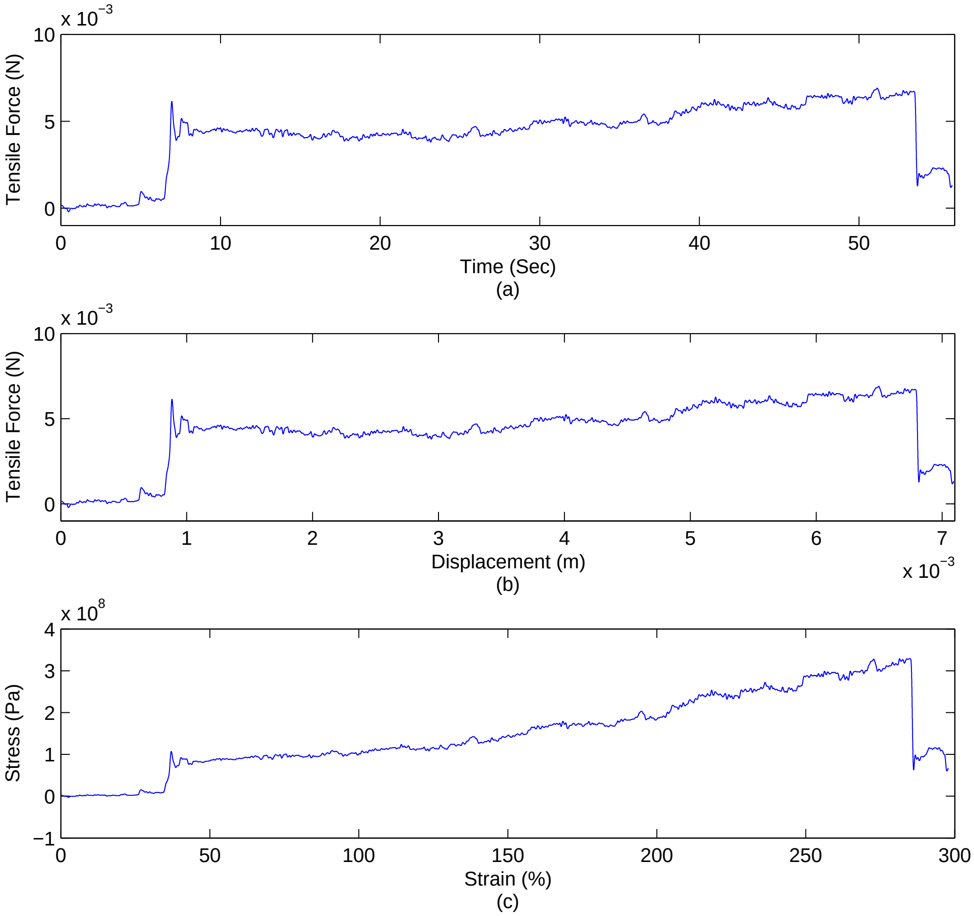

Figure 6.7: (a) Force vs. time curve. (b) Force vs. displacement curve (c) Stress-strain curve.

affect the result; 2) it is assumed that the fiber has a uniform deformation during the elongation process. Figure 6.9 shows some imperfections along fibers. Lumps (Figure 6.9 (a)) along the fiber is often observed. During the elongation in the tensile test, the lump becomes a strong point where the material is difficult to deform so that it leads to other places weaker (easy to deform). Also, constriction along the fiber, as shown in Figure 6.9 (b), is observed and it will reduce the estimated Young's modulus

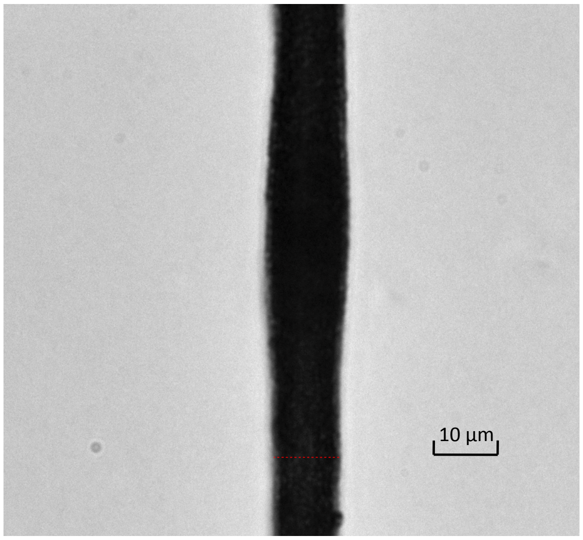

Figure 6.8: Optical microscopy for measuring the diameter of the fiber.

as well. In reality, a real fiber could have both imperfections, which could decrease the estimated Young's modulus more; 3) the tested fiber might be a composite containing residual solvent. Further, it could lead to porosity even if the solvent is fully vaporized.

6.6 Concluding Remarks

In this chapter, three main methodologies (i.e., three-point bend test, nanoindentation, and micro-tensile test) for characterization of nanofibers are compared. The advantages and disadvantages of each method is analyzed and discussed. A micro-tensile machine was developed to characterize micro- or nanofibers by incorporating a precision linear actuator (Ultra Motion, Inc.), a mini-load cell (Cooper Instruments and Systems), and a XYZ basis (Sherine, Inc.). Due to the difficulty in manipulating and gripping single nanofibers, a special holder for gripping fibers was designed and developed, which is found to be more convenient than the holder used in commercial

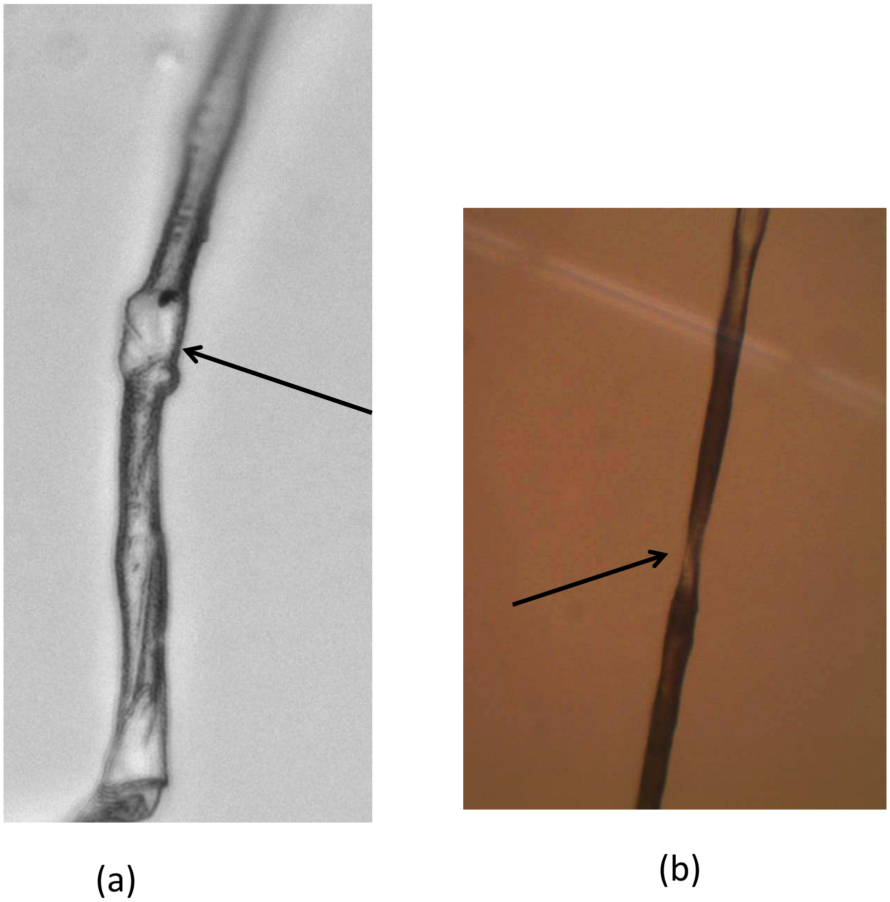

Figure 6.9: Imperfections along fibers (a) lump, (b) constriction.

micro-tensile machines. Displacement and force resolutions of the developed system are further analyzed. The highest displacement of the system can be 12.7 nm and while the best force resolution is found to be ∼6 μN (p-p) by using the amplifier gain of 1000, 10 Hz low pass filter, and 10 V of the excitation voltage. The force time trace, force-displacement curve, and stress-strain curve for a PVDF single microfiber are obtained through the tensile test. Material creep phenomenon is clearly observed. It is also found that the fiber exhibits a significant large strain (more than 200%), which is not commonly seen in the normal elastic materials. The electrospun PVDF fiber is found to exhibit a Young's Modulus of ∼300 MPa, which is about 1/10 of that of commercially available PVDF film. The reasons for the difference are discussed.

CHAPTER 7

CONCLUSION

7.1 Main Contributions to the Field

Acoustic sensor with superior sensitivity, broad frequency bandwidth, and high dynamic range is always of interest. PVDF is a piezoelectric material that has an ability to convert mechanical energy to electric energy, or vice versa. It is a superior material for sensors because the stress constant of PVDF film is typically more than 20 times that of PZT (one piezoceramic material). Even with the high sensitivity of PVDF, many researchers are still dedicated to improving the sensitivity of PVDF film, or more specifically the stress constant of PVDF. In general, most researchers focus on material properties, such as increasing β phase ratio and artificially introducing defects, or processing, such as optimizing stretch ratio and poling temperature, and applying a high electric field. For example, Perlman et al. found that the piezoelectric and pyroelectric constant of PVDF films and copolymers can be increased by nearly 200% when they are simultaneously subjected to stretching and poling process [60]. Non-porous PVDF films with very high ratios of β phase were obtained via a very high pressure applied to porous PVDF films [43]. A compliant dielectric annulus insulates the polarized region from the edges of the film so that it eliminates the breakdown at the edges of the film, and thus allowing increased poling voltage and reducing the poling time [76]. This research is focused on improving the stress constant by means of design.

The static sensitivity of PVDF film is defined as the ratio of the output voltage over the pressure acting on the PVDF material (i.e., $K = V_o/P$). For a given external pressure, the only feasible way to improve the sensitivity of PVDF film is to increase the voltage output of the film. The voltage produced by a capacitive sensor is given by the ratio between charge and capacitance (i.e., $V_o = Q/C$, where Q is the induced charge and C is the capacitance). Thus there are two methods to improve the voltage output of the PVDF film: increase the charge generated by the PVDF film and/or reduce the capacitance of the device. Our developed sensor achieves both methods of improving output voltage, hence significantly improve the sensitivity of the sensor.

The acoustic sensor, present in this dissertation, exploits the key advantages of PVDF as a sensor material by means of two key design elements aimed at increasing the charge and decreasing the effective device capacitance. The first design element is a stress amplification mechanism through the area ratio between the overall surface exposed to acoustic waves and the area of the micro-pillars array (Figure 3.1). Because PVDF responds to stress, this mechanism increases the amount of charge for a given pressure level. The second design element is top and bottom electrodes selectively patterned to form an overlapping active area determined by the micro-pillars. Excluding the capacitance of the other inactive area, the design with patterned electrodes reduces the capacitance of the sensor and hence increases the voltage generated by the sensor.

The small size, high stiffness, and reduced mass of MEMS sensors are of great interest because such devices can significantly improve both the temporal and spatial measurement bandwidth. The sensor realization requires micro-fabrication process and this technology is available from Dr. Hansford's group at the Biomedical Engineering Center of OSU. Previously patterned PDMS stamps molded from photolithographically fabricated masters are used in the production of individual and interconnected PVDF micropillar arrays as shown in Figure 1.4. Please note that such sensor works under 3-3 mode (or, referred to as thickness mode). Taking advantage of this thickness mode, the developed PVDF micro-pillar sensor has the frequency bandwidth of at least 20 Hz- 100 kHz (could be up to a few mega Hz depending on the real configurations, i.e., ultrasonic range).

A PVDF micro-pillar sensor with patterned electrodes and gap ratio of 5.8182 was developed and various acoustic tests were performed on this sensor. The sensitivity calibration test shows that the developed sensor has a sensitivity of 189.3 μV/Pa, which is 60.39× greater than that of the commercial solid PVDF with the same footprint area and the thickness. Or more specifically, the measured stress constant of the sensor is -19.93 V/m/Pa, which is 60.39× bigger than that of commercial solid PVDF (g_{33} =-0.33 V/m/Pa). Meanwhile the measured stress constant amplification ratio (60.39) is in good agreement with the predicted amplification ratio (59.19), thus confirming the performance advantages of the micro-pillar sensor.

7.2 Summary of Results and Findings

The goal of this research is to develop an acoustic sensor with superior sensitivity, broad frequency bandwidth, and small footprint. It produces numerous important results and findings as follows:

- A PVDF rod is modeled as a second-order mechanical system and a first-order electrical system. The model is used to determine the system frequency bandwidth. This lumped model can be extended to various PVDF based sensors.

- A discrete damped rod model with electromechanical coupling based on piezoelectric constitutive equations and Hamilton's principle is created. The simulation results of discrete damped rod model with electromechanical coupling show that the piezoelectric electromechanical coupling increases the overall stiffness of the system if the electrodes are left open and therefore the natural frequencies are smaller if the electromechanical coupling is neglected, which is consistent with the existing literature. The simulation trends demonstrate our models are convergent with the increasing number of elements. There is approximately 15% error between the models with and without electromechanical coupling. Around the natural frequency, the linear piezoelectric constitutive model does not work because it does not include the resonance. The resonance phenomena are observed if we use the dynamic governing equations whether we include the electromechanical coupling or not.

- A cylindrical curvature microphone is designed and developed to study the sensitivity, frequency bandwidth and other behaviors of the PVDF film based microphone. The acoustic testing results on the curved microphone show that the sensitivity of the microphone is slightly higher than that of the sound level meter in low and high frequency ranges. Further, the involvement of a tube enclosure does not significantly increase the sensitivity. A small resistance value (high cutoff frequency) suppresses the electrical 60 Hz noise (which is always observed and typically significant compared to the signals) but also attenuates the sensor signal.

- An acoustic sensor design consisting of micron-sized Polyvinylidene Fluoride (PVDF) pillars and patterned electrodes is proposed. The sensitivity of the proposed microphone is analyzed and compared against the sensitivity of two sensors: (i) flat continuous PVDF film and (ii) micro-pillars with full flat electrodes. The proposed sensor has the potential to achieve 100× the sensitivity of commercial PVDF film.

- A constrained optimization algorithm has been developed as a function of geometric parameters and electrical parameters of the sensor and conditioning amplifier.

- A micro-fabrication process of the acoustic sensor based on PVDF micro-pillars and patterned electrodes is described. In order to determine the piezoelectric properties, a PVDF sample consisting of a uniform pattern of 5 μm pillars was manufactured and tested on a Hysitron TriboIndenter nanomechanical test instrument. The nanoindentation testing results show that the PVDF micropillar sample exhibits obvious piezoelectric responses under an applied voltage or strain.

- A macro simple process is described to create a proof-of-concept microphone based on stress amplification through an area ratio and patterned electrodes. An crosshair aluminum pattern was micromachined by the CNC-miller and used for the sensor assembly.

- Finite element simulations including static structure analysis, modal analysis and harmonic response are performed in ANSYS WORKBENCH to finalize and evaluate the microphone assembly with the design requirements of a frequency range of 100 kHz and a dynamic range of 180 dB. Peak coalescence caused by the first three adjacent natural frequencies and the structure damping ratio was observed and analyzed. The static and dynamic stress distributions make sure of the design within the safety constraint.

- Experimental setup is developed to characterize the microphone using a commercial available PCB microphone as reference. The theory and design of a circular plane wave tube is presented and signal conditioning circuits including the preamplifier circuit and the notch filter are also developed. The buffer circuit converts the high output impedance of the microphone into a low impedance signal which eliminates the loading effect and thus minimizes the signal loss. Approximately 55 dB reduction at 60 Hz is obtained for the designed notch filter.

- Acoustic tests show that the crosshair microphone exhibits a good linearity up to 140 dB (SPL) and a relatively flat frequency response up to 10 kHz. The microphone has a sensitivity of 27.8 mV/Pa. Most importantly, the sensitivity of the sensor itself (without the amplifier) is found to be 27.8 μV/Pa that is

3.01 times the sensitivity of the commercial available PVDF film working in 3-3 mode, which is approximate to the area amplification ratio of 3.2.

- Microfabrication of the acoustic sensor based on micro-pillars array and patterned electrodes is briefly described. The theoretical sensitivity of the developed sensor with gap ratio of 5.8182 is analyzed.
- Acoustic tests show that the microphone exhibits a good linearity up to 120 dB (SPL) and a relatively flat frequency response up to 15 kHz (This is the frequency bandwidth of the PCB microphone and our sensor frequency range should be greater than 100 kHz considering the sensor works in the thickness mode). The sensitivity calibration test shows that the developed micro-pillar sensor has a sensitivity of 189.3 μV/Pa, which is 60.39× greater than that of the commercial solid PVDF with the same footprint area and the thickness. Or more specifically, the measured stress constant of the sensor is -19.93 V/m/Pa, which is 60.39× larger than that of commercial solid PVDF (g_{33} =-0.33 V/m/Pa). Meanwhile, the measured stress constant amplification ratio is in good agreement with the predicted amplification ratio.
- Three main methodologies (i.e., three-point bend test, nanoindentation, and micro-tensile test) for characterization of nanofibers are compared. The advantages and disadvantages of each method is analyzed and discussed. A micro-tensile machine was developed to characterize micro- or nanofibers by incorporating a precision linear actuator (Ultra Motion, Inc.), a mini-load cell (Cooper

Instruments and Systems), and a XYZ basis (Sherine, Inc.). Due to the difficulty in manipulating and gripping single nanofibers, a special holder for gripping fibers was designed and developed, which is found to be more convenient than the holder used in commercial micro-tensile machines. Displacement and force resolutions of the developed system are further analyzed. The highest displacement of the system can be 12.7 nm and while the best force resolution is found to be ∼6 μN (p-p) by using the amplifier gain of 1000, 10 Hz low pass filter, and 10 V of the excitation voltage.

- The force time trace, force-displacement curve, and stress-strain curve for a PVDF single microfiber are obtained through the tensile test. Material creep phenomenon was clearly observed. It is also found that the fiber exhibits a significant large strain (more than 200%), which is not commonly seen in the normal elastic materials. The electrospun PVDF fiber is found to exhibit a Young's Modulus of ∼300 MPa, which is about 1/10 of that of commercially available PVDF film. The reasons for the difference were discussed.

7.3 Future Work

While this research has accomplished several key goals and validated an ultrasonic acoustic sensor based on micro-pillars and patterned electrodes with extreme sensitivity, there are still some opportunities for future study. The following list enumerates possibilities for future work:

- For comparison reasons, more micro-pillar sensors with different gap ratios or pillar heights could be fabricated and investigated. Acoustic tests could lead to more interesting results and findings. Questions such as, what is the limitation of the fabrication gap ratio, could be determined.

- Poling process could be further investigated. How does the poling process affect the piezoelectric properties of the developed sensor? What is the optimum elevated temperature? Studies on them could result in more useful outcomes.
- The reliability of micro-pillar sensors' microfabrication process could be further studied. Based on the same principle, the package issues could be studied in the future.
- Regarding the microfiber characterization, more tensile tests could be performed to observe the variation of the different testing results. Although initial dynamic test showed that there was no force produced when the fiber was subjected to a sine wave voltage, it is still possible to detect forces if the voltage is applied to a PVDF fiber mat.

BIBLIOGRAPHY

[1] F. Ahmadkhanlou, G. Washington, Y. Wang, and S. Bechtel. “the development of variably compliant haptic systems using magnetorheological fluids”. In *Proceedings of SPIE Smart Structures and Materials Conf.*, volume 5757, pages 491–502, 2005.

[2] S. Aoyagi, K. Furukawa, D. Ono, K. Ymashita, T. Tanaka, K. Inoue, and M. Okuyama. “development of a capacitive ultrasonic sensor having parylene diaphragm and characterization of receiving performance of arrayed device”. *Sens. Actuators A*, 145:94–102, 2008.

[3] D.P. Arnold, S. Gururaj, S. Bhardwaj, T. Nishida, and M. Sheplak. “A piezoresitive microphone for aeroacoustic measurements”. In *2001 ASME International Mechanical Engineering Congress and Exposition*, Proc. IMECE ’01, 2001.

[4] A. Bhatti, H.S. Al-Raweshidy, and G. Murtaza. “optical antenna using d-fibre for radio-over-fibre applications”. *Opt. Fiber Technol.*, 8:153–161, 2002.

[5] Robert D. Blevins. *Formulas for Natural Frequency and Mode Shape*. Van Nostrand Reinhold Co, New York, NY, 1979.

[6] G.R. Bogart, D.W. Carr, and J.A. Rogers. “Fabrications of PVDF gratings: Final report for LDRD project 79884”. Technical Report SAND2005-6706, Sandia National Laboratories, 2006.

[7] W.J. Buehler, J.V. Gilfrich, and R.C. Wiley. “effect of low-temperature phase changes on the mechanical properties of alloys near composition tini”. *J. Appl. Phys.*, 34:1475, 1963.

[8] R.E. Cais and J.M. Kometani. “new isomers of poly(vinyl fluoride) with controlled regiosequence microstructure”. *Polym.*, 29:168, 1988.

[9] S. Charleston-Villalobos, S. Cortes-Rubiano, R. Gonzalez-Camarena, G. Chi-Lem, and T. Aljama-Corrales. “Respiratory acoustic thoracic imaging (RATHI): assessing deterministic interpolation techniques”. *Med. Biol. Eng. Comput.*, 42:618–626, 2004.

[10] A.E. Clark, J.B. Restorff, M. Wun-Fogle, T.A. Lograsso, and D.L. Schlagel. “magnetostrictive properties of body-centered cubic fe-ga and fe-ga-al alloys”. *IEEE Trans. Magn.* , 36(5):3238, 2000.

[11] T.F. Coleman and Y. Li. “An interior, trust region approach for nonlinear minimization subject to bounds”. *SIAM J. Optim.*, 6:418–445, 1996.

[12] M. J. Dapino. “Magnetostrictive materials: Their use in smart structure applications”. In J. A. Harvey, editor, *Encyclopedia of Smart Materials.* John Wiley and Sons, 2002.

[13] M.J. Dapino, F.T. Calkins, and A.B. Flatau. “measured terfenol-d material properties under varied applied magnetic field levels”. In *Proceedings of SPIE Smart Structures and Materials Conf.*, volume 2717(66), 1996a.

[14] T.R. Dargaville, M.C. Celina, J.M. Elliott, P.M. Chaplya, G.D. Jones, D.M. Mowery, R.A. Assink, R.L. Clough, and J.W. Martin. “Characterization, performance and optimization of PVDF as a piezoelectric film for advanced space mirror concepts”. Technical Report SAND2005-6846, Sandia National Laboratories, 2005.

[15] B. Dickens, E. Balizer, A.S. DeReggi, and S.C. Roth. “hysteresis measurements of remanent polarization and coercive field in polymers”. *J. Appl. Phys.*, 72:4258, 1992.

[16] A. Dubach, R. Raghavan, J.F. Löffler, J. J. Michler, and U. Ramamurty. “Micropillar compression studies on a bulk metallic glass in different structural states”. *Scr. Mater.*, 60:567–570, 2009.

[17] T. Duerig, D. Stoeckel, and D. Johnson. “sma:smart materials for medical applications”. In *Proceedings of SPIE European Workshop on Smart Structures in Engineering and Technology*, volume 4763, pages 7–15, 2003.

[18] L. Faidley. *Characterization and modeling of ferromagnetic shape memory alloy Ni-Mn-Ga in a collinear stress-field configuration.* PhD thesis, The Ohio State University, Columbus, OH, 2006.

[19] N. Ferrell, J. Woodard, and D. Hansford. “Fabrication of micro- and nanoscale polymer structures by soft lithography and spin dewetting”. *Biomed. Microdevices*, 28:966–971, 2007.

[20] H. Fong. “electrospun nylon 6 nanofiber reinforced BIS-GMA/TEGDMA dental restorative composite resins”. *Polymer*, 45:2427–2432, 2004.

[21] M.L.R. Fripp and N.W. Hagood. “distributed structural actuation with electrostrictors”. *J. Sound Vib.*, 203(1):11–40, 1997.

[22] N. Fujitsuka, J. Sakata, Y. Miyachi, K. Mizuno, K. Ohtsuka, Y. Taga, and O. Tabata. “Monolithic pyroelectric infrared image sensor using PVDF thin film”. *Sens. Actuators A*, 66:237–243, 1998.

[23] D. Gallego, N. Ferrell, N. Higuita, and D.J. Hansford. “Versatile methods for the fabrication of polyvinylidene fluoride microstructures”. *Macro. Rapid. Commun.*, submitted, 2009.

[24] F.X. Gil, J.M. Manero, and J.A. Planell. “relevant aspects in the clinical applications of niti shape memory alloys”. *J. Mater. Sci.*, 7(7):403–406, 1996.

[25] P.E. Gill, M. Murray, and M.H. Wright. *Practical Optimization.* Academic Press, London, 1981.

[26] S. Goodrich, M. Tawk, and W. Orr. The use of polyvinylindene fluoride (pvdf) film airflow sensors: An alternative to the nasal cannula for measuring respiratory events. Website, 2003. http://www.dymedix.com/pdf/apss2003orr.pdf.

[27] R. Gopal, S. Kaur, Z. Ma, C. Chan, S. Ramakrishna, and T. Matsuura. “electrospun nanofibrous filtration membrane”. *J. Membr. Sci.*, 281:581–586, 2006.

[28] K. Grosh, J. Zheng, E. deBoer, and A. L. Nuttall. “High frequency electromotility of the cochlea”. *J. Acoust. Soc. Am.*, 115:2178–2184, 2004.

[29] D.L. Hall and A.B. Flatau. “broadband performance of a magnetostrictive shaker”. *J. Intell. Mater. Syst. Struct.*, 6(1):109–116, 1995.

[30] R. Heydt, R. Kornbluh, R. Pelrine, and V. Mason. “design and performance of an electrostrictive-polymer-film acoustic actuator”. *J. Sound Vib.*, 215(2):297–311, 1998.

[31] C.L. Hom. “simulating electrostrictive deformable mirrors: Ii. nonlinear dynamic analysis”. *Smart Mater. Struct.*, 8(5):700–708, 1999.

[32] S.B. Horowitz, T. Nishida, T. Nishida, and M. Sheplak. “Design and characterization of a micromachined piezoelectric microphone”. In *26th AIAA Aeroacoustics Conference*, Proc. AIAA, 2005.

[33] J.S. Hundal and R. Nath. “piezoelectricity and polarization studies in unstretched san copolymer films”. *J. Mater. Sci.*, 34:5397, 1999.

[34] T. Ikeda. *Fundamentals of Piezoelectricity.* Oxford Science Publications, New York, NY, 1996.

[35] D.J. Inman. *Engineering Vibration.* Prentice-Hall, NJ, 2001.

[36] T.K. Jee. Nanoscale characterization of soulution-cast poly(vinylidene fluoride) thinkfilms using atomic force microscopy. Master's thesis, Texas A&M University, college State, TX, 2005.

[37] K.L. Johnson. *Contact Mechanics*. Cambridge University Press, West Nyack, NY, 1992.

[38] M.R. Jolly. "properties and applications of commercial magnetorheological fluids". *J. Intell. Mater. Syst. Struct.*, 10(1):5, 1999.

[39] H. Kawai. "The piezoelectricity of poly (vinylidene fluoride)". *JPN. J. Appl. Phys.*, 8:975–976, 1979.

[40] R.A. Kellogg. The Delta-E effect in Terfenol-D and its application in a tunable mechanical resonator. Master's thesis, Iowa State University, Ames, IA, 2000.

[41] R.A. Kellogg. *Development and modeling of iron gallium alloys*. PhD thesis, Iowa State University, Ames, IA, 2003.

[42] M. Koucky. Piezoelectric polymer microstructures for biomedical applications. Master's thesis, The Ohio State University, Columbus, OH, 2009.

[43] S. Lanceros-mendez, V. Silva, and R.G. Filho. Patent: Non-porous polyvinylidene fluoride (pvdf) films in the beta phase and processing method thereof, August 2008.

[44] L.J. Lee, M.J. Madou, K.W. Koelling, S. Daunert, S. Lai, and C.G. Koh. "Design and fabrication of CD-like microfluidic platforms for diagnostics: microfluidic functions". *Biomed. Microdevices*, 3:245–254, 2001.

[45] G. Li, N. Kagami, and H. Ohigashi. "the possibility of formation of large ferroelectric domains in a copolymer of vinylidene fluoride and trifluoroethylene". *J. Appl. Phys.*, 72:1056, 1992.

[46] X. Li, H. Gao, C.J. Murphy, and K.K. Caswell. "nanoindentation of silver nanowires". *Nano Lett.*, 3:1495–1498, 2003.

[47] J. Manzo, E. Garcia, A. Wickenheiser, and G. Horner. "design of a shape-memory alloy actuated macro-scale morphing aircraft mechanism". In *Proceedings of SPIE Smart Structures and Materials Conf.*, volume 5764, pages 232–240, 2005.

[48] D. Marinković, H. Koppe, and U. Gabbert. "Accurate modeling of the electric field within piezoelectric layers for active composite structures". *J. Intel. Mat. Syst. Str.*, 18:503–513, 2007.

[49] Measurement Specialties, Inc. *"Piezo Film Sensors Technical Manual"*.

[50] Measurement Specialties, Inc. *"Piezo Film Sensors Technical Manual"*, 1999.

[51] R. Miles, Q. Su, W. Cui, M. Shetye, F.L. Degertekin, B. Bicen, C. Garcia, S. Jones, and N. Hall. "A low-noise differential microphone inspired by the ears of the parasitoid fly ormia ochracea". *J. Acoust. Soc. Am.*, 125:2013–2026, 2009.

[52] A.P. Mortensen and M.J. Dapino. "broadband acoustic transducer driven by magnetostrictive composite rod and electrostrictive stack". *J. Sound Vib.*, 307:3–5, 2007.

[53] W.J. Morton. Patent: Method of dispersing fluids, 1902.

[54] M. Munjal. *Acoustics of Ducts and Mufflers.* John Wiley, New York, NY, 1987.

[55] R.L.H. Murphy. Patent: Method and apparatus for displaying body sounds and performing diagnosis based on body sound analysis, September 2004.

[56] V.A. Neelakantan, G. Washington, and N.K. Bucknor. "two-stage actuation system using dc motors and piezoelctric actuators for controllable industrial and automotive brakes and clutches". In *Proceedings of SPIE Smart Structures and Materials Conf.*, volume 5762, pages 275–286, 2005.

[57] D.T. Nosse and M.J. Dapino. "compact actuation through magnetorheological flow control and rectification of magnetostrictive vibrations". In *Proceedings of SPIE Smart Structures and Materials Conf.*, volume 5764, pages 262–273, 2005.

[58] H. Ohigashi. "electromechanical properties of polarized poly(vinylidene fluoride) films as studied by the piezoelectric resonance method". *J. Appl. Phys.*, 47:949, 1976.

[59] F. Pablo and B. Petitjean. "characterization of 0.9pmn-0.1pt patches for active vibration control of plate host structures". *J. Intell. Mater. Syst. Struct.*, 11:857–867, 2000.

[60] M.M. Perlman and M. Canada. Patent: Method to double the piezo-and pyro-electric constant of polyvinylidene fluoride (pvdf) film, October 1993.

[61] V. Piefort. *Finite element modelling of piezoelectric active structures.* PhD thesis, Université Libre de Bruxelles, Brussels, Belgium, 2001.

[62] S. Ramakrishna, K. Fujihara, W. Teo, T. Yong, Z. Ma, and R. Ramaseshan. "electrospun nanofibers: solving global issues". *Mater. Today*, 9:40–50, 2006.

[63] M.M.D. Ramos, H.M.G. Correia, and S. Lanceros-Mendez. "Atomistic modelling of processes involved in poling of PVDF". *Comp. Mater. Sci.*, 33:230–236, 2005.

[64] N.N. Sarawate. *Characterization and modeling of the ferromagnetic shape memory alloy Ni-Mn-Ga For Sensing and actuation.* PhD thesis, The Ohio State University, Columbus, OH, 2008.

[65] H. Schreuder-Gibson, P. Gibson, K. Senecal, M. Sennett, J. Walker, W. Yeomans, D. Ziegler, and P.P. Tsai. "protective textile materials based on electrospun nanofibers". *J. Adv. Mater.*, 3:44–55, 2002.

[66] A. Selamet. ME766 course notes, 200.

[67] A. Selamet and P. Radavich. "The effect of length on the acoustic attenuation performance of concentric expansion chambers: an analytical, computational and experimental investigation". *J. Sound Vib.*, 201:407–426, 1997.

[68] E. P. S. Tan and C. T. Lim. *Mechanical Characterization of a Single Nanfiber.* Springer Netherlands, 2006.

[69] M.L. Thompson. *On the material properties and constitutive equations of piezoelectric poly vinylidene fluoride (PVDF).* PhD thesis, Drexel University, Philadelphia, PA, 2002.

[70] M. Toda. "Phase-matched air ultrasonic transducers using corrugated PVDF film with half wavelength depth". *IEEE T. Ultrason. Ferr.*, 48:1568–1574, 2001.

[71] M. Toda. Patent: Acoustic sensor using curved piezoelectric film, August 2005.

[72] M. Toda and M.L. Thompson. "Contact-type vibration sensor using curved clamped PVDF film". *IEEE Sens. J.*, 6:1170–1177, 2006.

[73] H.S. Tzou and W.K. Chai. "Design and testing of a hybrid polymeric electrostrictive/piezoelectric beam with bang-bang control". *Mech. Syst. Signal. Pr.*, 21:417–429, 2007.

[74] K. Ullakko. "magnetically controlled shape memory alloys: A new class of actuator materials". *J. Mater. Eng. Perform.*, 5(3):405–409, 1996.

[75] M.R. VanLandingham. "Review of instrumented indentation". *J. Res. NIST.*, 108:249–265, 2003.

[76] H. von Seggern and T.T. Wang. Patent: Polarizing of piezoelectric material, April 1985.

[77] F. Wang, M. Tanaka, and S. Chonan. "Development of a PVDF piezopolymer sensor for unconstrained in-sleep cardiorespiratory monitoring". *J. Intell. Mater. Syst. Struct.*, 14:185–190, 2003.

[78] X. Wang, C. Drew, S.H. Lee, K.J. Senecal, J. Kumar, and L.A. Samuelson. "electrospun nanofibrous membranes for highly sensitive optical sensors". *Nano Lett.*, 2:1273–1275, 2002.

[79] Y. Wang, K. Ren, and Q. M. Zhang. "Direct piezoelectric response of piezopolymer polyvinylidene fluoride under high mechanical strain and stress". *Appl. Phys. Lett.*, 91:22905–22905–3, 2007.

[80] Y.C. Wang, C.H. Huang, Y.C. Lee, and H.H. Tsai. "Development of a PVDF sensor array for measurement of the impulsive pressure generated by cavitation bubble collapse". *Exp. Fluids*, 41:365–373, 2006.

[81] M. Wegener, W. Kunstler, and R. Gerhard-Multhaupt. "ferroelectric polarization in stretched piezoand pyroelectric poly(vinylidene fluoride-hexafluoropropylene) copolymer films". *J. Appl. Phys.*, 92:7442, 2002.

[82] R. D. White and K. Grosh. "Microengineered hydrodynamical cochlear model". *Proc. Natl. Acad. Sci.*, 102:1296–1301, 2005.

[83] J. Xu, M.J. Dapino, D. Gallego-Perez, and D. Hansford. "Microphone based on polyvinylidene fluoride (PVDF) micro-pillars and patterned electrodes". *Sens. Actuators A*, 153:24–32, 2009.

[84] H. Yang. *Fabrication and characterization of multifunctional nanofiber nanocomposite structures through co-electrospinning process.* PhD thesis, Drexel University, Philadelphia, PA, 2007.

[85] H. Yoshimoto, Y.M. Shin, H. Terai, and J.P. Vacanti. "a biodegradable nanofiber scaffold by electrospinning and its potential for bone tissue engineering". *Biomaterials*, 24:2077–2082, 2003.

[86] C. Wang Z. Wang and L. Liu. "Design and analysis of a PZT-based micromachined acoustic sensor with increased sensitivity". *IEEE T. Ultrason. Ferr.*, 52:1840–1850, 2005.